Durham E-Theses

Galaxy clustering and galaxy clusters from the UKIDSS DXS

KIM, JAE,WOO

How to cite:

Use policy

Galaxy clustering and galaxy clusters from the UKIDSS DXS

Jae-Woo Kim

A Thesis presented for the degree of
Doctor of Philosophy

Durham
University

Extragalactic Astronomy
Department of Physics
University of Durham
England

September 2011

Dedicated to

My Family

for their love and support

Galaxy clustering and galaxy clusters from the UKIDSS DXS

Jae-Woo Kim

Submitted for the degree of Doctor of Philosophy

September 2011

Abstract

Recent wide and deep surveys allow us to investigate the large scale structure of the Universe at high redshift. We present studies of the clustering of high redshift galaxies and galaxy clusters, using reprocessed UKIDSS DXS catalogues. The UKIDSS DXS is one of the deepest near-IR surveys to date and provides sufficient samples of the distant Universe.

Firstly we measure the angular correlation function of high redshift red galaxies which are Extremely Red Objects (EROs) and Distant Red Galaxies (DRGs) in Chapters 3 and 4 from DXS SA22 and Elais-N1 fields. We found that their angular correlation functions can be described by a broken power-law. Thus we estimated clustering properties on small and large scales separately. Then we found that red or bright samples are more strongly clustered than those having the opposite characteristics. In addition old, passive EROs are found to be more clustered than dusty, star-forming EROs. The effect of cosmic variance on angular clustering was also investigated.

Chapter 5 describes the halo modelling for the angular clustering of EROs. EROs reside in in dark matter haloes having $> 10^{12.9} h^{-1} M_\odot$, and have a bias of 1.93 at $z = 1.12$ and 3.17 at $z = 1.55$. From a direct comparison between the observed clustering and the cosmological model, they show good agreement. However the cosmological simulation may predict too many red satellites, especially at high redshfit.

In Chapter 6, we present the details of our cluster detection algorithm based on the red sequence technique. This algorithm successfully found published galaxy clusters in the DXS Elais-N1 field. We also found many overdensities in the DXS SA22 field. Two prominent galaxy clusters were confirmed by spectroscopic observations, and we identified a supercluster candidate. Finally the clustering strength

of candidate galaxy clusters showed good agreement with previous results and was consistent with the ΛCDM prediction.

In the near future the full DXS catalogue will provide an opportunity to detect various high redshift populations. With other advanced surveys, it will be possible to investigate more details of the large scale structure of the Universe.

Declaration

The work in this thesis is based on research carried out at the Extragalactic Astronomy Group, Department of Physics, Durham University , UK. No part of this thesis has been submitted elsewhere for any other degree or qualification and it all my own work unless referenced to the contrary in the text. Parts of this thesis have been published or are to be published in the following papers:

Kim J.-W., Edge A. C., Wake D. A., Stott J. P., 2011, MNRAS, 410, 241

Kim J.-W., Edge A. C., Wake D. A., Gonzalez-Perez V., Yamada T., Sato Y., Pan-STARRS PS1, 2011, to be submitted to MNRAS

Kim J.-W., Edge A. C., Stott J. P., Wake D. A., 2011, to be submitted to MNRAS

Acknowledgements

Contents

List of Figures

List of Tables

Chapter 1

Introduction

1.1 Modern Cosmology

Through the history of mankind, we can find various kinds of calendar based on the observation of the Sun or Moon with the naked eye. Simultaneously celestial objects such as stars, planets and comets were very important agriculturally, politically or religiously in the past. However in the 17th century, with the invention of the telescope, it was recognised that the Earth is not the centre of Universe. From the 18th to the early of 20th centuries it was known that the Sun is not located at the centre of the Universe, but displaced from the Galactic centre. In the 1920s Edwin Hubble found that the distances to nebulae, which were regarded as the part of the Milky Way at that time, are too far to think those are members of our galaxy. Also Hubble's law ($v = Hd$, where v is the receding velocity, H is the Hubble constant and d is the distance, Hubble 1929) indicated that the Universe is expanding.

Theoretically Albert Einstein suggested special and general relativity theories in the early 20th century. In particular Einstein's general relativity field equation led to the Friedman-Lemaitre-Robertson-Walker (FLRW) metric, which indicated the possibility of expansion or contraction of the Universe. In 1927 Georges Lemaitre suggested the origin of the Universe through an expansion from a singularity that was later christened as the "Big Bang". The discovery by Hubble was considered one of the strongest pieces of evidence for the Big Bang theory. Because the correlation between velocity and distance means that galaxies recede from each other, all matter

was concentrated in a small region in the past.

There are two more clear lines of evidence supporting the Big Bang theory. One of them is the abundance of helium. From the Big Bang theory, the early Universe was hot enough to cause nucleosynthesis, and after a short period the Universe cooled and ceased nuclear fusion. Thus the predicted abundance of helium is 25 per cent of the total baryonic matter, and now confirmed observationally. Another piece of evidence, the most important one, is the discovery of the Cosmic Microwave Background (CMB) radiation in the middle of 20th century by Arno Penzias and Robert Wilson. The CMB has a thermal black body spectrum with the temperature of 2.7K, and is observed uniformly in all directions. From the Big Bang theory, electrons combined with protons at $z \sim 1,100$, the recombination era, when matter and radiation were decoupled. The radiation from this epoch is observed as the 2.7K black body, through being redshifted and cooled by the expanding Universe. Considering all current observations, the Big Bang theory is the most reliable explanation to describe the origin of the Universe.

1.1.1   Dark components

The recent standard cosmological paradigm is the Lambda cold dark matter (ΛCDM) model which contains two non-baryonic, dark components, 'dark energy' and 'cold dark matter'. It means that there are more ingredients other than ordinary matter required to describe the Universe. It is not currently possible to detect these dark components directly, so we do not know what they are exactly. However it is possible to constrain their properties by observing their influence on stars and galaxies.

The existence of dark matter was deduced by Fritz Zwicky in 1933. He estimated the mass of the Coma cluster through the motion of member galaxies. Puzzlingly the mass measured by galaxy motions was larger than that predicted by the brightnesses of cluster member galaxies. It indicates that there is a non-visible component of the cluster contributing to the total mass. In the 1960's measurements of the velocity rotation curves of spiral galaxies lead to a surprising result. Stars at large radii in spiral galaxies have similar rotational velocities as those in the inner regions, i.e., the velocity curve is flat out to large radii. Since the observable mass density

in stars is low at large radii, it means that non-visible matter also exists in spiral galaxies. Lastly, massive objects such as galaxy clusters change the path of light from distant objects, if they are aligned, through gravitational lensing. This process is useful to measure the mass of a massive object causing lensing without requiring any dynamical information of the object. It is known that the masses of galaxy clusters derived from the lensing method are consistent with the dynamical masses, suggesting the existence of the dark matter. In order to explain the structure of the Universe, the dark matter travelling at non-relativistic speeds, i.e., it is "cold", is preferred since it is believed that small fluctuations on the CMB grow large structures hierarchically. It is also required that the dark matter does not interact with baryonic matter via electromagnetic forces.

Another important dark component is dark energy (Λ). Dark energy has a negative pressure accelerating the expansion of the Universe. It is still impossible to explain dark energy because of the lack of accurate data measuring the expansion rate of the Universe. However we can establish the existence of dark energy. The evidence for the dark energy was first deduced from observations of supernova which can be used to calculate distances. Perlmutter et al. (1998) reported their observational results for Type Ia supernovae, and suggested a change of expansion rate. In addition Riess et al. (1998) also suggested $\Omega_\Lambda > 0$ meaning the accelerated expansion by using 10 Type Ia supernovae. The CMB measurements from the Wilkinson Microwave Anisotropy Probe (WMAP) show that the fractions of ordinary matter and dark matter are 4.6 and 22.7 per cent, respectively. That for dark energy is 72.8 per cent. For the flat Universe, the critical density (ρ_{crit}) is defined as

$$\rho_{crit} = \frac{8H^2}{8\pi G},\tag{1.1}$$

where H is the Hubble constant and G is a gravitational constat. Also a density parameter is then defined as

$$\Omega = \frac{\rho}{\rho_{crit}}.\tag{1.2}$$

The total mass density of the Universe, which is the combination of matter and dark energy, is 1.0023±0.005 implying that it is "flat".

1.1.2 Hierarchical structure formation

The distribution of baryonic matter has been studied through various wide field surveys. We can observe stars, galaxies and galaxy clusters, where the mass density is many hundreds of times that of the mean density of the Universe. However the CMB is homogeneous on large scales and isotropic at the level of 10^{-5}. This indicates that the Universe has evolved from the CMB and the structures on large scales have been created through the influence of gravity.

In the ΛCDM framework, the origin of the Universe was the Big Bang. After the explosion a period of inflation occurred, which made the flat, homogeneous and isotropic Universe we observe in the CMB. However tiny fluctuations left after inflation became the seeds to create larger structures. When the matter dominated era began after the recombination epoch, matter could gravitationally contract around these tiny fluctuations. Dark matter played a key role in this assembly since it dominates gravitationally. So as the dark matter collapsed and generated haloes, it concentrated the baryons within these dark matter haloes, and lead to the formation of the first stars and hence galaxies. As time goes on, smaller dark matter haloes merged and larger, massive structures were created. Therefore the structure has grown from tiny seeds to the large scale structure we see today hierarchically.

1.2 Clustering

Understanding dark matter is important to describe the Universe accurately. Several indirect methods have been used to estimate various properties of the dark matter. One of them is the clustering of galaxies. It is believed that galaxies are formed at the centre of dark matter haloes by baryons falling into haloes (White & Rees 1978; Fall & Efstathiou 1980), and evolve with the haloes (White & Frenk 1991). Therefore the observed distribution of galaxy traces that of dark matter.

In order to estimate the distribution of galaxies statistically, their clustering can be used. Especially the two-point correlation function which shows the probability of a pair with respect to the random distribution is one of the most popular and simplest methods. With recent wide field surveys, the clustering properties of various

galaxy populations have been investigated. These clustering properties depend on the characteristics of galaxies such as luminosity, colour, morphology and stellar mass (Cole et al. 1994; Norberg et al. 2001, 2002; Zehavi et al. 2002, 2005; Coil et al. 2008; Ross & Brunner 2009; Foucaud et al. 2010; Hartley et al. 2010; Ross, Percival & Brunner 2010; Wake et al. 2011; Zehavi et al. 2011). The overall trends of the clustering for various populations are that luminous, red, passive and massive galaxies are more clustered than those having the opposite properties.

The dependence of clustering strength on the intrinsic properties of a galaxy can be translated into information of the dark matter halo hosting the galaxies, because the property of a galaxy is determined by its parent halo (Eke et al. 2004; Baugh 2006). Generally galaxies having a stronger clustering amplitude reside in more massive dark matter haloes. To link the clustering of galaxies with their dark matter haloes, the halo model, that includes properties such as halo mass function, halo density profile and halo bias, is required. In the halo model the galaxy power spectrum can be split into the 1-halo term, galaxy pairs in the same halo, and the 2-halo term, those from different haloes. In Cooray & Sheth (2002) the galaxy power spectra are given as

$$P(k) = P^{1h}(k) + P^{2h}(k), \tag{1.3}$$

$$P^{1h}(k) = \int dM n(M) \frac{\langle N(N-1)|M \rangle}{\overline{n}^2} |u(k|M)|^2, \tag{1.4}$$

$$P^{2h}(k) = P_{lin}(k) \left[\int dM n(M) b(M) \frac{\langle N|M \rangle}{\overline{n}} u(k|M) \right]^2, \tag{1.5}$$

where $n(M)$ is the halo mass function, $<N|M>$ is the number of galaxy, N, hosted by the dark matter halo having mass M, $b(M)$ indicates the halo bias function and $u(k|M)$ represents the density profile in Fourier space of the halo having a mass, M. The mean number density is described by $\overline{n}$ and $P_{lin}(k)$ is the linear power spectrum.

Firstly the halo mass function ($n(M)$) means the number density of halo as a function of halo mass (M). Press & Schechter (1974) introduced

$$n(M) dM = \frac{\overline{\rho}}{M} f(\nu) d\nu \tag{1.6}$$

and

$$\nu f(\nu) = \sqrt{\frac{\nu}{2\pi}} \exp(\frac{-\nu}{2}) \tag{1.7}$$

where ν is defined by $[\delta_{sc}/\sigma(M)]^2$. δ_{sc} means the critical density, and $\sigma^2(M)$ is the variance in the density field smoothed with a tophat filter. Recently Sheth & Tormen (1999), Tinker et al. (2008, 2010) provided the improved mass function showing a better fit with simulations. Secondly the halo density profile describes the distribution of dark matter around the centre of a halo. The profile mainly depends on the mass of the halo, since all parameters depend on the mass. In the halo model it is assumed that the distribution of satellite galaxies follows the distribution of dark matter in the halo. Finally the more massive dark mater halos are more strongly clustered than the overall mass distribution. The halo bias function expresses the mass dependence of the amplitude of fluctuations in the number of halos relative to fluctuations in the underlying mass distribution. At a given redshift more massive haloes have a higher bias meaning they are more clustered than less massive haloes. Also at a given halo mass, the bias is higher at higher redshift. Recently Tinker et al. (2010) demonstrated that massive, rare haloes have a higher bias than predicted by previous results. In Chapter 5 the halo model is fitted to the angular clustering of high redshift red galaxies. For that the halo mass and bias functions in Tinker et al. (2010) and the density profile by Navarro, Frenk & White (NFW, 1997) are adopted for this work. These three formulae are as follows,

$$\nu f(\nu) = \nu\alpha \left[1 + (\beta\nu)^{-\Phi}\right] \nu^{\eta} \exp(\frac{-\gamma\nu}{2}), \tag{1.8}$$

$$\rho(M, r) = \frac{M}{[cr/r_{vir}(M)] \left[1 + cr/r_{vir}(M)\right]^2} \frac{1}{4\pi \left[r_{vir}(M)/c\right]^3 \left[\ln(1 + c) - c/(1 + c)\right]}, \tag{1.9}$$

$$b(\nu) = 1 - A\frac{\nu^{a/2}}{\nu^{a/2} + \delta_{sc}^{a/2}} + B\nu^{b/2} + C\nu^{c/2}, \tag{1.10}$$

where α, Φ, η and γ in Equation 1.6 are parameters depending on redshift (see Tinker et al. 2010), and c and r_{vir} in Equation 1.7 indicate concentration parameter and virial radius, respectively. In Equation 1.8, a, A, b, B, c and C depend on Δ which is the critical overdensity for virialisation, assumed to be 200 for this work.

When applying the halo model, the mean number of galaxies in the dark matter halo at a given mass, $< N|M >$, must be also defined. The halo occupation distribution (HOD) describes the statistical relation between number of galaxies and the halo mass. Since galaxies in the same halo can be distinguished into a central galaxy and satellites, the HOD for the power spectrum of 1-halo term is also split into $< N|M >_{cen}$ and $< N|M >_{sat}$ for central and satellite galaxies, respectively. The simplest form for the HOD is a step function for the central galaxy and a power-law for the satellites. This means haloes above a certain mass threshold contain a central galaxy, but haloes below the threshold contain no galaxies. However the results from cosmological simulations present different features. The HOD of a central galaxy shows a smooth cutoff at the low mass regime. Zheng et al. (2005) introduced a modified form :

$$< N|M >_{cen} = \frac{1}{2} \left[1 + erf \left(\frac{\log M - \log M_{cut}}{\sigma_{cut}} \right) \right],$$ (1.11)

$$< N|M >_{sat} = \left(\frac{M - M_1}{M_0} \right)^{\alpha} (for M \leq M_1),$$ (1.12)

where erf is the error function, M_{cut} is the halo mass threshold for a central galaxy and σ_{cut} describes the width of cutoff profile for the HOD of central galaxy. In addition M_1 is the low mass cut for the satellite HOD, M_0 is the characteristic mass for satellites and α indicates the power law slope.

1.3 Galaxies at high redshift

1.3.1 Galaxy spectrum

Through optical and near-IR wavelengths we mainly detect photons from the stellar population of a galaxy. Old stellar populations, having low surface temperatures, emit their energy at longer wavelengths. On the other hand, young and hot stars also emit UV photons as well.

An early-type galaxy consists of mainly an old stellar population, such as K type star. The lack of UV emission leads to faint magnitudes at rest-frame wavelengths of < 4000Å. Also the spectra of old stars having low surface temperature show a

clear Balmer break at 4000Å. Thus, passive galaxies can be selected using a red colour measured by two bands covering the Balmer break. As well as the Balmer break, the key spectral features of early-type galaxies are absorption lines such as Ca II H and K lines (3969 and 3934Å) and G-band (4304Å).

On the other hand, star-forming galaxies containing young and hot stars emit photons at shorter wavelengths as well. The Lyman limit at 912Å and Lyman α line at 1216Å are key features of star-forming galaxies. The filters covering a rest-frame UV regime are useful to detect star-forming galaxies. Other important lines of star-forming galaxies are some emission lines such as [OII] (3727Å), Hβ (4861Å) and Hα (6563Å). However since UV photons are easily absorbed by dust in galaxies, dusty star-forming galaxies can be missed by the UV selection technique. In this case re-emitted energy at an infrared regime is best used to detect dusty galaxies. Figure 1.1 shows the example spectra of spiral (blue) and elliptical (red) galaxies from the EAZY template (Brammer et al. 2008). Dotted lines indicate key features mentioned.

1.3.2 Colour selection for high-z galaxies

Over the past few decades, several colour selection techniques for various galaxy populations at different redshifts have been developed. Through optical colours the UV continuum has been used to detect star-forming galaxies. Steidel & Hamilton (1992) used U_nGR filters to find high redshift quasars. This technique was also applied to find star-forming galaxies called as Lyman Break Galaxies (LBGs). Steidel et al. (1996) spectroscopically confirmed normal star-forming galaxies at $z > 3$ selected through this technique. It was extended to the BM/BX method by Adelberger et al. (2004). They used the same filter system and found star forming galaxies at slightly lower redshift $z \sim 1.7$ and $z \sim 2.3$ respectively. As well as the details of those populations, their clustering properties have also been studied from various wide field surveys. The correlation length which describes the clustering strength ranges from 3 to 6 h^{-1}Mpc (Foucaud et al. 2003; Adelberger et al. 2005).

On the other hand detecting passive galaxies at $z > 1$ with optical colour criteria may be more difficult, since the bulk of the stellar emission is redshifted into the
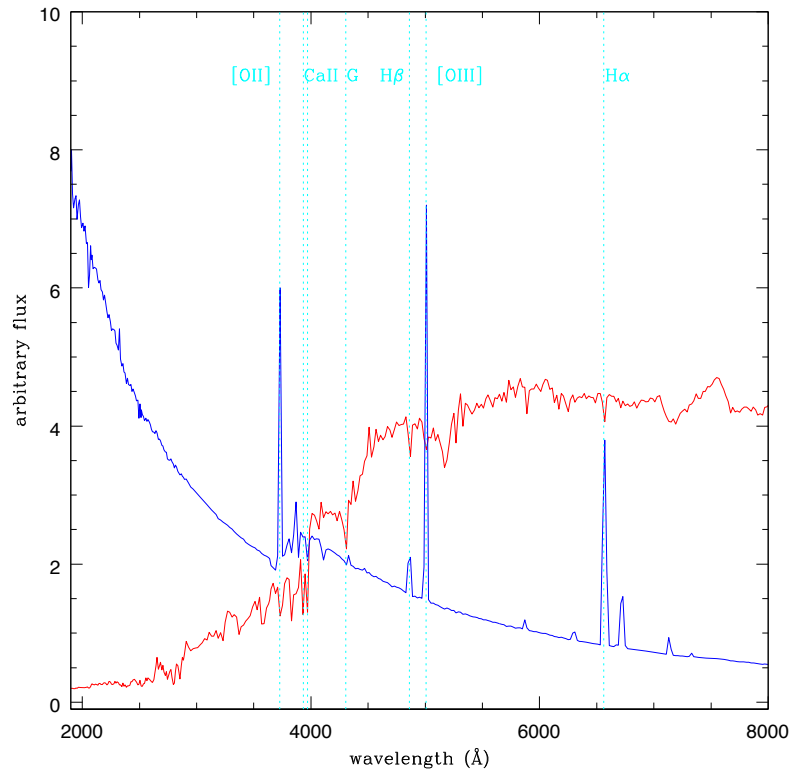
Figure 1.1: The example of galaxy spectra. Blue and red lines show spectra of spiral and elliptical galaxies, respectively, from the EAZY template (Brammer et al. 2008). Dotted lines indicate key features.

near-IR regime. Daddi et al. (2004) combined optical and near-IR filter sets to find galaxies at $z > 1.4$. They found that star-forming galaxies and passively evolved galaxies were distinguished in the $z - K$ versus $B - z$ diagram, which are referred to as $sBzK$ and $pBzK$ respectively. Additionally there are also more simple colour criteria to select high redshift, red galaxies. Elston, Rieke & Rieke (1988) proposed $(R - K) > 5$ for a new extragalactic population at $z > 6$ or passive galaxies at $z > 1$. These were named as the extremely red objects (EROs), and the redshifts of EROs were spectroscopically confirmed to be $0.8 < z < 2$ (Cimatti et al. 2002; Conselice et al. 2008). Furthermore distant red galaxies (DRGs) can be detected by their red near-IR colour, $J - K > 2.3$, since the 4000Å break of a high redshift galaxy at $z > 2$ is bracketed by the J- and K-bands (Franx et al. 2003). Recently it has been recognised that both populations are a mixture of dusty star-forming galaxies and passively evolved galaxies (Pozzetti & Mannucci 2000; Smail et al. 2002; Roche et al. 2002; Cimatti et al. 2002, 2003; Moustakas et al. 2004; Sawicki et al. 2005; Simpson et al. 2006; Conselice et al. 2008; Kong et al. 2009 for EROs and Labbé et al. 2005; Papovich et al. 2006 for DRGs). All three populations are also strongly clustered (Kong et al. 2006; Blanc et al. 2008 for BzK, Daddi et al. 2000; Roche et al. 2002, 2003; Brown et al. 2005; Kong et al. 2006, 2009 for EROs, and Grazian et al. 2006; Foucaud et al. 2007; Quadri et al. 2008 for DRGs). Like the galaxies sampled by morphology at lower redshift, passively evolved galaxies of $BzKs$, EROs and DRGs show larger correlation lengths than dusty star-forming populations (Blanc et al. 2008; Kong et al 2006, 2009).

In spite of the successful colour criterion, they are not enough to distinguish and to detect complete and uniform samples. As already mentioned EROs and DRGs are split into dusty-star forming galaxies or old, passive galaxies. In addition the UV selection technique is not appropriate to detect obscured galaxies. Quadri et al. (2007) cross-matched BM/BX/LBG, BzK and DRG populations selected from the Multiwavelength Survey by Yale-Chile (MUSYC). While they found that most $sBzK$ were selected as BM/BX/LBGs, BM/BX/LBGs did not recover $sBzK$s. Furthermore DRGs can be found in both BzK populations which indicates the existence of DRG at $z < 2$. Additionally, Lane et al. (2007) used the UKIRT Infrared

Deep Sky Survey (UKIDSS) UDS dataset to compare photometric properties of EROs, DRGs and BzKs. They also found the same result as Quadri et al. (2007). Comparing EROs with other populations, it was found that most of $pBzK$s and 32 per cent of $sBzK$s were identified as EROs, but 40 per cent of EROs were BzKs due to their redshift distribution. Also most DRGs were matched with EROs, which showed both red $R - K$ and $J - K$ colours. They pointed out that these joint EROs and DRGs were either low luminous AGNs or dusty star-forming galaxies at $z < 2$. The cross-matching between colour selected populations mentioned above indicates that a more careful analysis is necessary for the populations selected by their colours.

1.4 Galaxy clusters

The galaxy cluster is the most massive gravitationally bound system known and represents the most extreme environment in the Universe. A large galaxy cluster contains thousands of all types of galaxies within a few Mpc region. However the central region of cluster is usually dominated by red, elliptical galaxies. As well as galaxies, galaxy clusters hold large amounts of intergalactic gas which is referred to as the intracluster medium and emits X-rays. The total mass of galaxy clusters ranges from 10^{14} to a few times $10^{15} M_{\odot}$ with the invisible dark matter contributing most to the total mass.

The one of the most famous catalogues of galaxy clusters was compiled by George Abell in the mid 20th century. In 1958 George Abell published the catalogue containing 2,712 rich clusters in the northern hemisphere (Abell 1958). It was extended to the southern hemisphere in 1989 (Abell, Corwin & Olowin 1989). Fritz Zwicky who suggested the existence of dark matter also published a series of catalogues of clusters of galaxies from 1961 to 1968.

Galaxy clusters can be observed at various wavelengths for different components. Firstly the individual member galaxies can be studied at optical and infrared wavelengths. Since the distance to member galaxies is the same, the colour of a galaxy directly represents the galaxy type. In this context it is well known that elliptical galaxies, having red colours, form the clear sequence on the colour-magnitude di-

agram, called the red sequence. Since the colour of red sequence depends on the redshift of the cluster due to the redshifted spectral energy distribution, it can be used to find new galaxy clusters at various redshift ranges (Gladders & Yee 2000). Secondly X-rays are useful to detect the hot intracluster medium. It is observed as extended emission from the centre of galaxy cluster. Thus recent X-ray space telescopes have been used to detect extended sources to find new galaxy clusters. Thirdly the high energy electrons in clusters distort the CMB photons through the Sunyaev-Zel'dovich (SZ) effect. This effect creates a decrement in radio maps where clusters are. The SZ effect is also a way to find galaxy clusters. Finally galaxy clusters are the most massive systems and contain large amounts of dark matter. Dark matter plays a lensing like role and amplifies the light from background objects through gravitational lensing. We can measure the mass of dark matter in the galaxy cluster, and map the distribution of dark matter as well as detailed properties of the lensed background objects.

Now galaxy clusters are used not only to investigate galaxies in extreme environments of the galaxy cluster itself, but also to measure cosmological parameters. The abundance of galaxy clusters depends on cosmological parameters, $\sigma_8(\Omega_m)^{0.5}$, where σ_8 is the rms mass fluctuation amplitude in $8h^{-1}$ Mpc sphere in units of the critical density and Ω_m is the total matter density. The evolution of cluster abundance is especially sensitive to Ω_m (Eke et al. 1998). Moreover the abundance also depends on the dark energy, since the dark energy determines the expansion of Universe. Therefore the abundance of galaxy clusters is one of the key science goals of wide field surveys.

1.5   This work

Now we are in an era where various wide and deep surveys are being performed or planned. Surveys such as UKIDSS (Lawrence et al. 2007), the Panoramic Survey Telescope and Rapid Response System (Pan-STARRS, Kaiser & Pan-STARRS team 2002), the Dark Energy Survey (DES[1]), the Visible and Infrared Survey Telescope for

---

[1]www.darkenergysurvey.org

Astronomy (VISTA[2]) and the Large Synoptic Survey Telescope (LSST[3]) will provide opportunities to measure the accurate clustering of galaxies and to investigate details of galaxy clusters. In this thesis we present results of the clustering of high redshift red galaxies such as EROs and DRGs, halo modelling for EROs and galaxy cluster candidates at $z \sim 1$ based on the UKIDSS Deep eXtragalactic Survey (DXS, Edge et al., in preparation).

Chapter 2 mainly describes the details of the DXS which is one of the sub-surveys in UKIDSS. There are some known issues caused by the UKIDSS standard pipeline, which need to be addressed in order to make reliable photometric catalogues. Details of these issues and the strategy for better photometric catalogues are described. Also, additional science areas covered by the DXS that are not the primary aim of this thesis are also presented.

Chapters 3 and 4 show the angular correlation functions of high redshift red galaxies such as EROs and DRGs in two DXS fields. The widest survey datasets ever studied for those populations are used to measure the angular correlation function. Unlike previous studies, we demonstrate that the angular correlation function of those populations can not be described by a single power-law. Furthermore the dependence of clustering on colour and redshift are also discussed.

In Chapter 5, the halo model fit for EROs at different redshifts is performed. It is demonstrated that the standard halo model with the ΛCDM cosmology is appropriate to describe the clustering of EROs. The result of halo model fit is also compared with semi analytical model predictions.

Chapter 6 describes the study of galaxy clusters in one of the DXS fields. We explain the selection algorithm based on the red sequence of galaxy cluster. The spectroscopic confirmation for some candidates are also displayed. From the candidates the angular clustering of galaxy clusters is measured and compared with previous works and ΛCDM cosmology.

The area covered for this study is a few deg^2 which is one of the widest datasets including the near-IR photometric catalogue to date. We expect that the completed

---

[2]www.vista.ac.uk

[3]www.lsst.org

UKIDSS datasets and future wider field surveys will be useful to measure more accurate clustering and to detect more galaxy clusters. All results from this work demonstrate the reliability of future work for the more accurate measurement by wider and deeper surveys in the future.

Chapter 2

UKIDSS

2.1 Introduction

Wide and deep surveys play an important role in our understanding of the structure of the Universe. Above all, the near-IR regime must be included to detect $z > 1$ galaxies, since the bulk of their stellar emission is redshifted into this range. However performing such surveys, especially a near-IR survey, has been impossible due to the lack of an instrument with a sufficiently large field of view. Recently, several cameras have allowed us to do this efficiently.

The UKIRT Infrared Deep Sky Survey (UKIDSS) began in 2005 and consists of 5 sub-surveys covering various areas and depths (Lawrence et al. 2007). UKIDSS uses the Wide Field Camera (WFCAM, Casali et al. 2007) mounted on the UK Infrared Telescope (UKIRT). WFCAM is composed of four Rockwell Hawaii-II 2K×2K array detectors (Casali et al. 2007). The pixel scale is 0.4 arcsec/pixel, so the size of each detector is 13.7×13.7 arcmin^2. The relatively large pixel scale can lead to an undersampled point spread function. To avoid this problem microstepping is applied. In addition there are gaps between detectors, and the width is similar to the size of a detector. Therefore four exposures are needed to make a contiguous image, i.e. the 4×4 image tiling ∼0.8 deg^2. Figure 2.1 shows the focal plane of the WFCAM.

There are five sub-surveys in UKIDSS to study a wide range of astronomical goals from our galaxy to the distant Universe. The Large Area Survey (LAS) is

15

Figure 2.1: The focal plane of WFCAM. Four arrays and auto guider are presented. The readout direction is shown on the first array. (Dye et al. 2006)

Table 2.1: The four UKIDSS DXS fields

Field	area ($\deg^2$)	RA	Dec
XMM-LSS	8.75	02 25 00	-04 30 00
Lockman Hole	8.75	10 57 00	+57 40 00
Elais-N1	8.75	16 10 00	+54 00 00
SA22	8.75	22 17 00	+00 20 00

the widest survey of the UKIDSS sub-surveys. The LAS covers 4,000 $\deg^2$ in the northern hemisphere, and studies cool stars in the Galaxy to $z > 6$ quasars. The Galactic Plane Survey (GPS) maps 1,800 $\deg^2$ of the Galactic plane to constrain stellar evolution, star formation and the initial mass function. The Galactic Clusters Survey (GCS) traces 10 open clusters and star-formation associations. The stellar mass function and initial mass function are the science goals of the GCS. The Deep eXtragalactic Survey (DXS) images four different regions to study distant galaxy clusters and galaxy clustering at $z > 1$. Finally the Ultra Deep Survey (UDS) is a single field with WFCAM tiling. It is the deepest near-IR survey on $\sim$50 arcmin scales and will study the formation epoch of elliptical galaxies and the growth of structure and bias since $z = 3$. The depth of the LAS, the shallowest survey of UKIDSS, is $K_{vega} = 18.2$ which is three magnitudes deeper than the Two Micron All Sky Survey (2MASS, Skrutskie et al. 2006).

In this Chapter, the details of the DXS are explained. Also known issues of the standard pipeline are checked and additional processes to get a better photometric catalogue are discussed. Finally the science goals of the DXS are introduced. Unless otherwise noted, all magnitudes are in the Vega scale in this Chapter.

2.2   UKIDSS DXS

Of the 5 sub-surveys of UKIDSS, the DXS is a deep, wide survey mapping 35 $\deg^2$ with 5σ point-source sensitivity of $J \sim 22.3$ and $K \sim 20.8$. It comprises 4 fields and aims to create photometric samples at $z \sim 1 - 2$.

Table 2.1 lists the name, surveyed area and position of the four DXS fields. All fields are also mapped by other surveys at various wavelengths such as the

Panoramic Survey Telescope and Rapid Response System (Pan-STARRS, Kaiser & Pan-STARRS team 2002), the Spitzer Wide-area InfraRed Extragalactic (SWIRE, Lonsdale et al. 2003) survey and CFHT Legacy Survey (CFHTLS). This wide photometric coverage allows us to detect high redshift galaxies efficiently. The DXS samples the rest frame optical regime of galaxies at $z > 1$. The main scientific goals of the DXS are 1: to detect a large sample of galaxy clusters at $1.0 < z < 1.5$ in order to constrain cosmological parameters, 2: to measure galaxy clustering and bias at $z > 1$, 3: a multiwavelength census of starburst galaxies and AGNs to study the contribution of each to the global energy budget.

This thesis mainly concentrates on the clustering of red galaxies at high redshift and searching for galaxy clusters based on the DXS dataset. In order to apply colour selections or to measure photometric redshifts, an accurate photometric result is required.

2.3 DXS catalogue

2.3.1 Known issues

The observed images are processed with the UKIDSS standard pipeline (Lawrence et al. 2007) by the Cambridge Astronomical Survey Unit[1] (CASU). Also the processed and calibrated UKIDSS data can be downloaded from the WFCAM Science Archive[2] (WSA, Hambly et al. 2008). However Foucaud et al. (2007) pointed out that creating a contiguous image before extracting the catalogue is more helpful to optimise the depth in overlapping regions and to make a homogeneous image. There are also some known issues that require particular care when analysing WFCAM data.

There are many spurious objects caused by bright stars. Firstly, Dye et al. (2006) investigated the cross-talk caused by bright stars. The cross-talk features occur at multiples of 128 pixels (256 pixels for the DXS because of microstepping) away from

---

[1]http://www.ast.cam.ac.uk/ mike/casu/
[2]http://surveys.roe.ac.uk/wsa/

a bright star in the readout channel direction. The magnified picture in Figure 2.2 shows an example of cross-talk. The brightness and shapes of cross-talk depends on the host star. Secondly, diffraction spikes of saturated stars can also result in spurious objects. In the case of a WFCAM image, 8 spikes are generated toward vertical, horizontal and diagonal directions.

Moreover, total magnitudes such as Petrosian in the archive are unreliable. The left panel of Figure 2.3 displays the magnitude difference between aperture and Petrosian magnitudes of all stars defined by the class parameter in the dxsdetection table (class=-1) from the WSA catalogue. In the left panel it is apparent the magnitude difference is scattered, which indicates the Petrosian magnitude is brighter. This is caused by close neighbours of stars. The right panel is the same as the left panel, but stars having neighbours within 6″ are removed. It is apparently found that the scatter is reduced. In addition it is also known that the Kron radius for total magnitude of a galaxy is unreliable. Therefore the standard CASU detection pipeline is not optimised for galaxy photometry so we choose to create our own photometric catalogues from the mosaicked images.

2.3.2 Removing spurious objects and completeness

In this thesis, the main focus is distant galaxies located at $z > 1$. Their fluxes are important to distinguish populations, to reduce contamination and to measure their photometric redshift. Thus we reprocessed the photometric calibration, to ensure the best photometric catalogues.

First, deep stack images were downloaded from the WSA. These images come flat-fielded and with dark current and thermal background subtracted. Moreover astrometric and photometric solutions are contained in image headers. Therefore all preparations for making a contiguous image are already completed. Four 2K×2K arrays are mounted on the Wide Field Camera, and there are gaps between each array. To generate a contiguous map covering ∼0.8 deg^2, four pointings are required.

Second, we made a contiguous image from downloaded images by using the Swarp package (Bertin et al. 2002). Since varying sky levels on each image can lead to erroneous fluxes if one large area image is made, we stacked images in the only
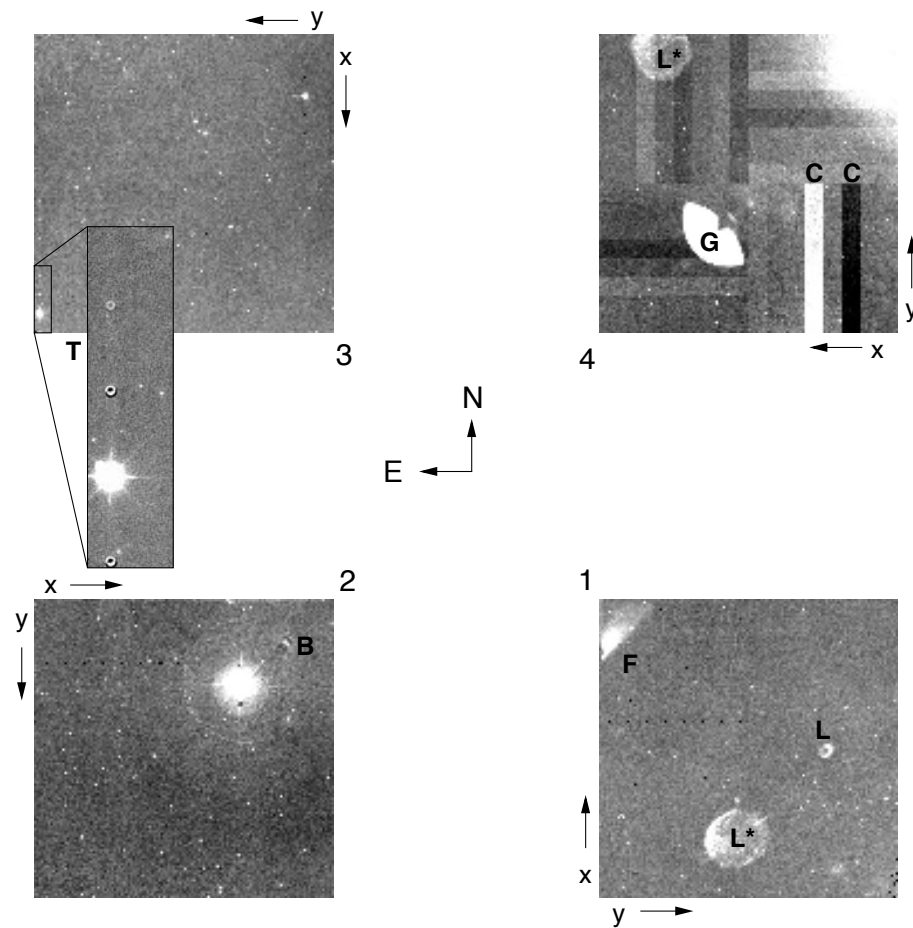
Figure 2.2: The sample image of WFCAM. Spurious objects are also displayed on each array. The magnified figure show the cross-talk of bright star (Dye et al. 2006).
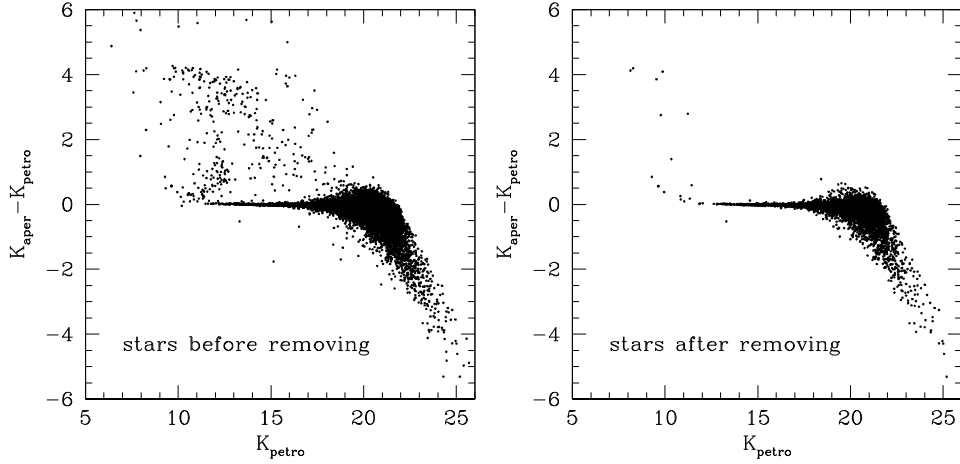
Figure 2.3: The difference of aperture and Petrosian magnitude of stars versus Petrosian magnitude. The left panel shows plot for all stars. The right panel presents the plot after removing objects having a close neighbour. The scatter is decreased after removing objects having a neighbour.

same region mapping $\sim$0.8 deg^2. Flux scaling was applied using the zero magnitude information contained in the image during stacking. Moreover in order to measure galaxy colours from the same region of galaxies, J-band images were aligned to K-band images using the GEOMAP and GEOTRAN tasks in IRAF.

Third, astronomical objects were detected from the contiguous image using SExtractor (Bertin & Arnouts 1996). To run SExtractor, the final threshold was determined after running SExtractor with various thresholds. Also, a gaussian filter was used to detect faint objects, and dual mode with K-band image as the detection image was applied. The aperture magnitude within a 1 arcsec radius was used to measure colour, and AUTO magnitude measured using the Kron radius was used to assign the total magnitude of objects.

Fourth, bright point sources in the WSA catalogue were used for photometric calibration. The WSA stacks are already calibrated using the 2MASS catalogue. Since the total magnitude of the WSA archive is not reliable, calibrated aperture magnitudes from the archive were extracted. Then total magnitudes of stars in the new catalogue were compared to the WSA aperture magnitudes for calibration.

Finally, spurious objects, cross-talk and spikes, were removed. The cross-talk

candidates were selected from their relative positions from bright stars, i.e., n×256 pixels. However candidates selected only by position may also contain a non-negligible fraction of real objects. The top panel of Figure 2.4 shows the relation between K-band magnitude of cross-talk candidate and their host stars at each position from 1×256 to 6×256 pixels. The dependence of cross-talk is presented for bright host stars. However there is a vertical distribution at fainter magnitude ($K_{host} = 13 - 16$). To decide whether this feature is from cross-talk or real objects, we used the dark spots around cross-talk candidates, which have negative pixel values. This was also reported by Williams et al. (2009). The inverse image of K-band image was created, and then the dark spots were detected by running SExtractor. After matching dark spots with cross-talk candidates of faint stars ($13 < K < 16$), the candidates accompanying a dark spot were determined as cross-talk. On the other hand all candidates of bright stars were regarded as cross-talks. In the bottom panel of Figure 2.4 showing the relation after filtering, it is shown that most cross-talk candidates of faint stars are not cross-talk but real objects. Furthermore bright, saturated stars ($K < 11$) also make spurious objects on diffraction spikes around the star. Vertical and horizontal spikes are tilted approximately 2.5 degrees, and diagonal spikes are well aligned at a 45 degree angle. Therefore we removed detected objects satisfying these positions from host stars. Figure 2.5 shows the colour-magnitude diagram for one of the SA22 fields before (top) and after (bottom) removing spurious objects. As shown in Figure 2.5, most objects having extreme colours are dominated by spurious objects at the DXS J and K limit.

The limiting magnitude goals of the UKIDSS DXS are $J = 22.3$ and $K = 20.8$ with the 5σ point source detection. In order to check the limiting magnitude of new catalogues and the quality of DXS data, an artificial star test was performed. Firstly an artificial star list containing 1,000 objects with random position and magnitude was created by STARLIST task of IRAF. Any artificial star located in a masked region was removed. Secondly the remaining artificial stars were added to DXS science images by MKOBJECTS task of IRAF. A gaussian profile was assumed as the point spread function of stars with the full width half maximum defined from stars in the original DXS image. Thirdly SExtractor was run with the same parameters
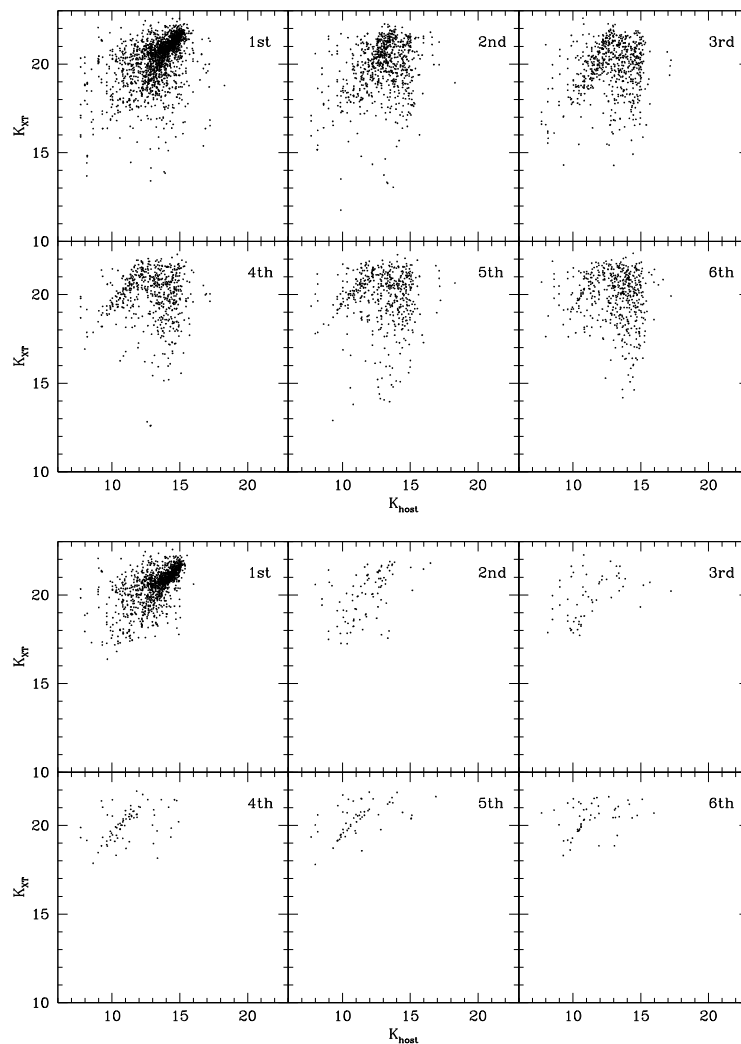
Figure 2.4: The relation between K-band magnitudes of potential cross-talk and host stars. The apparent dependence of the cross-talk is shown for bright stars. However there is also a vertical feature at $12 < K_{host} < 15$ (top). The bottom panel is the same plot after using an inverse image to find cross-talk. Most cross-talk candidates of faint stars are removed, i.e. they are real objects.
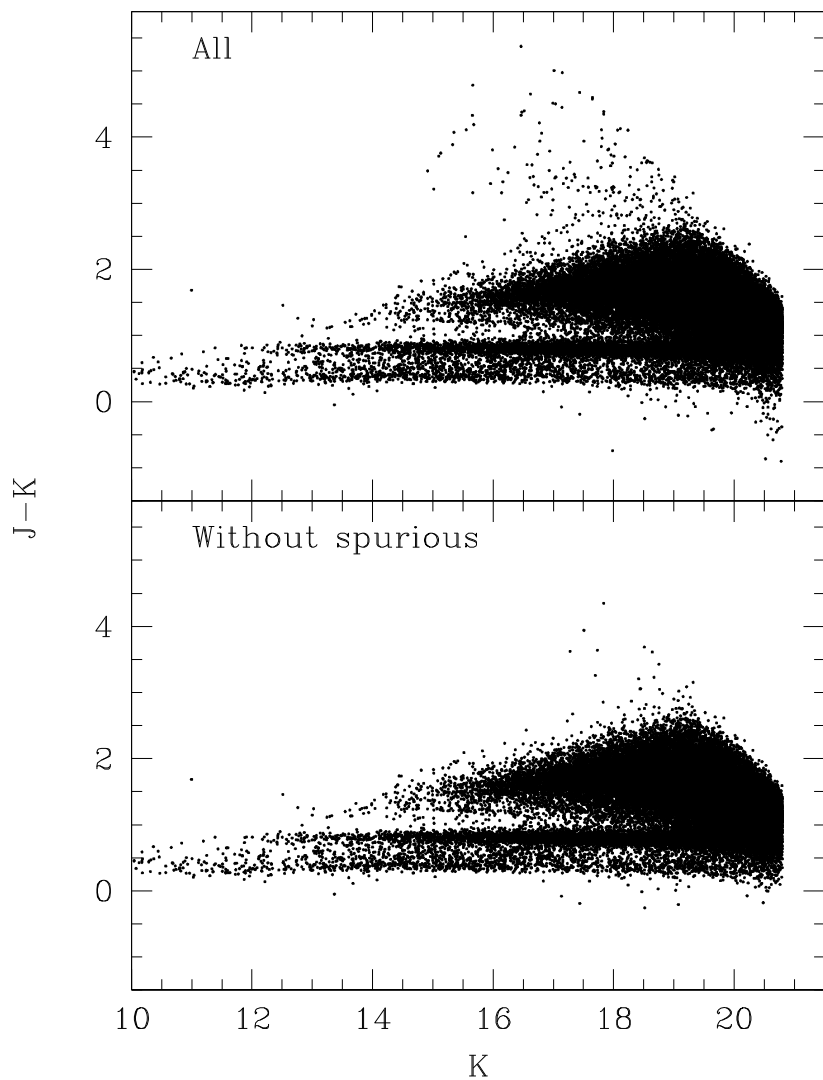
Figure 2.5: The colour-magnitude diagram for one of the SA22 fields before (top) and after (bottom) removing spurious objects.

as the scientific catalogue. Finally the detected objects were matched with the artificial star list, and the completeness was estimated. The SExtractor parameters were optimised for the K-band image. However to measure the completeness on the J-band image, the same parameters were used. It is noted that the parameters were also appropriate to detect objects and to reduce the contamination from noise on the J-band image. Figure 2.6, 2.7 and 2.8 are completeness test results for SA22, Elais-N1 and Lockman Hole, respectively. For the SA22 field, DXS images in data release (DR) 5, 7 and 8 were used. The images for Elais-N1 were from DR7 and DR8. The DR6 images were used for the Lockman Hole field. The quality of all images satisfies the DXS magnitude goals. It is possible that the completeness estimated by point sources and extended sources may show different results. We note that the completeness measured using artificial galaxies is 90 per cent at $K \sim 20.4$ which is 0.4 magnitude brighter than that from point sources. The field-to-field differences in completeness and source dependence of completeness may imply the systematic effect to our analyses, if we use very faint objects. In order to minimise the effect, we apply a K magnitude cut for our analysis.

In order to check the fraction of noise detected as astronomical objects, the inverse K-band image was created. We assume that noise accompanying negative pixels on sky-subtracted images is symmetric with the positive noise. SExtractor was run again for the inverse image, and then detected pixels were matched to the science catalogue. We assume that the matched objects in the science catalogue are noise. The fraction of false detections is 0.02 per cent at $K = 20.75$. Therefore we conclude the influence of a false detection is not significant.

2.4   Additional DXS Science

This work focuses on investigating galaxy clusters and galaxy clustering. However the depth and wide area of the DXS also allow other science to be addressed such as detecting K-band excess (KX) quasars and brown dwarves. In this section, these areas are briefly introduced. For this section, the catalogues merged with Pan-STARRS for Elais-N1 and CFHTLS for SA22 were used. The details of the optical
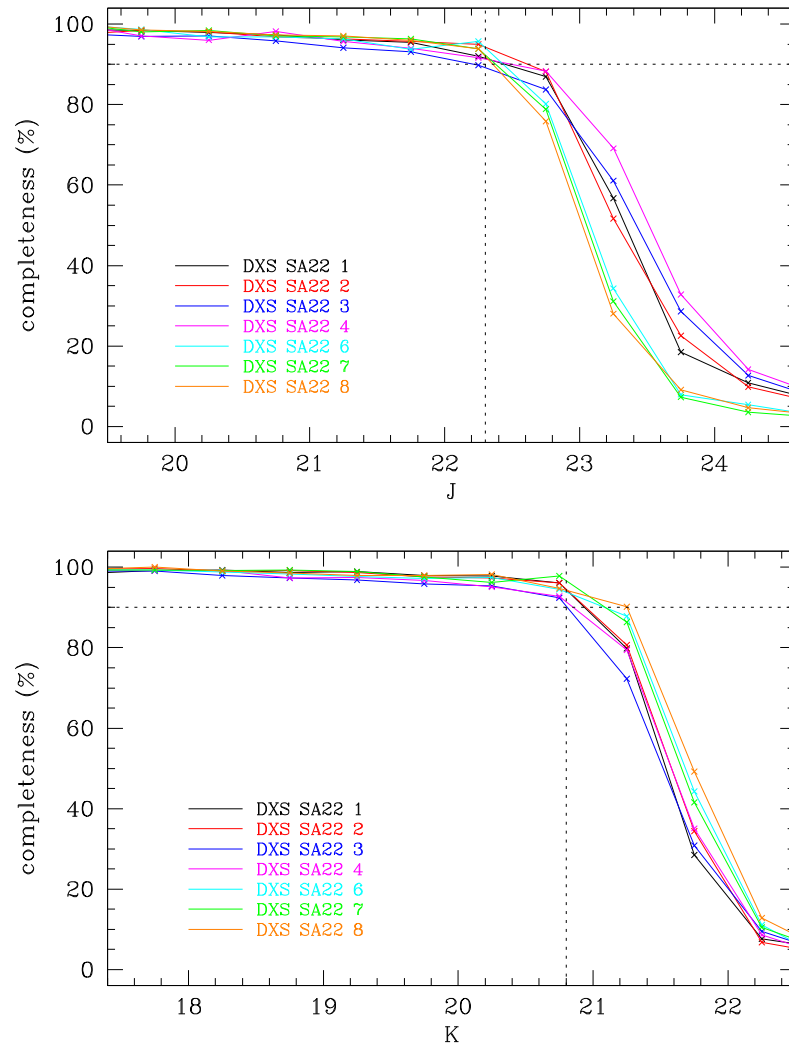
Figure 2.6: The completeness of point sources for the SA22 field. Dotted lines indicate 90 percent level (horizontal) and magnitude goal of the DXS. Each line corresponds to a ∼0.8 deg^2 sub-field
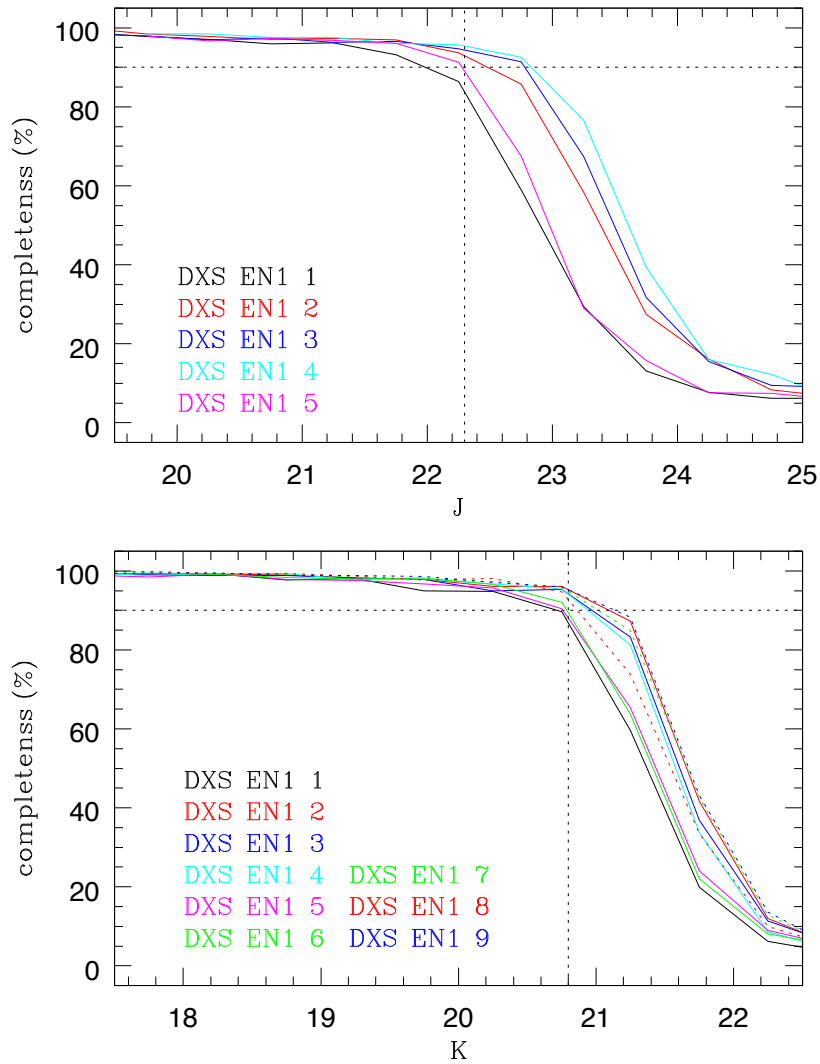
Figure 2.7: The completeness of point sources for the Elais-N1 field. Dotted lines indicate 90 percent level (horizontal) and magnitude goal of the DXS. Each line corresponds to a ~0.8 deg^2 sub-field
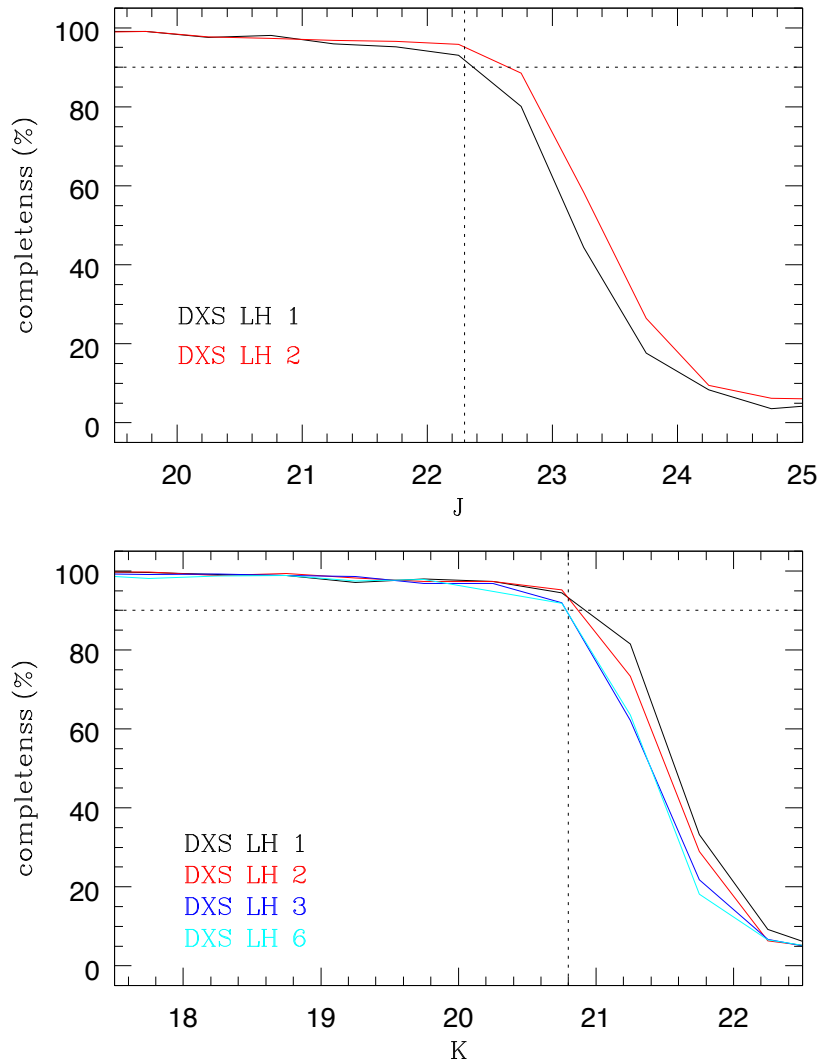
Figure 2.8: The completeness of point sources for the Lockman Hole field. Dotted lines indicate 90 percent level (horizontal) and magnitude goal of the DXS. Each line corresponds to a ~0.8 deg^2 sub-field

datasets are described in Chapter 4 for Pan-STARRS and Chapter 6 for CFHTLS.

2.4.1 KX quasars

The spectral energy distribution (SED) of quasars shows a clear discrepancy from stars. The excess of flux at short wavelengths allows us to find quasars, which is called as the UV excess (UVX) method. However the selection method through optical pass bands may miss quasars having a different SED from a standard power-law, or located at the high redshift. Moreover the UVX selection method is not suitable to detect obscured quasars, since short wavelengths are significantly affected by dust reddening.

In order to overcome these problems, Warren et al. (2000) suggested a new method which is similar with the UVX method but uses optical and near-IR colours, $V - J$ and $J - K$. The SED of quasars shows a clear excess at K-band compared with that of stars. Thus quasars have a similar $V - J$ colour and a redder $J - K$ colour than stars. This method is known as the KX method. In addition it can select obscured quasars as well as optically selected quasars, because the KX method is less sensitive to colour changes by reddening. Croom et al. (2001) demonstrated the feasibility of the KX method for wider near-IR surveys. Maddox et al. (2008) used $g - J$ and $J - K$ colours from UKIDSS LAS and SDSS datasets to study characteristics of quasars selected by the KX method. Also Smail et al. (2008) identified 17 KX quasars at $1.57 < z < 3.29$ from a pilot survey in the UKIDSS UDS field.

Here we simply consider the $g - J$ versus $J - K$ diagram of DXS Elais-N1 and SA22 fields to show the possibility of detecting KX quasars from the DXS. Firstly the DXS catalogues of Elais-N1 and SA22 were merged with Pan-STARRS and CFHTLS, respectively. Secondly the aperture magnitude difference by $0.8''$ and $2.0''$ apertures was applied to select point like sources. From the magnitude difference, objects having the same value as stars were selected. Figures 2.9 and 2.10 display two-colour diagrams of only point like sources for Elais-N1 and SA22, respectively. A K-band magnitude cut ($13.0 < K < 18.0$) was applied for bright quasar candidates, since the difference of aperture magnitudes for faint galaxies may
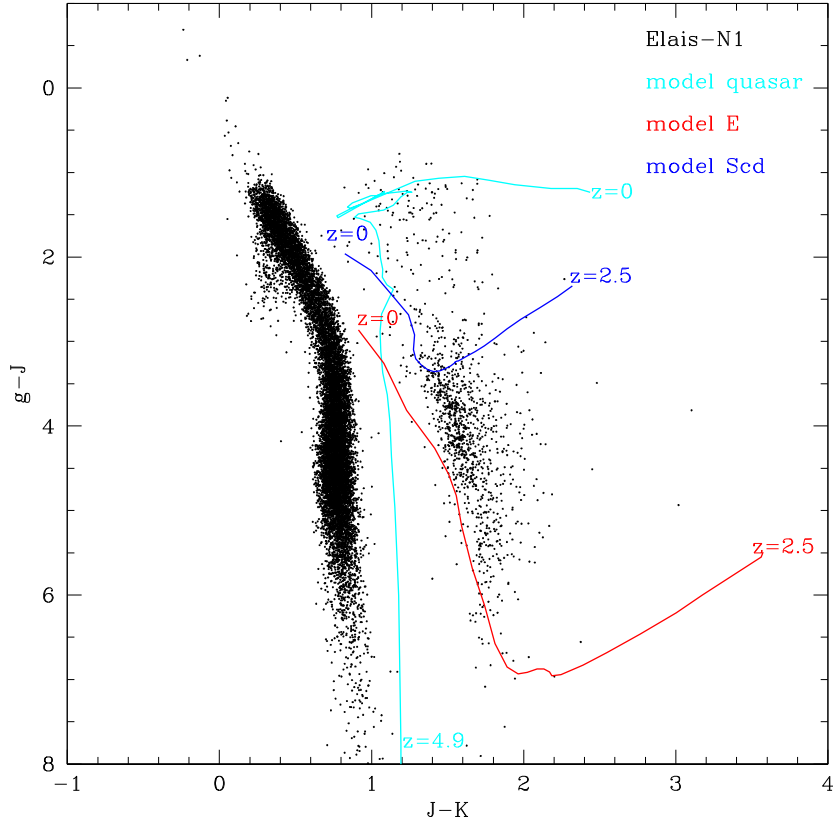
Figure 2.9: The $g - J$ versus $J - K$ diagram of point sources in Elais-N1. The cyan line tracks the colour of model quasars at various redshifts from Hewett et al. (2006). Red and blue lines indicate colours of elliptical and Scd galaxies at various redshifts.

contaminate the point sources. The stellar locus is well distinguished at blue $J - K$ colour regime. It is noted that different widths of stellar loci in two fields are caused by the optical datasets. The CFHTLS has a similar observational parameters as the DXS, but the seeing of Pan-STARRS is larger than the DXS. Since a KX quasar has relatively blue $g - J$ and red $J - K$ colours, objects following the model quasar track (cyan) are KX quasar candidates. They are also well distinguished from elliptical (red) and spiral (blue) galaxy tracks. Although the spectroscopic confirmation is necessary, it proves that the DXS dataset is useful to detect KX quasars.
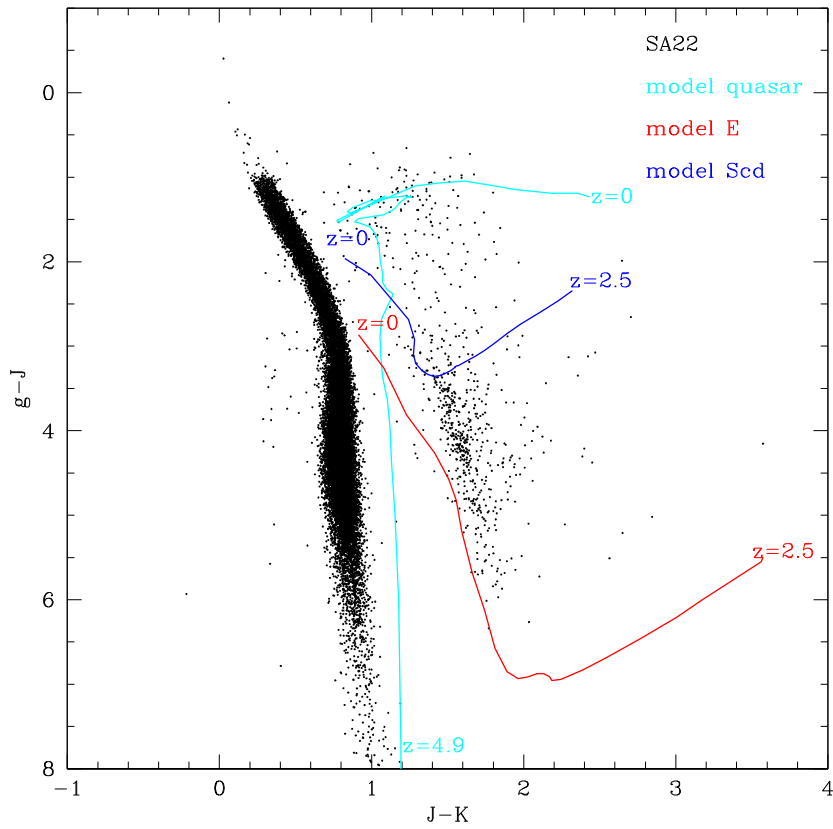
Figure 2.10: The $g-J$ versus $J-K$ diagram of point sources in SA22. The cyan line tracks the colour of model quasars at various redshifts from Hewett et al. (2006). Red and blue lines indicate colours of elliptical and Scd galaxies at various redshifts.

2.4.2 T dwarves

Brown dwarves are one of the coolest objects known. The mass of brown dwarves ranges between giant planets and low mass stars. The T dwarf is the coolest sub-population of brown dwarves ($T < 1400K$, Golimowski et al. 2004). The spectral energy distribution of T dwarves is shaped by water and methane in the near-IR wavelength regime (Burgasser et al. 2006). Finding cool stars is one of the main science goals of the LAS. However the DXS is also appropriate to do this because of its wide area and depth. Lodieu et al. (2009) found two T type brown dwarves from the DXS. In this section, T dwarf candidates are found from the DXS and other optical photometric datasets.

In order to find T dwarf candidates, the SA22 and Elais-N1 fields were used, since there are also deep optical datasets such as CFHTLS, Pan-STARRS, SDSS and Subaru catalogues. First a blue near-IR colour cut and K-band depth limit ($J - K < 0$ and $K < 21$) were applied for the initial selection. Second J and K images of the initial candidates were checked to remove spurious objects from cross-talk or bright stars. Third the optical counterparts of candidates were found from CFHTLS and SDSS for the SA22, and Pan-STARRS, Subaru and SDSS for the Elais-N1. Knapp et al. (2004) introduced various optical and near-IR colours of L and T dwarves. Therefore colours of matched candidates can be used to determine whether the candidate is a brown dwarf or not. Unfortunately none of our matched objects satisfy the colour for L and T dwarves suggested in Knapp et al. (2004). Figure 2.11 shows the $z - J$ versus $i - z$ diagram to display rejected objects (filled circles) and colours of known M (magenta), L and T dwarves (red) in Hewett et al. (2006). Finally 8 candidates were left, one of which was already reported in Lodieu et al. (2009). Table 2.2 lists fields, positions, $J - K$ colours and K-band magnitudes. Spectroscopic observations or methane imaging are required to confirm the candidates as T dwarves.
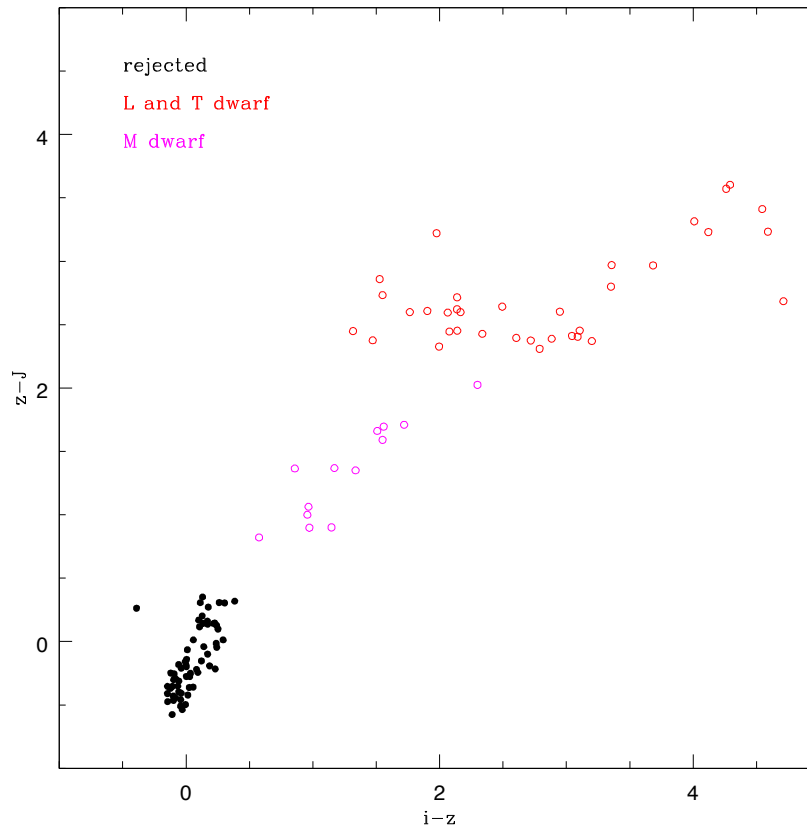
Figure 2.11: The $z-J$ versus $i-z$ diagram for brown dwarves. Filled circles indicate rejected objects from T dwarf candidates. Magenta and red open circles show known M dwarf and L, T dwarves, respectively, from Hewett et al. (2006).

Table 2.2: New T dwarf candidates in DXS SA22 and DXS Elais-N1 fields.

Field	RA (deg)	Dec (deg)	$J - K$	K
SA22	333.7711118	0.5147362	-0.0758±0.1071	19.9091±0.0834
SA22	333.6674734	-0.9368084	-0.0297±0.2211	20.9088±0.2175
SA22	333.3564590	-0.7344558	-0.3101±0.1479	20.6635±0.1262
SA22	334.2522547	-0.5930759	-0.2132±0.2264	20.8315±0.1238
Elais-N1	241.1395222	54.7037226	-0.0313±0.1780	20.4276±0.1280
Elais-N1	243.4738828	55.4119708	-0.2245±0.2021	20.4941±0.1284
Elais-N1	243.5089425	55.4294800	-0.1299±0.0779	20.2805±0.0715

2.5   Summary

We have used UKIDSS data to investigate the large scale structure at high redshift in this thesis. The DXS is a wide and deep near-IR survey covering 35 deg^2. In this section we presented the strategy for a reliable photometric catalogue.

There are some known issues in the UKIDSS standard pipeline such as spurious objects due to cross-talk and diffraction spikes caused by a bright star, and unreliable total magnitudes. We reduced the fraction of spurious objects and reprocessed the photometric calibration, using the stacked DXS images. The completenesses estimated by an artificial star test are over 90 per cent at $J_{vega} = 22.3$ and $K_{vega} = 20.8$ which satisfy the magnitude goals of the DXS.

We also introduced the feasibility of additional DXS science goals which are not included in this thesis. The KX method is a useful technique to find quasars. Merging the DXS catalogues with deep optical datasets, we found that candidate KX quasars are well distinguished from a stellar locus and other galaxy populations on the colour-colour diagram. Brown dwarves are also well detected through near-IR datasets, since their effective temperature is low. Using $J - K$ colours and optical counterparts, we found 7 candidate T dwarves from DXS SA22 and DXS Elais-N1 fields.

Through the rest of this thesis, we mainly discuss the main science goals of the DXS. The DXS is efficient in detecting high redshift galaxies such as EROs and DRGs. We investigate their clustering properties, using an angular correlation functions and a halo model. Furthermore galaxy clusters in the DXS SA22 field are identified, and we compare their clustering properties with the prediction of the ΛCDM model.

Chapter 3

Clustering of EROs and DRGs in the SA22

3.1 Introduction

The Lambda cold dark matter (ΛCDM) paradigm predicts that small scale structure has developed by accretion and mergers within the large scale structure generated by primordial mass fluctuations. In addition, the galaxies tracing this structure are themselves embedded and have evolved in dark matter haloes (White & Frenk 1991). The halo properties such as abundance, distribution and density profile depend on the mass of the halo (Cooray & Sheth 2002). As a result, the formation and evolution of galaxies is affected by the halo mass (Eke et al. 2004; Baugh 2006). Therefore the clustering properties of galaxies can be related to the distribution of dark matter haloes, and hence offer an important insight into the relationship between the halo and the galaxies within it. For instance, Wake et al. (2008) used correlation functions and halo models to demonstrate that Luminous Red Galaxies (LRGs) are frequently located in the centre of the most massive dark matter haloes, and that changes in their small scale clustering with redshift can constrain LRG-LRG merger rates. At higher redshifts, Mo & White (2002) pointed out that haloes of a given mass are expected to be more clustered from simulations. Observationally Foucaud et al. (2010) have demonstrated that galaxies with higher stellar masses are more clustered, and galaxies with a fixed stellar mass are also more clustered

at higher redshift. Hartley et al. (2010) have also shown that passive, red galaxies are more clustered than star-forming, blue galaxies of similar absolute magnitudes at $0.5 < z < 3.0$. Quadri et al. (2008) found that a double power law was required to describe the correlation function of DRGs at $2 < z < 3$, but were unable to fit their clustering measurement and space density simultaneously using the halo model. Tinker, Wechsler & Zheng (2010) showed that using a more realistic halo model they could better fit this clustering measurement, but they still required that the observed region be a more clustered part of the universe than is typical. However, most observational studies of clustering and the halo model have concentrated on relatively low redshifts ($z < 1$) so their evolution has been poorly constrained. With the advent of large near-infrared surveys, it is now possible to apply these techniques to more distant galaxies. The study of the angular clustering of $z > 1$ galaxies is particularly powerful as the near constant angular diameter distance in the $1 < z < 3$ range means that angle and comoving distance are much more closely linked than at lower redshift. Therefore, any characteristic distance (halo transition or sound horizon at recombination) will translate to a small range in angle.

Despite all of the successful photometric selection methods for high redshift galaxies, the small field of view of imaging cameras has hampered the accurate measurement of large scale clustering. In particular, the lack of wide field near-IR instruments has prevented the detection of distant, passive galaxies since the bulk of their emission is redshifted to longer wavelengths. However, new wide and deep near-IR surveys now provide an opportunity to investigate the clustering properties of galaxies at high redshift. In this Chapter, we use the wide contiguous near-IR data from 5th Data Release (DR5) of the Deep eXtragalactic Survey Data (DXS), which is the sub-survey of the UK Infrared Telescope Infrared Deep Sky Survey (UKIDSS) (Lawrence et al. 2007), in conjunction with *gri* optical data from the CTIO 4m to measure the clustering properties of EROs and DRGs, and discuss the clustering properties with various criteria.

Unless otherwise noted, the photometry is quoted in the Vega scale in this Chapter. We also assume $\Omega_m = 0.27$, $\Lambda = 0.73$ and $H_o = 71$ km s^{-1} Mpc^{-1}.

3.2 Observation

3.2.1 UKIDSS DXS

In this Chapter we deal with a $\sim$3.3 deg^2 portion of the SA22 field centred on $\alpha = 22^h\ 19^m\ 17.0^s$, $\delta = +00^d\ 44^m\ 00.0^s$ (J2000) from UKIDSS DR5. Since it is composed with four 0.8 deg^2 fields from DXS SA22 1 to 4, there is a 16-point mosaic to cover the field. The DXS SA22 1 corresponds to the south-west part of our field, and SA22 2, 3 and 4 are south-east, north-east and north-west, respectively. Seeing conditions of all images were $\sim$0.9$''$ at J and $\sim$0.8$''$ at K.

3.2.2 Optical data

Optical gri images were obtained from the 4m Blanco Telescope in Cerro Tololo Inter-American Observatory (CTIO) in September 2006 to complement the DXS as the SA22 field lacked any wide field optical imaging. The observations were performed by Mosaic II CCD composed with eight 2K$\times$4K detectors. Each exposure covers 36$\times$36 arcmin^2, and 9 fields were observed to map $\sim$3.3 deg^2 of the UKIDSS DXS SA22 field. Total exposure times are 1,800 seconds for g and 3,000 seconds for r and 5,400 seconds for i. In addition, 5- or 9-point dithering methods were applied for g, r and i respectively. The seeing was 1-2$''$ for g and 1-1.5$''$ for r and i.

3.3 Analysis methods

3.3.1 Optical data

We followed the standard image reduction sequence for mosaic CCDs, namely bias subtraction, flat-fielding by dome and sky flat images, masking bad pixels and removing cross-talk artefacts and cosmic rays. The USNO-A2 catalogue was used to improve the astrometric solution for each field. This solution was also applied to project images so they had the same scale and astrometry using the IRAF tasks GEOMAP and GEOTRAN. Finally, these projected images were combined by using median values, and exposure maps were used as a weight map.

As with the near-IR data, colours of galaxies have to be measured from the same part of each object. Therefore, images for the same field have to be matched to have the same seeing. To do this, the better seeing images were degraded using the PSFMATCH task in IRAF. The DAOPHOT package was used to select unsaturated stars and to create PSF kernels. These kernels were then used to degrade better seeing images to the worst seeing.

In order to detect objects and measure fluxes, the same strategy used for the near-IR data was applied. SExtractor (Bertin & Arnouts 1996) was run in dual mode. The i-band image was used as the detection image. Saturated stars and their haloes were masked in the weight image to remove unreliable objects. Various threshold values were tested, and the value minimising spurious objects was selected. Finally, since the seeing of the CTIO imaging was worse than the DXS, ISO and AUTO magnitude were used to estimate colours instead of aperture magnitude and total magnitude.

Photometric calibration was performed using the Sloan Digital Sky Survey (SDSS, York et al. 2000) catalogue. Aperture colours from SExtractor were calibrated to those of SDSS, and the absolute flux calibration was determined using the total magnitudes in i with respect to those in the SDSS. Finally, we removed unreliable photometric results using a magnitude cut. To remove saturated stars, objects brighter than $i < 17.6$ were replaced by the equivalent SDSS data. In addition, since the number density of objects decreases sharply at $i > 24.6$ and the completeness computed from artificial stars is $\sim$85 per cent at $i = 24.6$, we extracted only objects brighter than $i = 24.6$. A total of 302,402 objects were extracted for the masked 2.45 deg^2 optical catalogue.

3.3.2 Matching optical and near-IR catalogues

To create the final catalogue, optical and near-IR catalogues were combined. Firstly, the near-IR catalogue was matched with the optical catalogue with a 1 arcsec distance, and the average offsets were measured. The offsets were applied to the near-IR catalogue and then the offsets were recalculated. This process was repeated until the average offset was less than 0.1 arcsec. The calculated offsets were 0.05 arcsec
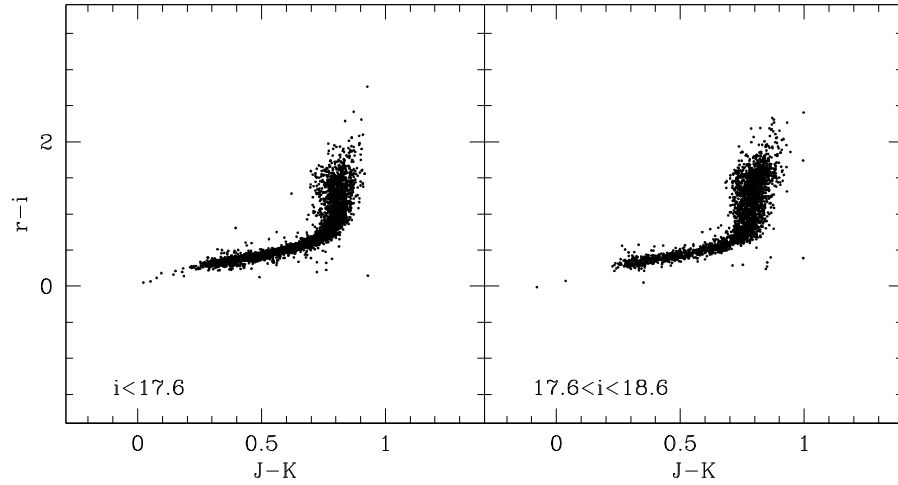
Figure 3.1: The $r - i$ vs. $J - K$ two-colour diagram for point sources of $i < 17.6$ (SDSS source) and $17.6 < i < 18.6$ (CTIO source).

toward the west and 0.43 arcsec toward the north. Finally, the calculated offsets were removed from the near-IR catalogue, and the closest optically detected object within 1 arcsec was taken as the counterpart.

A Galactic extinction correction was applied to all objects. The coordinate of each object was used to measure the reddening value from a dust map (Schlegel, Finkbeiner & Davis 1998). Then the values were transformed into extinction values for each band using the coefficients in Schlegel et al. (1998).

Due to the seeing differences, different aperture magnitudes were used for the optical and near-IR catalogues. To ensure this didn't affect our optical to near-IR colours we compared the two-colour diagram of point sources. The point sources were selected by the magnitude difference measured between $0.4''$ and $2''$ diameter apertures in K. Figure 3.1 shows the two-colour diagram of point sources for $i < 17.6$ (left) and $17.6 < i < 18.6$ (right); there is no significant difference. We also note that there are no appreciable field-to-field variations. Since we combined $i < 17.6$ SDSS sources, figure 3.1 indicates that our colour is not affected by the different methods used to measure fluxes.

The differing depth of the optical and near-IR catalogues may prevent complete selection of red objects. Therefore we tested the fraction of objects detected from both catalogues compared to those detected only in the DXS catalogue. Figure 3.2
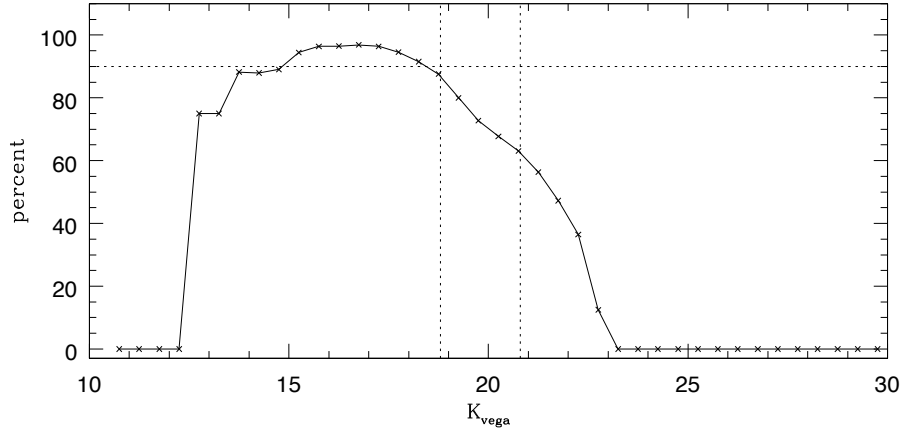
Figure 3.2: The fraction of objects detected from both catalogues compared to those from only the DXS catalogue.

displays the fraction. Dotted lines indicate 90 per cent (horizontal), $K = 18.8$ and $K = 20.8$ (vertical). At bright magnitudes ($K < 15$), saturated stars in i images cause incomplete detection. The objects detected in both catalogues show > 90 per cent completeness at $15 < K < 18.8$ and ~ 60 per cent at $K = 20.8$. This implies that we may miss red objects at a faint magnitude regime due to the depth of optical catalogue. However our bright samples are less affected.

3.3.3   Angular correlation function and correlation length

The angular two-point correlation function is the probability of finding galaxy pairs with respect to a random distribution (Peebles 1980). Usually the estimator from Landy & Szalay (1993) is used to estimate the angular two-point correlation function:

$$\omega_{obs}(\theta) = \frac{DD(\theta) - 2DR(\theta) + RR(\theta)}{RR(\theta)}, \tag{3.1}$$

where DD is the number of observed data pairs with a separation interval $[\theta, \theta + \Delta\theta]$. For this study we used $\Delta log\theta = 0.2$. DR and RR are respectively the mean data-random and random-random pairs in the same interval. All pair counts are normalised to have the same totals.

In order to count DR and RR, we generated the random catalogue with 100 times more random points than the observed data sample. Our random catalogue covered

exactly the same angular mask as our data, including the exclusion of regions around bright stars.

The error on each point in the correlation function was estimated from the poissonian variance of the DD pairs,

$$\delta\omega_{obs}(\theta) = \frac{1 + \omega_{obs}(\theta)}{\sqrt{DD}} \tag{3.2}$$

where DD is the unnormalised value.

The restricted area of our observations leads to a negative offset of the observed angular correlation function which is known as the integral constraint. Therefore, the relation between the real correlation function $(\omega(\theta))$ and the observed correlation function $(\omega_{obs}(\theta))$ is

$$\omega_{obs}(\theta) = \omega(\theta) - \sigma^2, \tag{3.3}$$

where σ^2 is the integral constraint (Groth & Peebles 1977).

If $\omega(\theta)$ is known, the integral constraint can be calculated numerically from the equation in Roche et al. (1999),

$$\sigma^2 = \frac{\sum RR(\theta)\omega(\theta)}{\sum RR(\theta)}. \tag{3.4}$$

In most previous studies, $\omega(\theta) = A_\omega\theta^{-\delta}$ was assumed for the correlation function with a slope fixed at $\delta =0.8$. However, applying a single power law is not appropriate for the correlation function of our samples over the range of angle achieved in this study (see section 3.4). Also even using a double power law can lead to an uncertain integral constraint value if the slope fitted to the larger scales is shallow. This can lead to a greatly inflated integral constraint on scales larger than the sound horizon at recombination ($\sim 100h^{-1}$Mpc) beyond which the angular clustering should be negligible but is predicted to be large. This is particularly important for this study as the largest scales sampled here are comparable to the natural cutoff in clustering that has been demonstrated directly from larger scale surveys by, for example, Maddox et al. (1990) and Sawangwit et al. (2009). To avoid this overestimation of the integral constraint we assume the correlation function has a form of $\omega(\theta) = \alpha_1\theta^{-\beta_1} + \alpha_2\theta^{-\beta_2} - C$, where C is a constant. This functional form provides a good fit to the angular correlation function of AAΩ LRGs in Sawangwit

et al. (2009) as shown in the upper panel of their figure 3.3. With this assumed functional form, we calculated the integral constraints of our samples by an iterative technique with equations 3.1, 3.3, and 3.4. The bottom panel in figure 3.3 shows the example of $K < 18.8$ EROs before and after correcting for the integral constraint (open and filled circles) with the fitted result (solid line). It is also confirmed that the assumed form fits our results well. After correcting for the integral constraint with the assumed form, we used the simple power law, $\omega(\theta) = A_\omega \theta^{-\delta}$, to measure amplitudes and slopes of each sample on small and large scales (see section 3.4 and 3.5 for details).

The observed angular correlation function corresponds to a projection of the real space correlation function, which is assumed to have a power law form.

$$\xi(r) = \left(\frac{r}{r_0}\right)^{-\gamma} \tag{3.5}$$

where $\gamma = 1 + \delta$. The value of r_0, the correlation length, can be calculated by Limber's transformation from the amplitude of angular two-point correlation function (Limber 1953; Peebles 1980). In this study, we used the relation in Kovač et al. (2007). The relation is as follows:

$$A_\omega = r_0^\gamma \sqrt{\pi} \frac{\Gamma(\frac{\gamma-1}{2})}{\Gamma(\frac{\gamma}{2})} \frac{\int_0^\infty F(z) D_A^{1-\gamma}(z) N_{corr}(z)^2 g(z) dz}{\left[\int_0^\infty N_{corr}(z) dz\right]^2} \tag{3.6}$$

where A_ω is the amplitude of angular correlation function, Γ is the gamma function, $D_A(z)$ is angular diameter distance calculated by the Javascript Cosmology Calculator (Wright 2006) and $N_{corr}(z)$ is the redshift distribution of the detected galaxies. Different redshift distributions were used for each sample. In addition, $g(z)$ is given by

$$g(z) = \frac{H_o}{c}\left[(1+z)^2 \sqrt{1 + \Omega_M z + \Omega_\Lambda \left[(1+z)^{-2} - 1\right]}\right] \tag{3.7}$$

for standard cosmological parameters and $F(z)$ is a redshift evolution term. Blanc et al. (2008) point out $F(z) = (1+z)^{-(3+\epsilon)}$, where values of $\epsilon = -1.2$ corresponds to fixed clustering in comoving coordinates, $\epsilon = 0.0$ corresponds to fixed clustering in proper coordinates and and $\epsilon = 0.8$ is the prediction from linear theory, Brainerd, Smail and Mould (1995). In this study, we assume the first case, that the clustering is fixed in
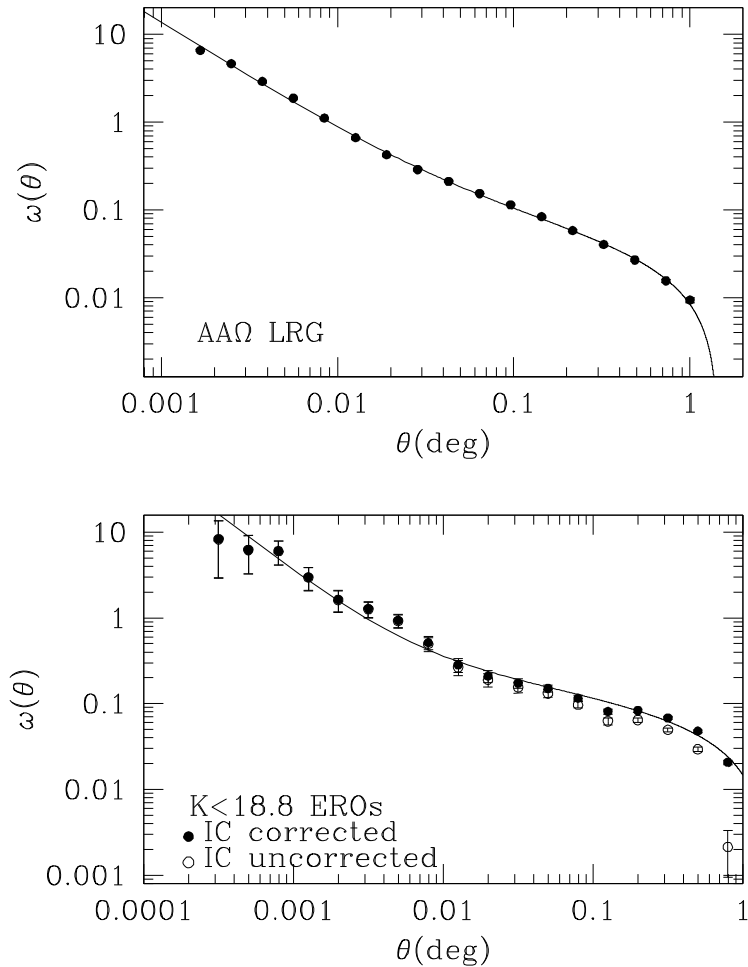
Figure 3.3: Fitted results by the assumed correlation function for AAΩ LRG (top) in Sawangwit et al. (2009) and our $K < 18.8$ EROs (bottom). Open and filled circles in the bottom panel show the correlation function before and after correcting for the integral constraint.

comoving coordinates. In addition, we use a power law slope, δ, determined from $i - K > 4.5$ and $K < 18.8$ EROs to calculate the correlation lengths of various ERO samples.

We generate the redshift distribution for each sample using the photometric redshifts produced by the NEWFIRM Medium Band Survey (NMBS; van Dokkum et al. 2009; Brammer et al. 2009; van Dokkum et al. 2010). This survey images two 0.25 deg^2 areas in the AEGIS (Davis et al. 2007) and COSMOS (Scoville et al. 2007) fields in 5 medium band filters in the wavelength range 1-1.7μm as well as the standard K-band. The addition of these 5 medium band near-IR filters to the already existing deep multi-band optical (CFHTLS) and mid-IR (Spitzer IRAC and MIPS) enables precise photometric redshifts ($\sigma_z/(1 + z) < 0.02$) to be determined for the first time for galaxies at z > 1.4, where the main spectral features are shifted into the near-IR. Although the NMBS can miss the rarest, bright galaxies because of the small surveyed area, NMBS imaging is significantly deeper than the DXS so we are able to directly apply all the same selection criteria that we apply to each sample in this Chapter in order to determine a meaningful redshift distribution. We make use of the full photometric redshift probability distribution functions (PDF) output by the EAZY photometric redshift code (Brammer, van Dokkum & Coppi 2008) that has been used to produce the NMBS photometric redshift catalogue. For each sample, our redshift distribution is defined as the sum of all the PDFs for the galaxies passing the appropriate colour and magnitude selection cuts. The redshift distributions of EROs show different trends with various selection cuts in magnitude and colour. On the one hand, magnitude limited EROs are predominantly at $1 < z < 2$ with a significant peak at $z \sim 1.2$, and a tail to higher redshift that is most apparent for fainter EROs. On the other hand, colour limited EROs show a much broader redshift distribution where the mean increases at higher values of $i - K$. Using the bluest cut of $i - K > 3.96$, a significant population ($> 20\%$) of $z < 1$ objects is included. For DRGs, the brightest ($K < 18.8$) are concentrated at $z \sim 1.1$ and the faintest ($18.8 < K < 19.7$) are more broadly distributed between $1.3 < z < 1.9$. Figure 3.4 displays the redshift distribution of magntiude (left) and colour (right) limited EROs.

Figure 3.4: The redshift distribution of magnitude (left) and colour (right) limited EROs estimated from NMBS.

In order to estimate the uncertainty in the correlation length, a Monte Carlo approach was applied. Firstly 1,000 amplitudes having a normal distribution were generated with the error in amplitude. Then correlation lengths were measured with a fixed redshift distribution for each generated amplitude. Finally, the dispersion of calculated correlation lengths was assigned to be the uncertainty.

3.4 Results

3.4.1 Colour selection and Number Counts

In this study, EROs and DRGs were selected using various colour criteria. Firstly, to remove the large majority of the Galactic stars from the optical-IR catalogue, we used $g - J = 33.33(J - K) - 27$ for $J - K > 0.9$ and $g - J > 3$, and $g - J = 4(J - K) - 0.6$ for $J - K < 0.9$ and $g - J < 3$ introduced by Maddox et al. (2008). A $J - K < 1$ criterion was used for the near-IR catalogue to remove all potential stars. Although many colour criteria for EROs exist, the redshift distribution of EROs in previous studies showed $z \sim 0.8$ as a low redshift limit (Simpson et al. 2006; Conselice et al. 2008). The variation in $i - K$ with redshift predicted from the model galaxy SED in Kong et al. (2009) and the photometric redshift distribution we find from the NMBS indicate that $i - K > 4.5$ is appropriate to select $z > 1$ galaxies.

Therefore, $i - K > 4.5$ was applied to select EROs in keeping with comparable studies but we investigate the impact of varying this cut in section 3.5. Similarly, we use $J - K > 2.3$ to select DRGs. Due to the limitations in the CTIO and DXS imaging our analysis is limited to $i < 24.6$ and $J < 22.0$. So our absolute limit for selecting EROs is $K < 20.0$ and DRGs is $K < 19.7$, well within our completeness in K. Each ERO and DRG requires a joint detection in i and K or J and K respectively, although we do investigate the number of possible EROs and DRGs where no detection is found in the bluer band. Figure 3.5 presents colour-magnitude diagrams for EROs (top) and DRGs (bottom) with selection criteria (lines). In the top panel, horizontal lines are $i - K = 3.96$ (corresponding to $I - K = 4.0$) and $i - K = 4.5$, and the vertical lines are the $K = 18.8$ and 20.0 magnitude limits. In addition, lines in the bottom panel indicate the $J - K = 2.3$ and $K = 18.8$ and 19.7 limits. The open circles are DRG candidates having $J > 22$. Finally, 5,383 EROs and 3,414 DRGs with matched detections were selected.

Figure 3.6 shows the number counts of EROs (top) and DRGs (bottom). The upper lines in each panel are the number counts of all galaxies. In the top panel of figure 3.6, results from the UKIDSS UDS (asterisk, Lane et al. 2007), Deep3a-F (filled triangle) and Daddi-F (filled square) from Kong et al. (2006) and EROs with $R - K > 5.3$ and 6 (open square and triangle) from Simpson et al. (2006) were also plotted for comparison. The number counts of all galaxies in SA22 field are in agreement with previous results. However, all galaxies with matching i and K detections (top) show slightly lower density at faint magnitudes, since our i depth is not sufficient to cover the full near-IR depth. Similarly, our ERO counts are slightly below those from previous results because of our relative depth in i. The filled and open circles indicate EROs in SA22 selected by $i - K > 4.5$ and $i - K > 3.96$, respectively. The filled triangles and squares are the results for EROs selected by $R - K > 5$ from Deep3a-F and Daddi-F of Kong et al. (2006) and, open squares and triangles, $R - K > 5.3$ and $R - K > 6$ EROs from the UKIDSS UDS in Simpson et al. (2006). Our $i - K > 3.96$ ERO counts are comparable to those of $R - K > 5$-5.3 EROs and our $i - K > 4.5$ ERO counts match those of $R - K > 6$ EROs. See section 3.5.4 for a discussion of how the colour selection affects the clustering.
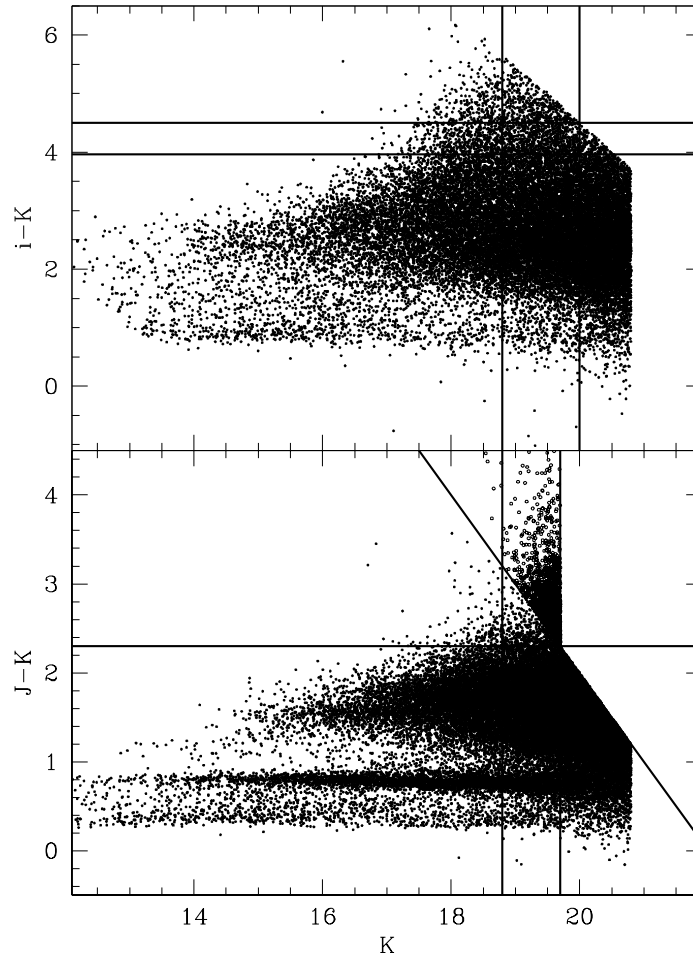
Figure 3.5: The colour-magnitude diagrams for EROs (top) and DRGs (bottom). The lines indicate the selection criteria for each population. For display purpose, only 20 per cent of all detected objects for iK and JK diagrams were displayed. The open circles are DRG candidates having $J > 22$.
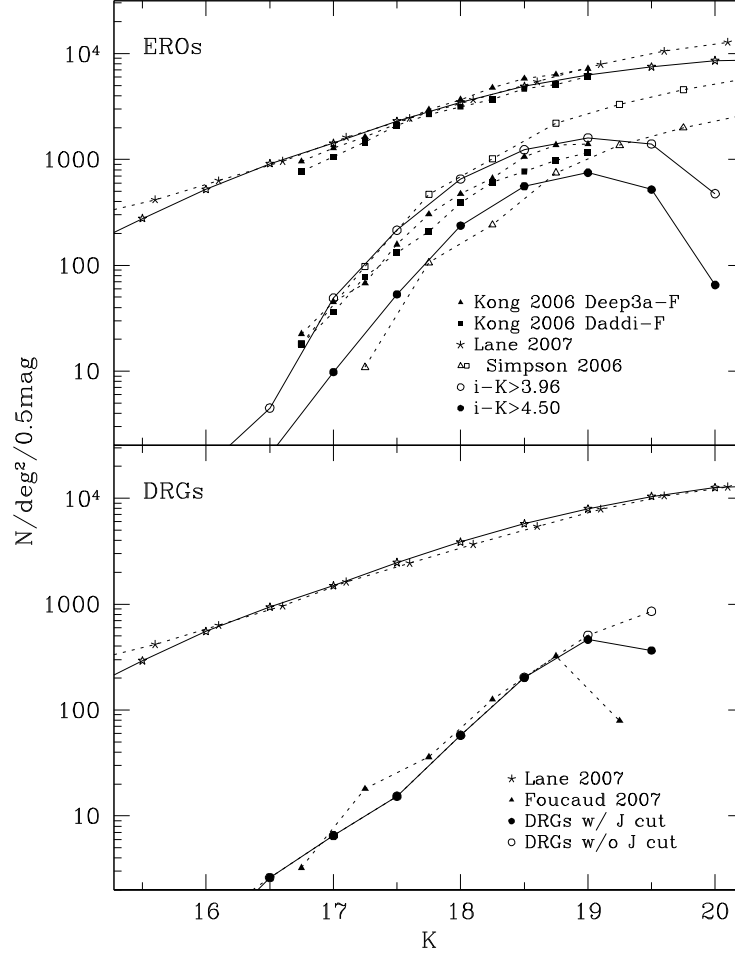
Figure 3.6: Number counts of all galaxies (upper lines in each panel), EROs (top) and DRGs (bottom). The top panel shows the number counts of Deep3a-F (filled triangle) and Daddi-F (filled square) in Kong et al. (2006), $R - K > 5.3$ (open square) and $R - K > 6.0$ (open triangle) EROs in Simpson et al. (2006), all galaxies (asterisk) in Lane et al. (2007) and this work (star). The results of two selection criteria are presented by open circle ($i - K > 3.96$) and filled circle ($i - K > 4.5$) symbols. The bottom panel shows all galaxies (asterisk) in Lane et al. (2007), DRGs (triangle) in Foucaud et al. (2007) and DRGs with a J magnitude cut (black filled circle) and without a J magnitude cut (black open circle), see text for details. Those of all galaxies in this work are results from iK matched (top panel) and only K (bottom panel) samples.

Table 3.1: The number counts in $\log[\mathrm{N}(\deg^{-2} 0.5\mathrm{mag}^{-1})]$ of galaxies $i-K >3.96$ and 4.5 EROs and DRGs. The number counts of all galaxies are measured using only the K magnitude from the UKIDSS DXS catalogue without a J limit, but those for the EROs and DRGs are limited by the i and J depths.

K bin	galaxies	$i-K > 3.96$ EROs	$i-K > 4.5$ EROs	DRGs
15.0	2.165	-	-	-
15.5	2.465	-	-	-
16.0	2.742	-	-	-
16.5	2.973	0.652	0.213	0.416
17.0	3.174	1.690	0.991	0.814
17.5	3.393	2.333	1.725	1.185
18.0	3.586	2.815	2.374	1.761
18.5	3.759	3.092	2.747	2.306
19.0	3.900	3.203	2.875	2.665
19.5	4.017	3.146	2.716	2.561
20.0	4.101	2.678	1.815	-

The bottom panel of figure 3.6 shows the number counts of DRGs. The results for all galaxies with a joint detection of J and K (stars) are in agreement with Lane et al. (2007). In addition, the counts of DRGs are also same as those of the UKIDSS UDS EDR in Foucaud et al. (2007). We also plot the number counts of DRGs irrespective of whether there is a matched detection in J (open circles) which only shows a significant difference for the faintest bin.

Table 3.1 lists the number counts of each population. We note that the number counts of all galaxies are from only the K band of the UKIDSS DXS catalogue without a J limit. However, those for EROs and DRGs are limited by the i and J bands, especially at faint magnitudes.

3.4.2 Clustering of EROs

Figure 3.7 shows the angular two-point correlation function corrected for the integral constraint of all (top), $K < 18.8$ (middle) and $K > 18.8$ (bottom) EROs. Many studies have found EROs are strongly clustered (Roche et al. 2002, 2003; Brown et al. 2005; Kong et al. 2006, 2009). A power law fit to the angular correlation function is consistent with the previous data with no significant differences in the measured
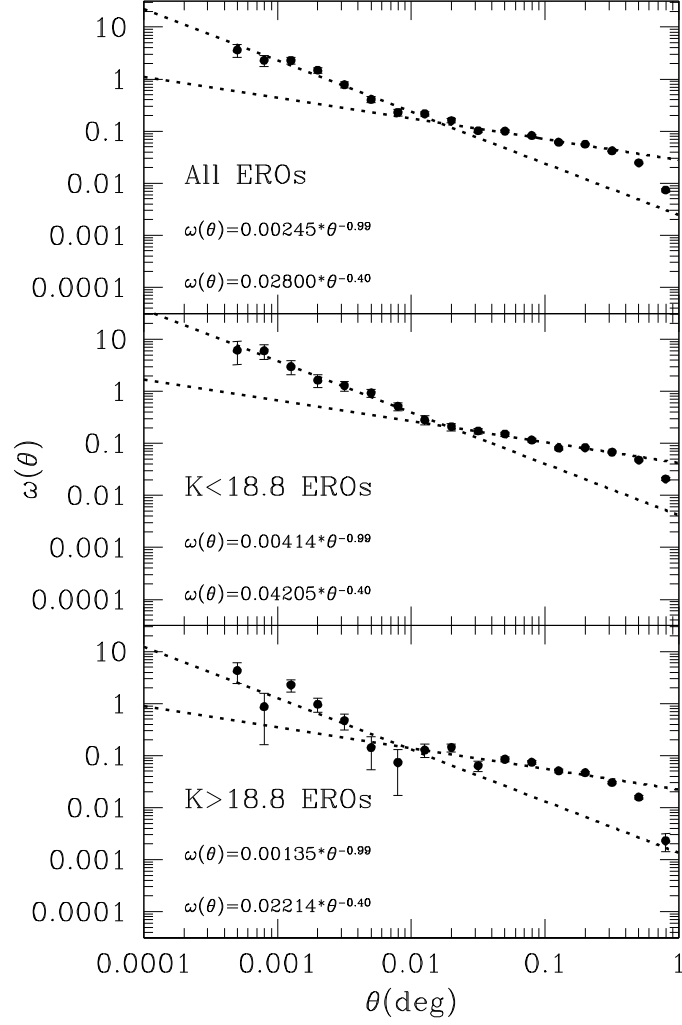
Figure 3.7: The integral constraint corrected angular two-point correlation functions of all (top), $K < 18.8$ (middle) and $K > 18.8$ (bottom) EROs. Dotted lines and equations in each panel show power law $(A_\omega \theta^{-\delta})$ fitting results at small and large scale.

slope. However, all of these studies have been restricted to relatively narrow fields ($< 20'$ on a side) and small samples (< 500). In this study, we present the correlation function of EROs on much wider scales and with a larger sample than before. We confirm that EROs are strongly clustered at all of the angular scales sampled. There is an apparent inflection at $\theta \sim 0.6'$-$1.2'$ implying a double power law is required to fit the correlation function of EROs. This has been observed for LRGs (Ross et al. 2008; Sawangwit et al. 2009) and DRGs at $2 < z < 3$ (Quadri et al. 2008) and is naturally explained by the 1- and 2-halo terms arising in the halo model of galaxy clustering. We fit the correlation function of EROs by separating small ($\theta < 0.76'$) and large ($0.76' < \theta < 19'$) scales, and apply these ranges for all other ERO samples. The slopes of each power law were measured from $K < 18.8$ and $i - K > 4.5$ ERO samples by the fit described in section 3.3.3, and then those were applied to all and $K > 18.8$ EROs, since our i-band magnitude limit prevents a complete extraction of the faint EROs. The measured slopes are 0.99±0.09 for the small scales and 0.40±0.03 for the larger scales. The slopes are slightly smaller than those for LRGs at $z < 1$ (1.16±0.07 and 0.67±0.07 of 2SLAQ and 1.28±0.04 and 0.58±0.09 of AAΩ for small and large scale respectively) in Ross et al. (2008). However, our values are in agreement with DRGs at $2 < z < 3$ (1.2±0.3 and 0.47±0.14 for small and large scale respectively) in Quadri et al. (2008) within the uncertainty ranges. Also bright EROs show a larger amplitude than others, i.e., stronger clustering. The second and third columns in table 3.2 list the amplitudes measured.

Perhaps the most striking result is the very shallow slope of the clustering on the larger scales. The value of 0.4–0.5 is in stark contrast to the canonical value of 0.8 that is so widely found in lower redshift studies and assumed for more distant studies when the slope is poorly constrained. For our ERO and DRG samples, the DRGs in Quadri et al. (2008) and the FIR selected galaxies in Cooray et al. (2010), the strongly clustered objects are being compared in projection over a range of order unity in redshift and all show relatively shallow slopes on scales equivalent to 5–50 h^{-1} Mpc. This contrasts with the equivalent angular clustering of LRGs by Sawangwit et al. (2009) where the depth in redshift is at most 0.2 and the slope is steeper. A similar change in the slope has been noted in faint galaxy

clustering by Neuschaefer & Windhorst (1995) and Postman et al. (1998) in which they parameterised the change in slope as $\delta(z) = 1.75 - 1.8(1+z)^{-0.2-0.35} - 1$, where z is the median redshift of the galaxies sampled. This functional form is consistent with the shallower slope we find for EROs compared to LRGs as long as the index is less than -0.3, although this would predict a much shallower slope at higher redshifts which would appear to be inconsistent with results.

The origin of this change in slope in the angular clustering is a combination several factors. The primary one is the fact that the angular diameter distance at redshifts above 0.8 is relatively constant, although this is strongly dependent on the cosmological parameters as shown by Kauffmann et al. (1999) from N-body simulations. Indeed, the angular clustering as a function of redshift may be a relatively simple test of the Cosmological Constant and has been proposed as a method to detect the Baryon Accoustic Oscillation scale by Sánchez et al. (2011). Another effect that leads to the flattening of the slope may also be the redshift range sampled as the clustering is diluted as galaxies of differing distances are being compared. We note that Sánchez et al. (2011) predict a significantly shallower slope for the angular clustering as the redshift range increases on the scales we are considering here. Future studies will be able to test this directly with improved photometric redshift accuracy.

Our results need to be compared to previous results with careful attention to the differences in our selection and measurement. Thus we applied the same method as the previous studies which measured the integral constraint and the amplitude of correlation function by a single power law with the fixed slope of $\delta = 0.8$. First we consider the amplitude of the clustering which may appear to differ only because of the fact we are fitting a double power law. Fitting a single power law to the angular clustering of $K < 18.8$ and $i - K > 4.5$ EROs we measure an amplitude of $(12.72 \pm 0.5) \times 10^{-3}$ which is consistent with $(14.60 \pm 1.64) \times 10^{-3}$ of Daddi-F EROs at the same magnitude limit, but slightly larger than $(9.29 \pm 1.60) \times 10^{-3}$ of Deep3a-F EROs in Kong et al. (2006). In addition, our value is larger than $(6.6 \pm 1.1) \times 10^{-3}$ of Kong et al. (2009). However, this difference may be the result of the different selection criteria and angular ranges used. To illustrate this, if we fit over the angular

Table 3.2: The amplitudes A_ω of the correlation functions and the number of selected objects in the ERO and DRG samples.

Criterion	EROs			DRGs		
	$A_\omega^{small}(\times 10^{-3})$	$A_\omega^{large}(\times 10^{-3})$	Num	$A_\omega^{small}(\times 10^{-3})$	$A_\omega^{large}(\times 10^{-3})$	Num
All	2.45±0.13	28.00±0.39	5,383	0.19±0.02	7.30±0.44	3,414
$K < 18.8$	4.14±0.33	42.05±0.93	2,277	0.37±0.10	23.63±1.57	979
$K > 18.8$	1.35±0.20	22.14±0.67	3,106	0.16±0.03	6.23±0.67	2,435

range sampled by Kong et al. (2009) of $0.19'$ and $3'$ to measure the amplitude of $i - K > 3.96$ and $K < 18.8$ EROs with a single power law with $\delta = 0.8$ we recover a value of $(6.65\pm0.3)\times10^{-3}$ that does match their published value. Therefore, our results are entirely consistent with Kong et al. (2009) given the effects of Cosmic Variance (see section 3.5.6) even though the slopes and amplitudes we quote appear to differ on first inspection.

Secondly, if a single power law is applied to fit the correlation function, the reduced χ^2 value is 2.8. However, the value drops to 0.3 for small scales and 1.5 for large scales, when the double power law with the measured slopes is applied. Thus a double power law well describes the correlation function of our EROs but past observations have not uncovered it due to their limited angular sampling and larger errors.

The clustering properties as a function of limiting magnitude and colour are discussed in section 3.5.

3.4.3   Clustering of DRGs

Applying a similar analysis to the angular clustering of DRGs, we again find that a double power law fit is required (Figure 3.8). While most early attempts to measure the angular correlation of DRGs were consistent with a single power law (Grazian et al. 2006; Foucaud et al. 2007), Quadri et al. (2008) demonstrated that a double power law with an inflection at $\theta \sim 0.17'$ was appropriate to fit the angular correlation function of $2 < z < 3$ DRGs in the UKIDSS UDS field. However, the angular ranges for the small and large scales used in their fitting were split at $0.67'$. To ensure that our results can be compared, we have used the power law slope for the large scale
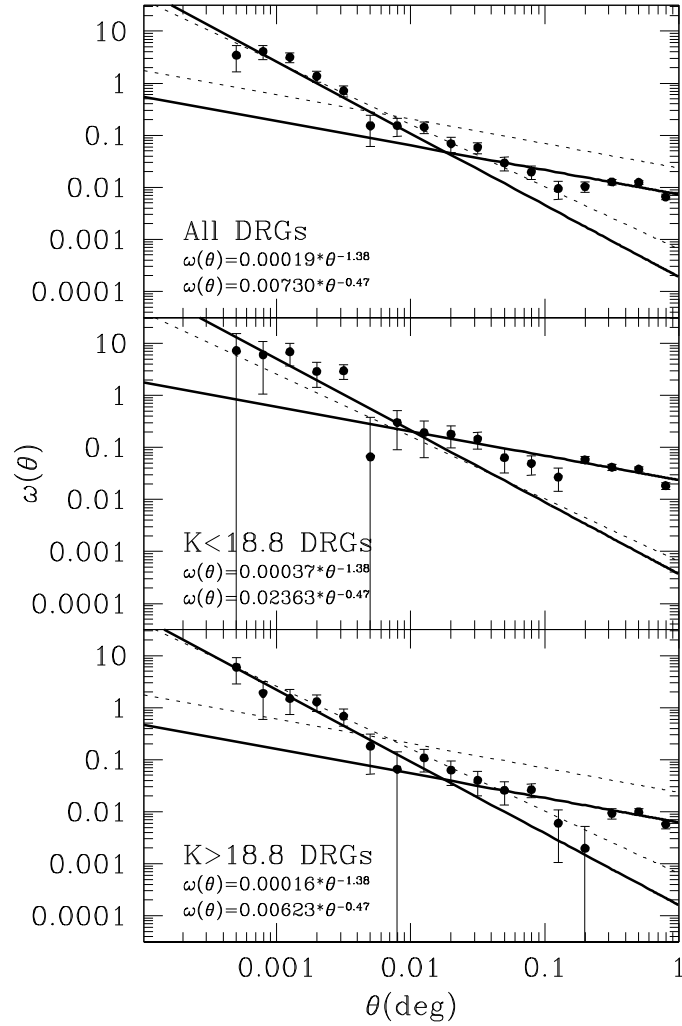
Figure 3.8: The angular two-point correlation functions corrected for the integral constraint of all (top), $K < 18.8$ (middle) and $K > 18.8$ (bottom) DRGs. Solid lines and equations in each panel show power law fitting results. For the comparison we also display the best fit results for $2 < z < 3$ DRGs (dotted lines) from Quadri et al. (2008), although it may not be entirely valid since bright DRGs may be located at $z < 2$.

clustering found by Quadri et al. (2008), $\delta = 0.47$, and measured that for the small scales from a free fit to δ after the integral constraint correction.

In order to measure an amplitude and slope for each angular range, small and large scales were split at $0.48'$ since our correlation functions showed an upturn at $\theta < 0.48'$. Then the power law slope for small scales was measured for $K < 18.8$ DRGs which is not affected by the J magnitude limit. The measured slope was $\delta = 1.38 \pm 0.27$, which is consistent with the value of 1.2 ± 0.3 derived by Quadri et al. (2008) considering the additional photometric redshift constraint they applied.

To directly compare our angular correlation function of DRGs with that in Foucaud et al. (2007), the function for $K < 18.8$ DRGs was fitted with a single power law with a fixed δ of 1.0 between $0.5'$ and $12'$ to match their magnitude limit and fit constraints. The amplitude of $K < 18.8$ DRGs, $(3.07 \pm 0.6) \times 10^{-3}$, is consistent with $3.1^{+2.1}_{-1.3} \times 10^{-3}$ in Foucaud et al. (2007).

Figure 3.8 presents the angular correlation functions corrected for the integral constraint for all (top), $K < 18.8$ (middle) and $18.8 < K < 19.7$ (bottom) DRGs with fitted power laws. The solid and dotted lines are the fitted power law and that for $2 < z < 3$ DRGs in Quadri et al. (2008), respectively. It is apparent that DRGs are strongly clustered, and their correlation functions are well described by a double power law. There are clear differences in the amplitude of clustering on both small and large scales between our brighter and fainter DRGs and in the angular scale for the inflection compared to the Quadri et al. (2008) sample. The measured amplitudes are listed in table 3.2 but should be used with care given the complex interplay between the depth, redshift sampled and angular coverage of DRG samples.

3.5   Discussion

3.5.1   Magnitude limited EROs

It is well known that the clustering of EROs depends on the limiting magnitude of any selection criterion (Daddi et al. 2000; Roche et al. 2002, 2003; Brown et al. 2005; Georgakakis et al. 2005; Kong et al. 2006, 2009). However, in previous cases,

a single power law was invoked to describe the angular correlation function. In this section, we discuss the clustering properties at small and large scales with various magnitude limits to expand on these previous studies.

To select EROs at each magnitude limit, the colour was fixed at $i - K > 4.5$. We applied the same slopes of power law and fitting ranges used in section 3.4.2 for small and large scales, and fitted $\omega(\theta) = A_\omega \theta^{-\delta}$ to the correlation function. Figure 3.9 shows the angular two-point correlation functions corrected for the integral constraint and fitted results for various subsets of EROs using different limiting magnitudes with fixed colour. It is apparent that a double power law is required to fit the correlation function of EROs for all magnitude limits.

The top panel in figure 3.10 shows the amplitude of each power law with fixed slopes as a function of limiting magnitude (filled symbols). Although faint EROs may not be complete because of the relatively shallow i depth, there is a trend in the amplitude at the brightest limiting magnitudes. The amplitude of the small scale varies significantly. However, the amplitude of the large scale shows an almost constant value at all magnitude limits.

The variation in amplitude at small scales is also apparent in the real space correlation length in the middle panel of figure 3.10 (filled symbols). As mentioned in section 3.3.3, the amplitudes measured with fixed slopes from $i - K > 4.5$ and $K < 18.8$ EROs were used to calculate the correlation length. The correlation length for the small scales shows a range between 9 and 14 h^{-1} Mpc with the strongest clustering for the brighter galaxies. On the other hand, the clustering on large scales shows a similar length of 21–24 h^{-1} Mpc that varies marginally over the range in magnitude sampled.

To investigate the variation in slope, we measured slopes by fitting a power law with a free slope. The results are presented in the bottom panel of figure 3.10. The slope of the brighter sub-samples have higher values than the fainter ones, i.e., brighter EROs show steeper correlation functions especially on small scales. The amplitudes and correlation lengths from freely fitted slopes are presented in the top and middle panel of figure 3.10 with open symbols. For display purposes the points are slightly shifted in magnitude. All estimated values with fixed slopes are listed
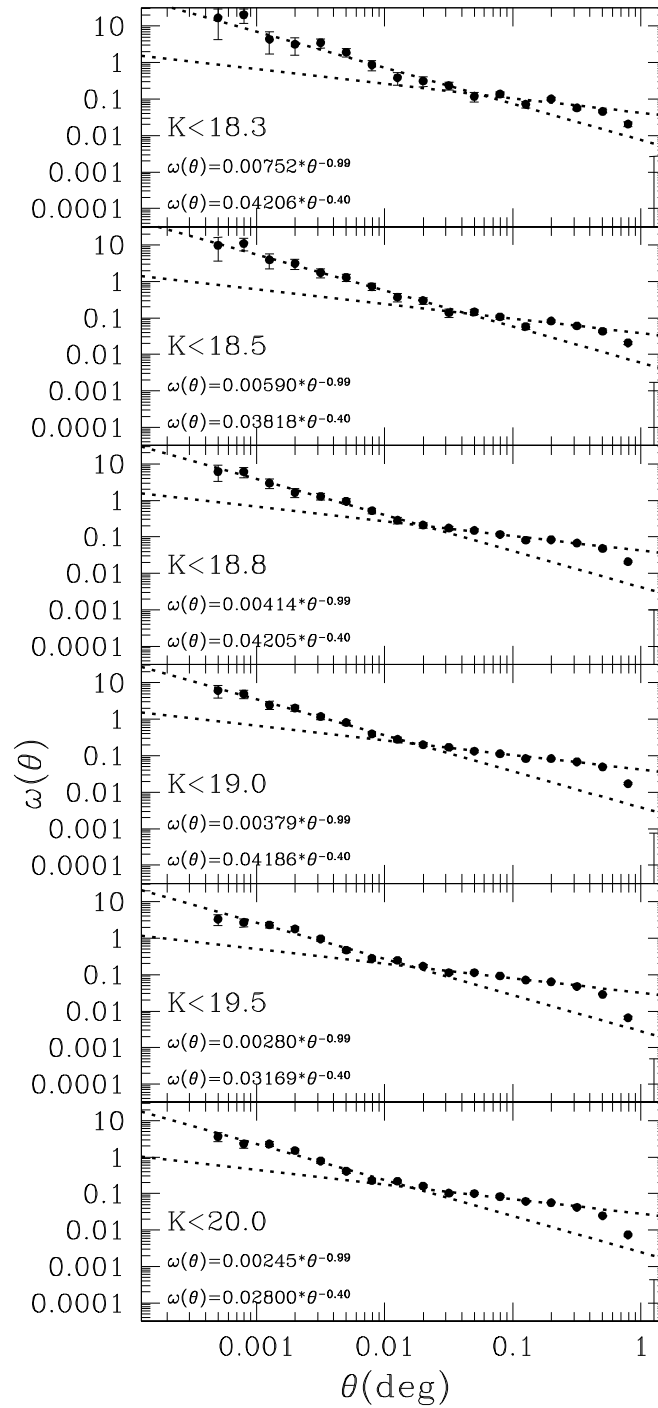
Figure 3.9: The angular two-point correlation functions corrected for the integral constraint and fitted power laws for various magnitude limited samples of EROs.
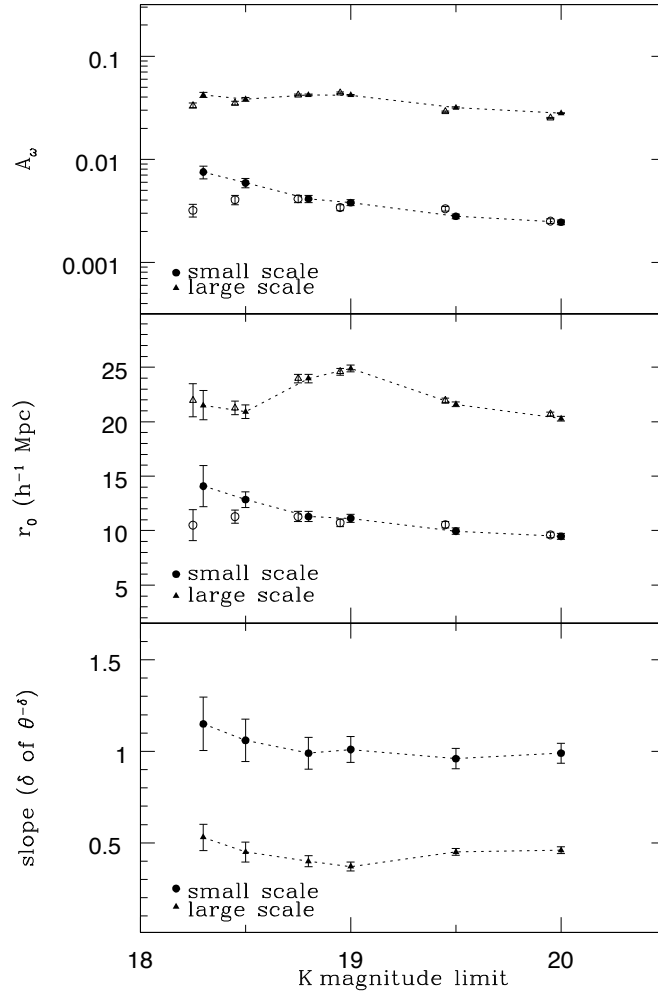
Figure 3.10: The amplitudes (top) and real space correlation lengths (middle) of double power law fits with fixed slopes (δ =0.99,0.40) for magnitude limited EROs and the measured slope (bottom) as a function of limiting magnitude. The open symbols in the top and middle panels are results when the slope is allowed to vary. Those are slightly shifted for display purposes.

Table 3.3: The amplitudes A_ω of the correlation functions, correlation lengths with fixed slopes and number of EROs for each magnitude limit.

K limit	A_ω^{small} ($\times 10^{-3}$)	A_ω^{large} ($\times 10^{-3}$)	r_0^{small} (h^{-1} Mpc)	r_0^{large} (h^{-1} Mpc)	$\chi^2_{small,large}$	Num.
$K < 18.3$	7.52±1.1	42.06±2.5	14.09±1.9	21.51±1.3	0.9, 2.1	852
$K < 18.5$	5.90±0.6	38.18±1.6	12.85±0.7	20.92±0.6	0.3, 2.8	1,323
$K < 18.8$	4.14±0.3	42.05±0.9	11.29±0.5	23.97±0.4	0.3, 1.5	2,277
$K < 19.0$	3.79±0.3	41.86±0.7	11.12±0.4	24.89±0.3	3.2, 2.0	3,014
$K < 19.5$	2.80±0.2	31.69±0.5	9.96±0.3	21.60±0.2	2.0, 3.1	4,713
$K < 20.0$	2.45±0.1	28.00±0.4	9.48±0.3	20.29±0.2	1.9, 3.6	5,383

Table 3.4: The amplitudes A_ω of the correlation functions, correlation lengths with variable slopes and estimated variable slopes of EROs for each magnitude limit.

K limit	A_ω^{small} ($\times 10^{-3}$)	A_ω^{large} ($\times 10^{-3}$)	r_0^{small} (h^{-1} Mpc)	r_0^{large} (h^{-1} Mpc)	slope^{small}	slope^{large}	$\chi^2_{small,large}$
$K < 18.3$	3.20±0.4	33.26±1.9	10.51±1.4	21.97±1.5	1.15±0.15	0.53±0.07	0.7, 1.8
$K < 18.5$	4.05±0.4	34.92±1.5	11.28±0.6	21.27±0.6	1.06±0.12	0.45±0.05	0.2, 2.7
$K < 18.8$	4.14±0.3	42.05±0.9	11.29±0.5	23.97±0.4	0.99±0.09	0.40±0.03	0.3, 1.5
$K < 19.0$	3.40±0.2	44.14±0.8	10.71±0.4	24.59±0.3	1.01±0.07	0.37±0.02	0.4, 1.8
$K < 19.5$	3.31±0.2	28.98±0.4	10.54±0.3	21.94±0.2	0.96±0.06	0.45±0.02	2.0, 2.1
$K < 20.0$	2.45±0.1	25.14±0.4	9.60±0.3	20.70±0.2	0.99±0.05	0.46±0.02	1.9, 2.3

in table 3.3 and those with variable slopes are in table 3.4.

To compare to previous results we again need to fit a single power law to a smaller range in angle. We find the correlation length of $K < 20$ and $i - K > 4.5$ EROs with a fixed $\delta = 0.8$ is 16.99 ± 0.2 h^{-1} Mpc, which is consistent with 12–17 h^{-1} Mpc in Georgakakis et al. (2005). Our value may be higher than Georgakakis et al. due to our redder colour limit that preferentially selects more massive galaxies. Furthermore, the correlation length of our $K < 18.8$ and $i - K > 3.96$ EROs fitted by a single power law (see section 3.4.2) is 12.52 ± 0.33 h^{-1} Mpc which is higher than 9.6 ± 0.1 or 9.2 ± 0.2 h^{-1} Mpc in Kong et al. (2009), although the amplitudes are all consistent. This is most probably caused by the different redshift distribution of the Kong $R - K$ sample. Applying the different criteria to the NMBS sample, our selection has a slightly larger fraction of galaxies at $1.5 < z < 2.0$ than that in Kong et al. (2009).

3.5.2   Colour limited EROs

Daddi et al. (2000) studied the clustering amplitude as a function of colour threshold. They pointed out that red galaxies have a higher amplitude, but the amplitudes of $R - K > 5.0$ and $R - K > 5.3$ EROs were consistent. In addition, Brown et al. (2005) also noted no significant difference in amplitude of $R - K > 5.0$ and 5.5 EROs. However, the small area or shallower depth of previous studies may have prevented a sufficiently accurate measurement of the ERO clustering to recover these differences. In this section we discuss the clustering properties of EROs as a function of colour limit using wider coverage than Daddi et al. (2000) and deeper imaging than Brown et al. (2005).

We used only $K < 18.8$ ERO samples with various colour limits since the i depth is too shallow to cover the full near-IR depth for the reddest sub-samples. Figure 3.11 shows angular correlation functions corrected for the integral constraint for various colour limits and the fitted power laws. The same ranges and fixed slopes from section 3.4.2 were applied to fit the functions. As verified in previous sections, the double power law well describes the functions of all colour limited EROs. However, the correlation functions show different trends from those of magnitude limited
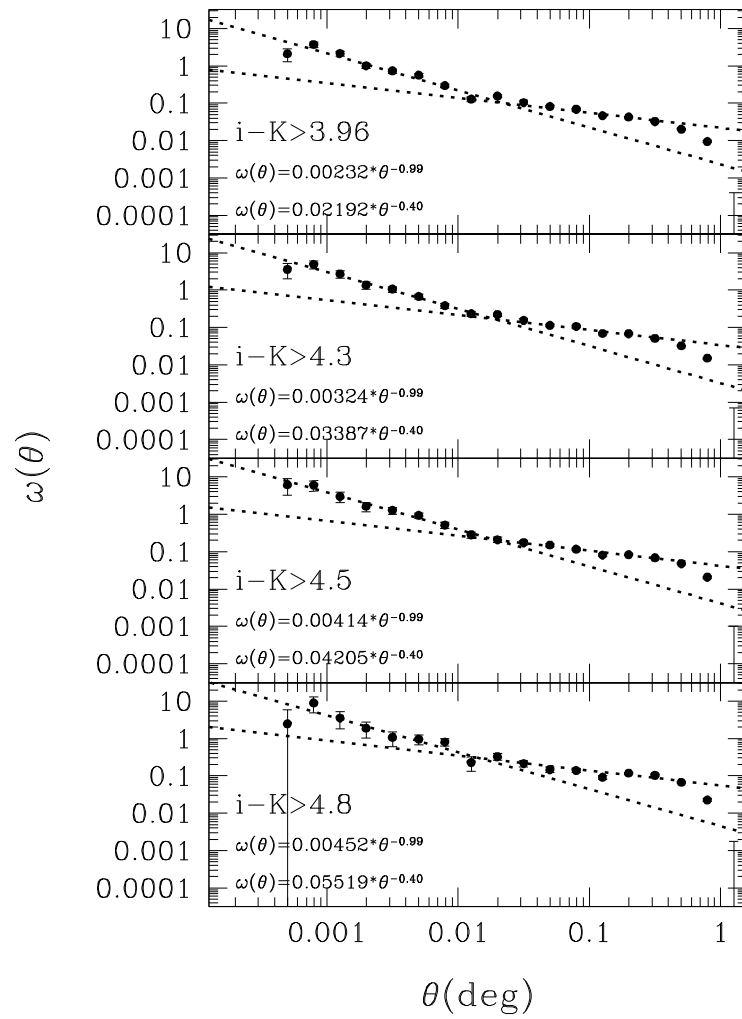
Figure 3.11: The angular two-point correlation functions corrected for the integral constraint and fitted results for various colour limits.
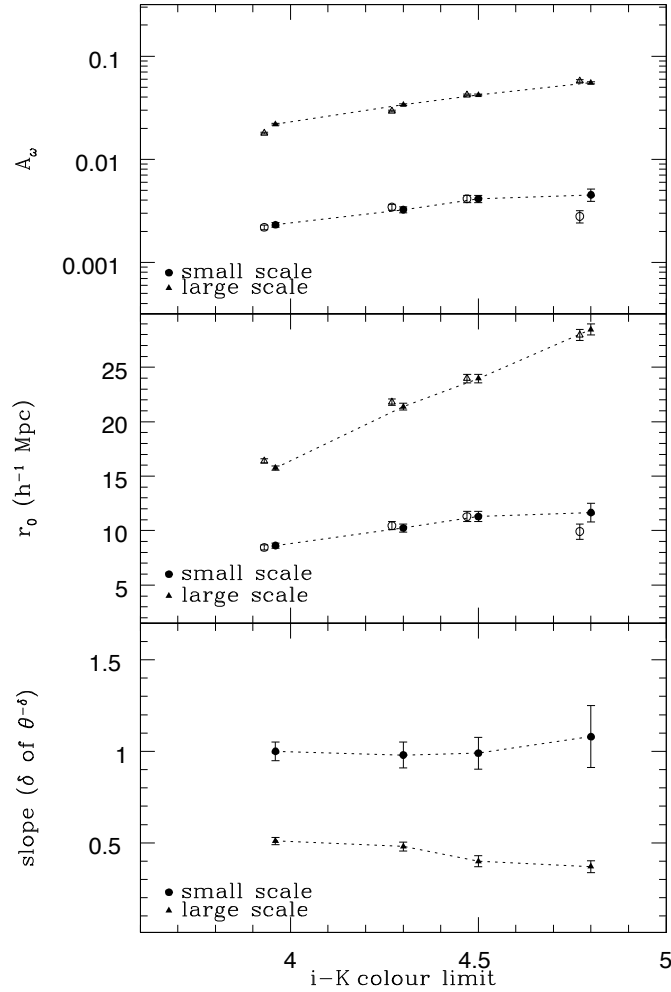
Figure 3.12: The amplitudes (top) and real space correlation lengths (middle) of double power law fits with fixed slopes (δ =0.99,0.40) for colour limited EROs and measured slope (bottom) as a function of colour limits. The open symbols in the top and middle panels are measured from fits with a varying slope. Those are slightly shifted for display purposes.

Table 3.5: The amplitudes A_ω of the correlation functions, the correlation lengths with fixed slopes and the number of EROs for each colour limit.

| $i - K$ limit	A_ω^{small} ($\times 10^{-3}$)	A_ω^{large} ($\times 10^{-3}$)	r_0^{small} (h^{-1} Mpc)	r_0^{large} (h^{-1} Mpc)	$\chi^2_{small,large}$	Num.
$i - K > 3.96$	2.32 ± 0.1	21.92 ± 0.4	8.63 ± 0.2	15.75 ± 0.2	3.2, 5.6	5,654
$i - K > 4.3$	3.24 ± 0.2	33.87 ± 0.6	10.24 ± 0.4	21.39 ± 0.3	0.6, 3.7	3,313
$i - K > 4.5$	4.14 ± 0.3	42.05 ± 0.9	11.29 ± 0.5	23.97 ± 0.4	0.3, 1.5	2,277
$i - K > 4.8$	4.52 ± 0.6	55.19 ± 1.4	11.66 ± 0.9	28.48 ± 0.5	0.8, 5.0	1,259

Table 3.6: The amplitudes A_ω of the correlation functions, the correlation lengths with variable slopes and the estimated slopes of EROs for each colour limit.

$i-K$ limit	A_ω^{small} ($\times 10^{-3}$)	A_ω^{large} ($\times 10^{-3}$)	r_0^{small} (h^{-1} Mpc)	r_0^{large} (h^{-1} Mpc)	slope^{small}	slope^{large}	$\chi^2_{small,large}$
$i-K > 3.96$	2.19±0.1	17.95±0.3	8.46±0.2	16.41±0.2	1.00±0.05	0.51±0.02	3.2, 2.2
$i-K > 4.3$	3.43±0.2	29.32±0.6	10.45±0.4	21.81±0.3	0.98±0.07	0.48±0.02	0.6, 2.3
$i-K > 4.5$	4.14±0.3	42.05±0.9	11.29±0.5	23.97±0.4	0.99±0.09	0.40±0.03	0.3, 1.5
$i-K > 4.8$	2.79±0.4	57.52±1.4	9.92±0.7	27.97±0.5	1.08±0.17	0.37±0.03	0.8, 4.8

EROs. The relation between amplitude and colour limit is presented in the top panel of figure 3.12 (filled symbols). It is clear that redder EROs have higher amplitudes, i.e., stronger clustering. Moreover, there is a similar trend in the amplitude as a function of colour limit for both small and large scales. This is also evident in the trend of the real space correlation length in the middle panel of figure 3.12 (filled symbols), but the correlation lengths for large scales vary most dramatically. This increased clustering with colour limit is entirely as expected given the correlation between colour and lower redshift limit of the selection. The redder colour cuts select more distant, more luminous galaxies that are therefore more clustered. In the bottom panel of figure 3.12, the slopes measured independently show similar values for each scale at all colour limits. The lack of any variation with colour indicates that the form of the clustering does not change dramatically with redshift. The values of the freely fitted slope are also marked as open symbols in the top and middle panels in figure 3.12. The measured values using a fixed slope are listed in table 3.5, and those with a variable slope are in table 3.6.

3.5.3   Populations of EROs

The simple colour selection of EROs, while effective and easy to implement, does not necessarily return a uniform population of galaxies. It is known that EROs can be classified into old passively evolved galaxies (OGs) and dusty star-forming galaxies (DGs). Pozzetti & Mannucci (2000) suggested a colour criterion in the $(I - K)$ versus $(J - K)$ plane defined by differences in the SEDs for old stellar populations and dusty galaxies. However, in this study, the i filter was used instead of I. Therefore we adopted the criterion, $(J - K)=0.20(i - K)+1.08$, defined in the $(i - K)$ versus $(J - K)$ plane by Fang, Kong & Wang (2009). Figure 3.13 shows the two-colour diagram of $K < 18.8$ EROs for classifying OGs and DGs. The line indicates the criterion defined by Fang et al. (2009). The fraction of OGs with $K < 18.8$ and $i - K > 4.5$ is ~63 per cent. This value is consistent with the fractions found for $K < 19.7$ EROs selected by $I - K$ and $R - K$ in Conselice et al. (2008). The fractions of DGs selected by various magnitude cuts with $i - K > 4.5$ are 36 per cent at $K < 18.5$ and 41 per cent at $K < 20$, although this may be affected by
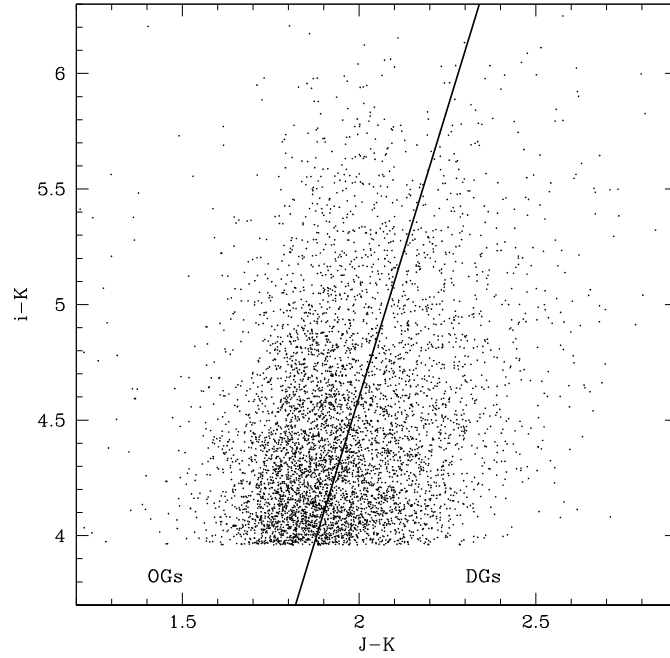
Figure 3.13: The $i - K$ vs. $J - K$ colour-colour diagram for $K < 18.8$ EROs. The line indicates the criterion defined by Fang et al. (2009) to classify OGs and DGs.

the shallow i-band depth. The fraction of colour limited $K < 18.8$ DGs are 43 per cent for $i - K > 3.96$ EROs and 36 per cent for $i - K > 4.8$ EROs.

Figure 3.14 shows the angular correlation functions corrected for the integral constraint of OGs (left) and DGs (right). In addition, correlation functions were measured with various colour (top) and magnitude (bottom) limits. The dotted line of each panel indicates the best fit for the correlation function for $K < 18.8$ and $i - K > 4.5$ EROs. Since the small number of objects for $i - K > 4.8$ DGs can cause a poor statistical error and uncertain integral constraint, $i - K > 4.8$ DGs were excluded for analysis. The most apparent features are that the correlation functions for OGs show a clear break at the same position as that for all EROs in section 3.4.2, and OGs are more clustered than the full ERO sample as a function of both magnitude and colour limit, especially on large scales. Conversely, the correlation functions of DGs show much more scatter between sub-samples in magnitude and colour and are much less clustered than OGs and the full ERO sample. This can be attributed to their wider redshift range and lower intrinsic mass.

These trends are also confirmed in the real space correlation lengths in figure
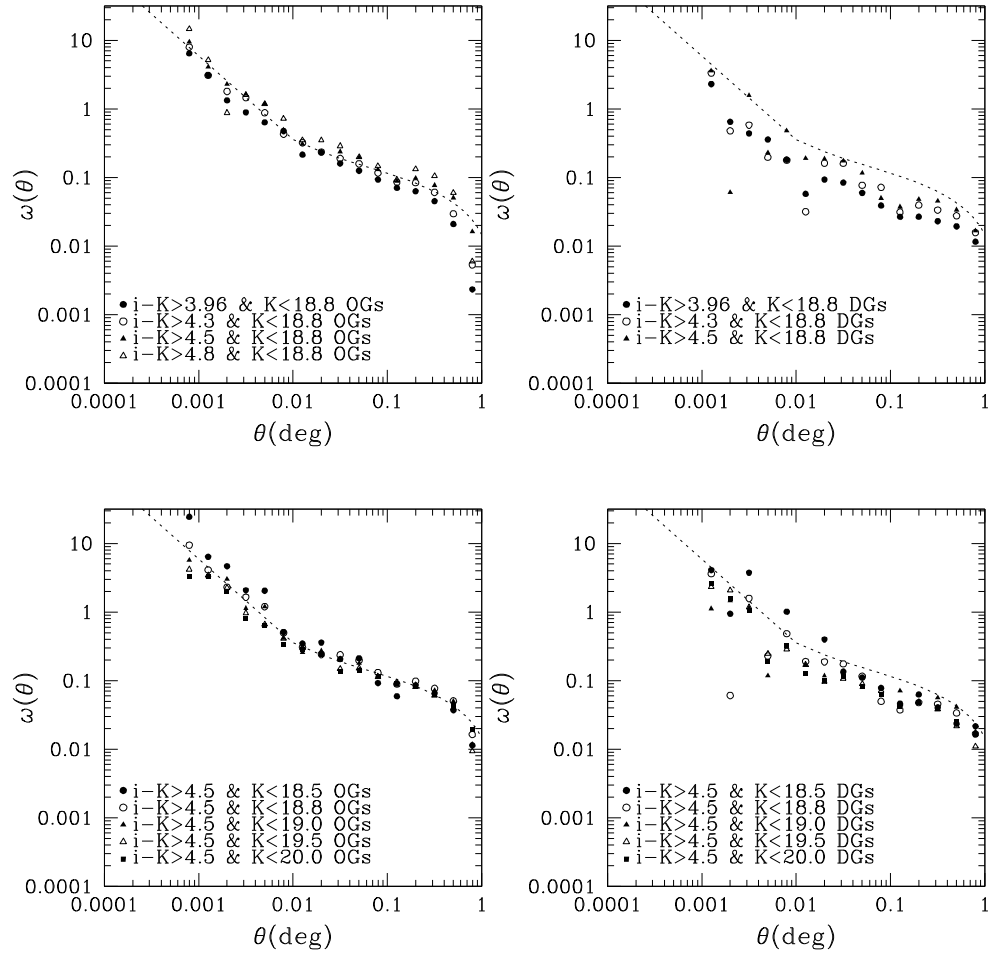
Figure 3.14: The angular correlation functions corrected for the integral constraint of OGs (left) and DGs (right). Also shown are the correlation functions for magnitude limited (bottom) and colour limited (top) samples. The dotted line indicates the best fit for the correlation function of $K < 18.8$ and $i - K > 4.5$ EROs.
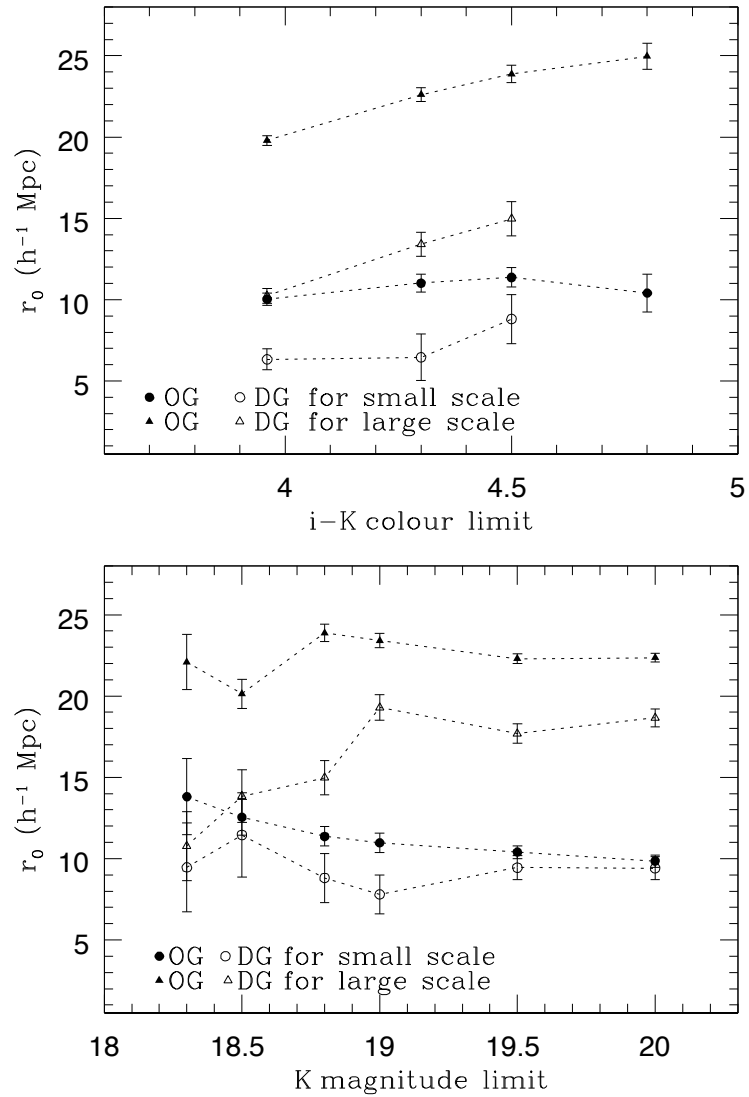
Figure 3.15: The correlation length of OGs (filled symbols) and DGs (open symbols) for various magnitude (bottom) and colour (top) limits.

3.15. Figure 3.15 shows the correlation length of OGs (filled symbols) and DGs (open symbols) on small (circle) and large (triangle) scales plotted for various magnitude (bottom) and colour (top) limits. As the angular correlation function of some DG samples was not measured at $\sim 0.05'$, to estimate the correlation length, the range between $0.076'$ and $0.76'$ for small scales (i.e. narrower than that used earlier), was fitted with the fixed slopes used in section 3.4.2. This may lead to slightly different correlation lengths at small scales, but it should not affect any overall trends. The most important feature of the correlation lengths is the trend within each population. The magnitude limited OGs show no significant change in clustering on large scales and only a weak decline in small scale clustering strength, as the uniformity of the correlation functions in figure 3.14 implies. However redder OGs have larger correlation lengths than bluer ones, since redder OGs are more distant and more massive galaxies. Indeed, the similarity in the clustering in strength and functional form to that of low redshift LRGs in Sawangwit et al. (2009) implies that there is a continuity in the selection of massive, passive galaxies that can be made from optical and near-IR surveys. Similarly, the DGs show more significant variation in clustering with colour and magnitude.

The consistency in clustering within the OG and DG samples contrasts with the much more significant changes in clustering seen in figures 3.10 and 3.12. These trends can be attributed to the changes in the relative proportion of OGs and DGs as a function of colour and magnitude. For instance, the decreased clustering on large scales for the brightest and bluest EROs coincides with the largest fraction of DGs (up to 43 per cent) resulting in lower clustering strength. These results highlight the need to treat the selection of EROs with care as the diversity of galaxies selected can lead to misleading clustering trends.

3.5.4   EROs selected by $r - K$ colour

Although various colour selection criteria have been used in previous studies to select EROs, the differences between criteria have not been well characterised. In this section, we briefly compare the clustering of EROs selected by $r - K$ and $i - K$ colours to attempt to clarify how the use of a different optical filter affects their

statistical and clustering properties.

Figure 3.16 shows the observed angular correlation functions of 5,564 $K < 18.8$ EROs which are selected by $i - K > 3.96$ (filled circle), 4,326 EROs by $r - K > 5$ and $r < 24$ (the peak of our r-band number counts) (open circle), 7,185 EROs by $r - K > 5$ without r magnitude cut (filled triangle) and 4,799 EROs by $r - K > 5.3$ without r magnitude cut (open triangle). It is clear that $r - K > 5.3$ EROs are more clustered than $r - K > 5$ EROs, matching the results found with $i - K$ selection. However, the most apparent feature is that each sample shows different clustering properties, particularly on larger scales. The EROs selected by $i - K > 3.96$ show the highest amplitude of all the samples and the slope of the clustering on larger scales varies significantly with colour. These different clustering properties are most easily explained by the changes in the redshift distribution between samples and the different proportion of OGs to DGs. Conselice et al. (2008) mentioned that the $I - K > 4$ criterion is more useful to select EROs at higher redshift than $R - K > 5.3$. In fact, r-band magnitudes of half of our $i - K > 3.96$ EROs are fainter than our $r = 24$ magnitude limit so any $r - K$ sample would be incomplete. Conversely, 27 per cent of the EROs selected by $r - K > 5$ without an r cut from our sample have $i - K < 3.96$ and would hence not have been considered in any of our $i - K$ samples. These objects $r - K > 5$ EROs that are blue in $i - K$ will be at lower redshifts, lower mass and therefore less clustered.

3.5.5 Clustering of EROs and DRGs

The goal of the colour criteria for EROs and DRGs are to select red galaxies that are likely to be at high redshift ($z > 1$ or $z > 2$). However, Lane et al. (2007) and Quadri et al. (2007) find that the colour cut for DRGs can include a significant fraction of relatively low redshift objects ($0.8 < z < 1.4$) that are dust obscured. In this section we briefly discuss the comparison of two different populations with clustering properties.

Table 3.7 lists correlation lengths of $i - K > 4.5$ EROs and $J - K > 2.3$ DRGs. It is apparent that brighter samples show stronger clustering. Although the direct comparison of correlation length is difficult because of different slopes and redshift
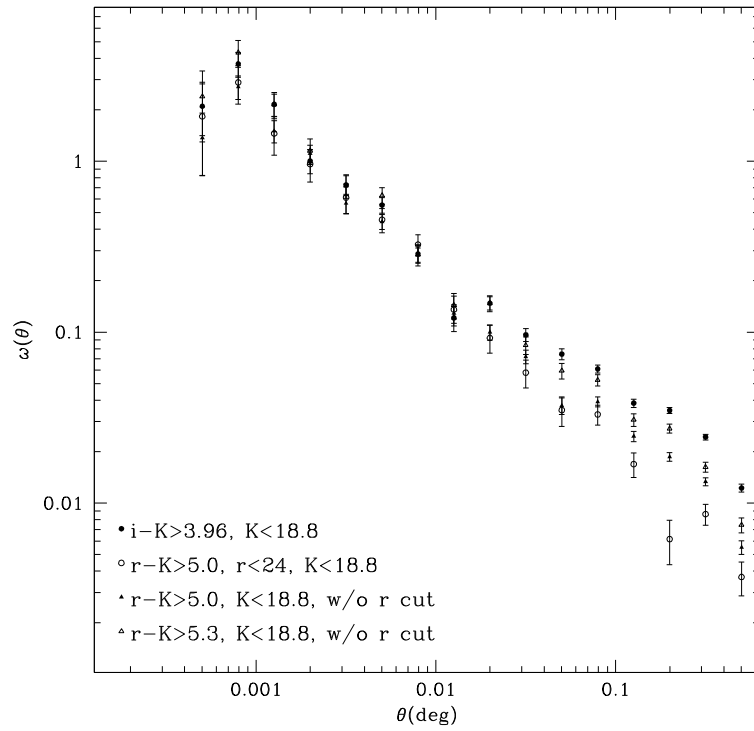
Figure 3.16: The observed angular correlation functions of $K < 18.8$ EROs with $i - K > 3.96$ (filled circle), $r - K > 5$ and $r < 24$ (open circle), $r - K > 5$ without an r cut (filled triangle) and $r - K > 5.3$ without an r cut (open triangle). It is noted that an integral constraint correction has not been applied to these functions.

Table 3.7: The correlation length r_0 (h^{-1} Mpc) of selected objects for EROs and DRGs.

Criterion	$r_{0,ERO}^{small}$	$r_{0,ERO}^{large}$	$r_{0,DRG}^{small}$	$r_{0,DRG}^{large}$
All	9.48 ± 0.3	20.29 ± 0.2	4.66 ± 0.2	10.32 ± 0.4
$K < 18.8$	11.29 ± 0.5	23.97 ± 0.4	5.14 ± 0.6	17.19 ± 0.8
$K > 18.8$	7.12 ± 0.6	17.45 ± 0.4	4.42 ± 0.4	9.52 ± 0.7

distributions, we can confirm that EROs are more clustered than DRGs from the comparison of figure 3.7 and 3.8, and correlation lengths. This was also found by Foucaud et al. (2007).

However, it has been shown that the $J - K > 2.3$ criterion selects $1 < z < 2$ objects as well as ones at $z > 2$ (Grazian et al. 2006; Papovich et al. 2006; Conselice et al. 2007; Lane et al. 2007). Quadri et al. (2007) also pointed out that the fraction of $z < 1.8$ DRGs is 15 per cent at $K < 21$ and 50 per cent at $K < 19$. Therefore, from the different clustering properties of the two populations, we can contrast them at $1 < z < 2$ where most bright DRGs and $i - K > 4.5$ EROs are located. The different clustering properties in the bin indicate that EROs and DRGs may have different characteristics. In fact, Conselice et al. (2007) demonstrated that $1 < z < 2$ DRGs show a broad range in stellar mass and that EROs are more massive than DRGs at the same redshift (Conselice et al. 2008). These mass differences can explain the stronger clustering of EROs compared to bright DRGs, since massive objects are expected to be more clustered. Furthermore, contamination from low redshift DRGs may lead to the variation of clustering between our samples and $2 < z < 3$ DRGs seen in figure 3.8. The fraction of $z < 1.6$ DRGs at $K > 18.8$ magnitude range is $\sim$40 per cent in NMBS redshift distribution. This effect is also verified by the weaker clustering of $r - K$ EROs in the previous section. This means that when using a simple colour criterion it is difficult to avoid a contribution from different types of galaxy or galaxies over a wide range in redshift.

Our correlation lengths of DRGs are apparently different from previous results. If a single power law is applied for our $K < 18.8$ DRGs, the correlation length is 9.5 ± 1.0 h^{-1} Mpc. This value is smaller than $14.1^{+4.8}_{-2.9}$ h^{-1} Mpc with $\sigma = 0.5$ redshift distribution or $11.1^{+3.8}_{-2.3}$ h^{-1} Mpc using a Gaussian redshift distribution with $z = 1$

and $\sigma = 0.25$ in Foucaud et al. (2007) but is within the error range of both of these estimates. These apparent differences may be caused by differences in the redshift distribution. The NMBS redshift distribution is broader and more complicated than that assumed in Foucaud et al. and is likely to better reflect the true DRG redshift distribution. Quadri et al. (2008) measured $r_0 = 10.6 \pm 1.6 \ h^{-1}$ Mpc on large scales for $2 < z < 3$ DRGs. This is consistent with our results for faint DRGs, but smaller than for our brighter DRGs. The improvement in photometric redshift measurement for galaxies at $z > 1$ that the NMBS provides is considerable. Future broad band studies will benefit from the NMBS constraints on redshift distributions.

3.5.6 Cosmic variance

Cosmic variance is an important source of systematic error in the investigation of the high redshift universe (Somerville et al. 2004). In particular, it is a significant contribution to the uncertainty in galaxy number counts and luminosity function (Somerville et al. 2004; Trenti & Stiavelli 2008). Somerville et al. (2004) defined the relative cosmic variance with mean and variance of number counts.

$$\sigma_v^2 \equiv \frac{\langle N^2 \rangle - \langle N \rangle^2}{\langle N \rangle^2} - \frac{1}{\langle N \rangle} \tag{3.8}$$

The last term gives the correction for Poisson shot noise. Garilli et al. (2008) compared cosmic variances defined by the above equation and correlation functions from the VIMOS VLT Deep Survey (VVDS) data, and argued that the values were in agreement. Therefore, we simply used the above equation to estimate the cosmic variance.

We divided the SA22 field into 9 sub-fields using two criteria, CTIO Blanco field of view (~ 0.36 deg^2) and WFCAM field of view (~ 0.8 deg^2), with $i - K > 4.5$ and $K < 18.8$ EROs. However the actual masked average areas were ~ 0.27 deg^2 and ~ 0.63 deg^2 for Blanco and WFCAM size fields, respectively. The number density of EROs in each field was calculated and used in equation 3.8. We note that the field-to-field ratios of number density were consistent with those for various brighter magnitude limits. Therefore, the field-to-field variation at this magnitude range is not a systematic effect, unlike a change in the limiting magnitude or area. The
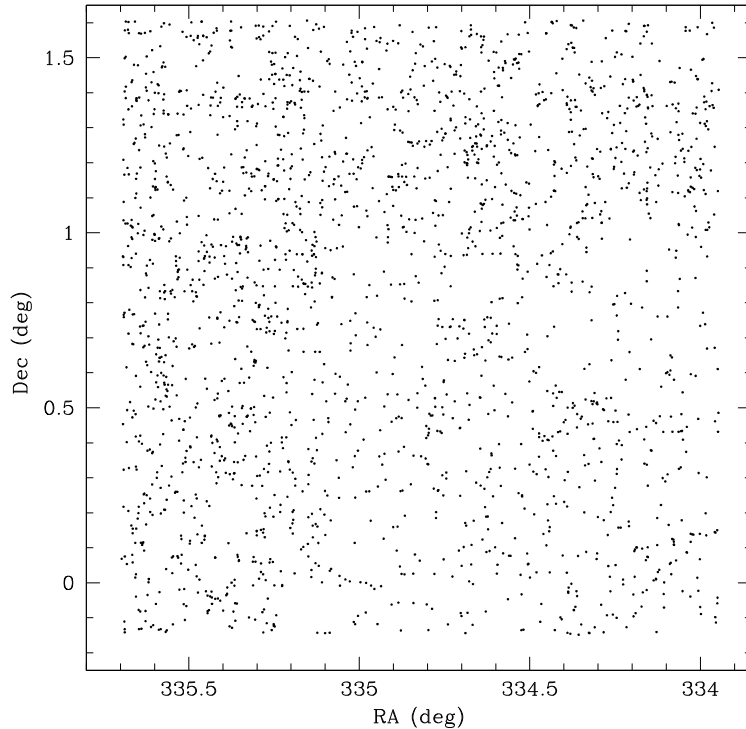
Figure 3.17: The spatial distribution of $K < 18.8$ and $i - K > 4.5$ EROs.

measured cosmic variances were 0.30 and 0.20 for Blanco and WFCAM field size, respectively.

In fact, it is known that the spatial distribution of EROs is inhomogeneous (Daddi et al. 2000; Kong et al. 2006), at least in part due to the strong clustering that EROs exhibit. Figure 3.17 shows the spatial distribution of $i - K > 4.5$ and $K < 18.8$ EROs. As checked by the number density variation of each sub-field and figure 3.17, the distribution of our EROs is also inhomogeneous. There are some overdense regions in the northern part of the field. Moreover, figure 3.18 shows the angular correlation functions corrected for the integral constraint of $i - K > 4.5$ and $K < 18.8$ EROs in each sub-field by Blanco size (top) and WFCAM size (bottom). The solid lines indicate the best fit of the correlation function for $i - K > 4.5$ and $K < 18.8$ EROs in the whole field. It appears that the correlation functions show the most variation on Blanco field size scales. In particular, the standard deviations of the amplitudes of angular correlation function on large scales are 0.011 and 0.007 for CTIO and WFCAM size sub-fields, respectively. Also, the standard deviations of the correlation lengths are 4.5 and 2.8 h^{-1} Mpc respectively. These
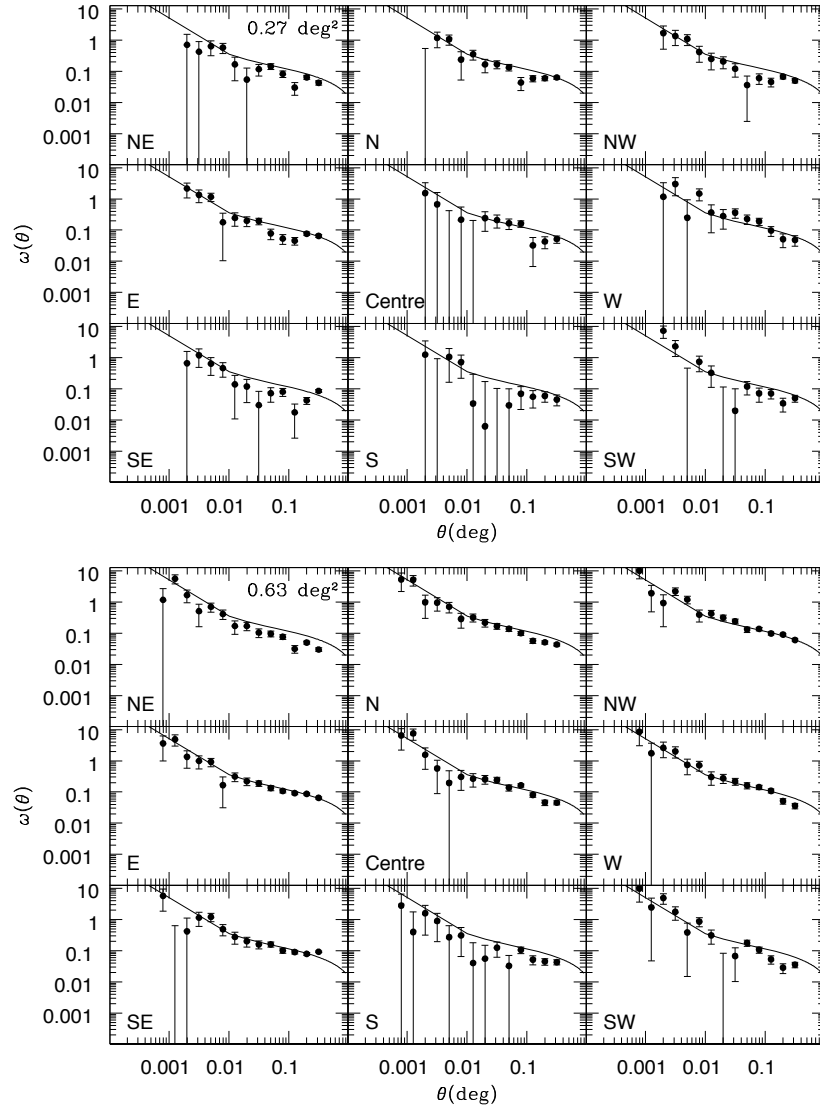
Figure 3.18: The angular correlation functions corrected for the integral constraint of EROs for 0.27 deg^2 (top) and 0.63 deg^2 (bottom) fields at each position. The solid lines indicate the best fit of $K < 18.8$ and $i - K > 4.5$ EROs in the whole field.

results demonstrate that cosmic variance for these field sizes can significantly affect the uncertainty of the measured clustering strength and is likely to have been the dominant source of error in previous clustering analyses of high redshift galaxies. It is apparent that a large-area survey is important not only to confidently measure number counts but also to investigate clustering properties.

3.6 Conclusions

We have used near-IR images from UKIDSS DXS DR5 and gri optical images from CTIO 4m Blanco telescope to investigate the clustering properties of EROs and DRGs in $\sim$ 3.3 deg^2 SA22 field. This is the largest area survey of such galaxies to date, and using the precise redshift distributions from the NMBS we have made the most accurate measurements of the cluster of EROs and DRGs. The results are summarised as follows;

1. Colour selection criteria were applied to extract EROs and DRGs. In total 5,383 EROs with $i-K > 4.5$, $i < 24.6$ and $K < 20.0$ were selected. In addition, 3,414 DRGs were extracted by a $J-K > 2.3$ with $J < 22$ and $K < 19.7$ limits. The number density of EROs was well matched to previous studies once the differences in selection method were taken into account. Similarly, the number density of DRGs was very well matched with the results from the UKIDSS UDS field.

2. Both populations showed strong clustering properties. Those of EROs are best described by a double power law with inflection at $\sim$ 0.6′-1.2′. Assuming a power law, $\omega(\theta) = A_\omega \theta^{-\delta}$, (A_ω, δ) of $K < 18.8$ and $i - K > 4.5$ EROs were (0.00414, 0.99) and (0.04205, 0.40) for small and large scales respectively.

3. Additionally a double power law is required to fit the angular correlation function of DRGs with δ =1.38 and 0.47 for small and large scale respectively. Our relatively bright magnitude limit samples are diluted by $1 < z < 2$ DRGs, so our clustering shows different trends when compared to deeper samples dominated by $2 < z < 3$ DRGs.

4. The angular two-point correlation function of EROs shows clear trends with different magnitude limits, although those for faint samples may be dominated by relatively blue EROs due to the optical limit. With a fixed power law slope, the amplitude for small scales decreased at fainter magnitudes, but that for large scales was invariable with magnitude. These trends were also confirmed by the real space correlation length. On the other hand, with variable slopes, the correlation function at bright limits is steeper than for samples with fainter limits.

5. The colour limited correlation function of EROs presents slightly different features from the magnitude limited function. With a fixed slope, clustering amplitudes and real space correlation lengths for small and large scales were increased with redder colours. However, slopes were comparable between various colour cuts.

6. The EROs were classified into OGs and DGs by their $i - K$ vs. $J - K$ colours. The correlation functions of magnitude limited OGs show an apparent break at $0.6'$-$1.2'$ and similar amplitude at large scales. The redder ones have stronger clustering. However, the functions for DGs, showed much weaker clustering. The relative proportion of OGs and DGs with colour and magnitude can explain the different trends seen in the clustering of the full sample of EROs.

7. EROs selected either with $r - K$ or $i - K$ colours show different correlation functions, especially on large scales. The EROs selected by $i - K > 3.96$ are more clustered than those by the $r - K$ selection criteria. This may be caused by the different redshift distribution, since the $r - K$ criterion extracts more low redshift galaxies than the $i - K$ criterion.

8. EROs are more clustered than DRGs over the same redshift range $(1 < z < 2)$. This is evidence that the two populations at this redshift are different and EROs are likely to be intrinsically more massive than DRGs.

9. By dividing the full survey field in to sub-fields of different sizes we demonstrate that cosmic variance is a significant issue for measurements of correlation

function and is likely to have been the dominant source of error in previous measurements of high redshift red galaxy clustering.

The results from this analysis illustrate the importance of sampling the widest possible fields in the near-infrared in order to recover representative clustering properties of distant galaxies. In the near future the combination of UKIDSS and VISTA surveys will cover more than an order of magnitude larger area to comparable depth. Our ability to extract the clustering of EROs in these areas is limited only by the depth of comparable optical imaging.

Finally, ERO samples are now of sufficient size to offer direct tests to galaxy formation models in terms of number density *and* clustering so future comparisons to semi-analytic simulations will be more powerful (Gonzalez-Perez et al. 2011 and Chapter 5).

Chapter 4

Clustering of EROs in the Elais-N1

4.1 Introduction

Extremely Red Objects (EROs, Elston, Rieke & Rieke 1988) can be selected on the basis of their red optical/near-IR colour ($(I - K)_{vega} > 4$). This is efficient in detecting massive galaxies ($> 10^{11} M_{\odot}$) at $z > 1$ (Conselice et al. 2008). Moreover it is known that EROs are strongly clustered (Daddi et al. 2000; Roche et al. 2002, 2003; Brown et al. 2005; Kong et al. 2006, 2009) and reside in massive dark matter haloes (Moustakas & Somerville 2002; Gonzalez-Perez et al. 2009). However EROs selected with a simple colour cut are contaminated by dusty, star-forming galaxies (Pozzetti & Mannucci 2000; Smail et al. 2002; Roche et al. 2002; Cimatti et al. 2002, 2003; Moustakas et al. 2004; Sawicki et al. 2005; Simpson et al. 2006; Conselice et al. 2008; Kong et al. 2009).

In this Chapter, we use near-IR images of a wide contiguous field from the 7th and 8th Data Release (DR7 & DR8) of the Deep eXtragalactic Survey (DXS), a sub-survey of UKIDSS. Other optical datasets such as the Subaru I-band catalogue and the Panoramic Survey Telescope and Rapid Response System (Pan-STARRS) are also merged. From the merged optical to near-IR catalogue, the angular clustering of EROs selected with various criteria is measured and discussed.

Unless otherwise noted, the photometry is quoted in the AB scale in this Chapter.

We assume the following cosmology : $\Omega_m = 0.27$, $\Omega_\Lambda = 0.73$, $\sigma_8 = 0.8$ and $H_o = 100$ h km s^{-1} Mpc^{-1} with $h = 0.73$.

4.2 Data

4.2.1 UKIDSS

In this study we deal with the Elais-N1 field centred on $\alpha = 16^h\ 10^m\ 00.0^s$, $\delta = +54^d\ 00^m\ 00.0^s$ (J2000). The datasets from data release 7 and 8 were used for this work. The survey for this field is on-going so that K-band data cover the whole region but J-band exists for only $\sim$56 per cent. The typical seeing is $\sim 0.9''$ at J and $\sim 0.8''$ at K. Although K-band dataset has mapped 6.5 deg^2 after masking unreliable regions, the actual area for this work depends on optical datasets (see next subsection). We found 670,214 objects based on K-band images.

4.2.2 Other datasets

Pan-STARRS

The Panoramic Survey Telescope and Rapid Response System (Pan-STARRS, Kaiser & Pan-STARRS team 2002) is a large optical survey scanning whole sky visible from Hawaii. The science objectives are various, from the Solar system astronomy to the distant Universe. The Pan-STARRS prototype telescope (PS1) is a 3-year science mission performed by the PS1 Science Consortium[1]. The 1.8m PS1 telescope feeds a 1.4 gigapixel camera covering a 3.2 diameter degree field of view with $grizy$ filters.

We used the Medium Deep Survey (MDS) data which comprises ten separate fields. The limiting magnitude was found to be $i_{AB} \sim 25.0$ by matching sources with the deeper Subaru catalogue. The PS1 catalogue was merged with the DXS near-IR catalogue (DXS/PS1). In order to calculate the colour of matched objects, a 3-arcsec aperture magnitude from PS1 was used, since the typical seeing of PS1 MDS was $\sim 1.2''$ which was worse than $\sim 0.8''$ for DXS. The area covered by the

---

[1] http://ps1sc.org/

DXS/PS1 combination is 5.33 deg^2. The Galactic extinction was corrected using the dust map in Schlegel, Finkbeiner & Davis (1998)

Subaru

To complement the UKIDSS DXS dataset, an I-band catalogue was also merged (DXS/Subaru). This was obtained with the Suprime-Cam mounted on the Subaru telescope. It covers part of the DXS Elais-N1 field. The 5σ point-source limit is $I_{AB} = 26.2$ (Sato et al., in preparation). However we cut samples at $I_{AB} = 25.5$, because there are field to field variations in depth. We find a consistent galaxy number density at brighter than $I_{AB} = 25.5$ across the observed area. For colour calculations a 2-arcsec aperture magnitude was used since the seeing of the Subaru data is similar to that of the UKIDSS DXS. The area covered by DXS/Subaru is 3.88 deg^2. As for DXS/PS1, the Galactic extinction was also corrected using the dust map in Schlegel et al. (1998).

SWIRE

The Elais-N1 field was also mapped by the Spitzer Wide-area InfraRed Extragalactic (SWIRE) survey (Lonsdale et al. 2003). SWIRE imaged 49 deg^2 mapping 6 fields at mid-IR wavelengths. In this work IRAC band data from DR2 (Surace et al. 2005) were merged with the other datasets. However, only the 3.6 and 4.5 μm catalogues were used to measure photometric redshift with the DXS/PS1 dataset.

4.2.3   ERO selection

In this study EROs were selected through $i - K$ colour for DXS/PS1 and $I - K$ colour for the DXS/Subaru. The majority of the Galactic stars were removed to avoid contamination. In the case of DXS/PS1 various schemes were applied. Firstly bright stars were removed using the magnitude difference between K-band aperture and total magnitudes. Then stellar sequences in $(i - K)$ vs. $(g - i)$ and $(r - [3.6])$ vs. $(r - i)$ colour-colour diagrams were extracted. These criteria are $(i - K)_{AB} = 0.76(g-i)_{AB}-0.85$ and $(r-[3.6])_{AB} = 2.29(r-i)_{AB}-0.66$. On the other hand, stars in DXS/Subaru were selected by comparing with those in DXS/PS1. Possibly faint

stars in the DXS/Subaru were not removed, but this does not affect our analysis because of the red colours of EROs.

From the catalogues with Galactic stars removed, colour criteria were applied to select EROs. For DXS/PS1 $(i - K)_{AB} > 2.45, 2.95$, $i_{AB} < 25$ and $K_{AB} < 22.7$ $((i - K)_{vega} > 4, 4.5$ and $K_{vega} < 20.8)$ were applied to satisfy the classical colour cut for EROs and limit magnitudes. Also $(I - K)_{AB} > 2.55, 3.05$, $I_{AB} < 25.5$ and $K_{AB} < 22.7$ were used for the DXS/Subaru dataset. The colour difference between the two catalogues came from different filters. Finally we detected 17,250 and 5,039 EROs with $(i - K)_{AB} > 2.45$ and $(i - K)_{AB} > 2.95$ from DXS/PS1 respectively. In addition from DXS/Subaru, 23,916 and 7,959 EROs were selected for these bluer and redder cuts respectively.

Figure 4.1 shows the number counts of all galaxies (top lines) and EROs (bottom lines). The solid line indicates number counts of galaxies, and the dashed lines are for EROs with bluer and redder cuts from this work. The number counts of galaxies in Lane et al. (2007, open stars) and Kong et al. (2006, open squares and triangles) and EROs in Kong et al. (2006, filled squares and triangles) are also displayed. The counts from this work are consistent with previous studies. However the result from the DXS/PS1 samples shows lower values than that from the DXS/Subaru samples at the faint magnitude regime because of the different depth of these optical datasets.

4.2.4   Photometric redshift

The main purpose of Chapters 4 and 5 is to compare the properties of haloes hosting EROs at different redshifts as well as to measure their angular clustering. For this purpose the photometric redshifts of EROs were measured using $grizJK3.6$ and 4.5 photometric data from DXS-PS1-SWIRE. The Easy and Accurate Z from Yale (EAZY) code (Brammer, van Dokkum & Coppi 2008) was run to measure photometric redshifts of all objects. The default parameters of the EAZY code were used, and as a training set we used spectroscopic redshift datasets from Rowan-Robinson et al. (2008), which contained those in Berta et al. (2007) and Trichas et al. (2010). The normalised median absolute deviation (NMAD) in $\Delta z/(1 + z_{spec})$ was ~ 0.066.
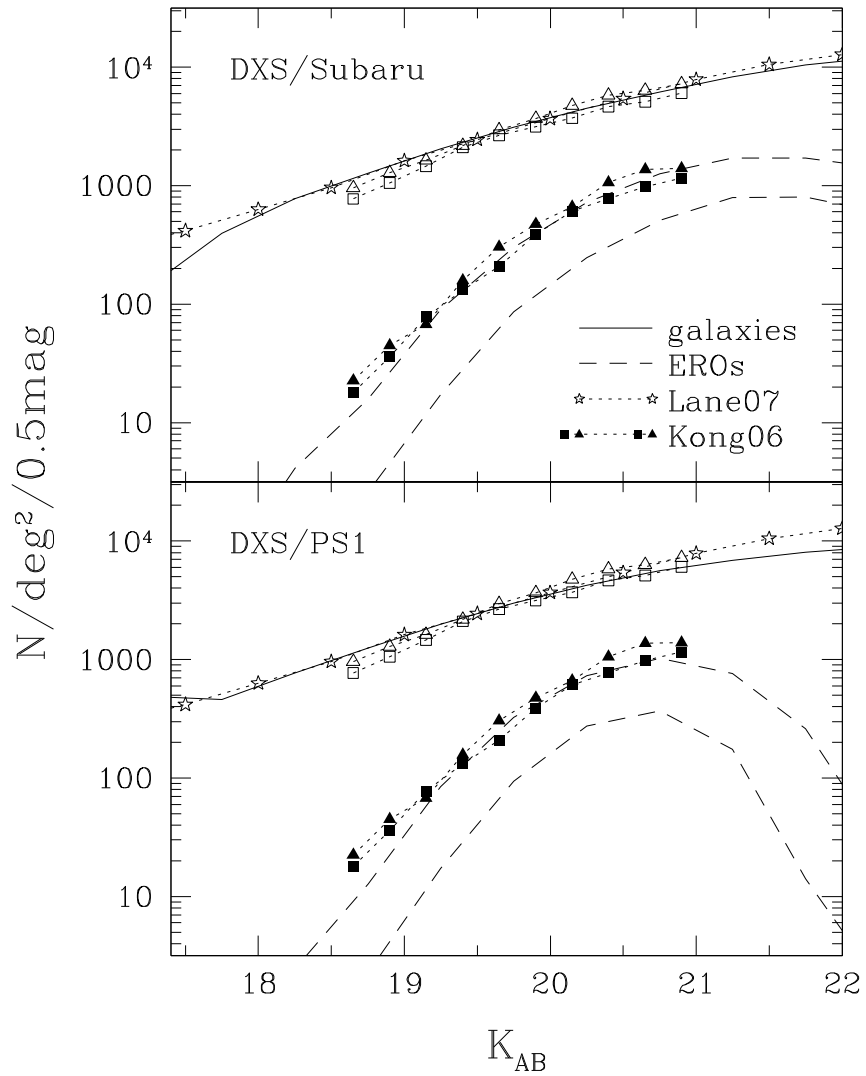
Figure 4.1: Number counts of galaxies (top lines) and EROs (bottom lines) from DXS/Subaru (top panel) and DXS/PS1 (bottom panel). The solid lines are for galaxies in this work, and dashed lines are for EROs with different colour cuts. The counts in Lane et al. (2007, stars) and Kong et al. (2006, triangles and squares) are also displayed.
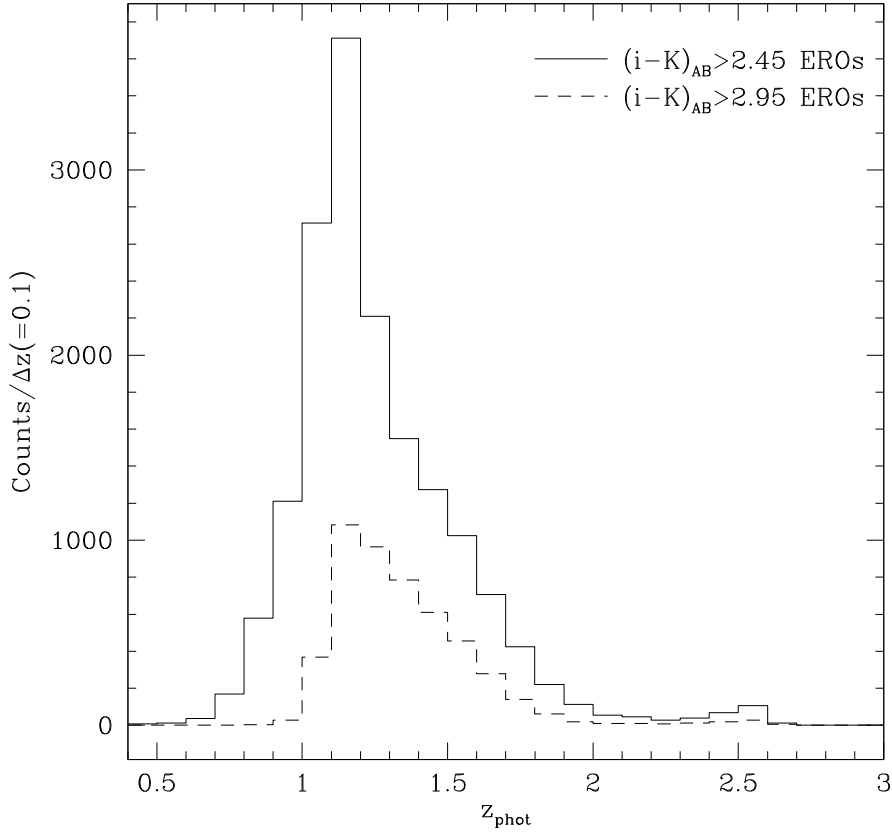
Figure 4.2: The photometric redshift distributions of EROs in the DXS/PS1. The solid histogram is for $(i-K)_{AB} > 2.45$ EROs, and the dashed one is for $(i-K)_{AB} > 2.95$ EROs.

Nevertheless, there are not enough spectroscopic samples at $z > 1$, where most EROs are located. Therefore we also applied the empirical method of Quadri & Williams (2010) to constrain the photometric redshift uncertainty for EROs. This method assumes that close pairs of galaxies show a significant probability of being located at the same redshift. We counted pairs of EROs having an angular separation $2.5'' < \theta < 15''$ and those with randomised position. Then the difference between two sets in $\Delta z/(1 + z_{spec})$ was used to measure the photometric redshift uncertainty of EROs. This gave a dispersion of $\sigma_z \sim 0.059$ which is consistent with NMAD from spectroscopic samples. Figure 4.2 shows the photometric redshift distributions of EROs in the DXS/PS1. The solid histogram is for $(i - K)_{AB} > 2.45$ EROs, and the dashed one is for $(i - K)_{AB} > 2.95$ EROs. It is apparent that most EROs are located at $z > 1$. However $(i - K)_{AB} > 2.45$ EROs also contain galaxies at $z < 1$.

4.3 Analysis methods

4.3.1 Angular correlation function

The angular two-point correlation function is the probability of finding a galaxy pair with respect to a random distribution (Peebles 1980). We used the estimator from Landy & Szalay (1993) which already came up in section 3.3.3 to estimate the angular two-point correlation function:

$$\omega_{obs}(\theta) = \frac{DD(\theta) - 2DR(\theta) + RR(\theta)}{RR(\theta)}, \tag{4.1}$$

where DD is the number of observed ERO pairs with separation interval $[\theta, \theta + \Delta\theta]$. For this study we applied $\Delta log\theta = 0.15$. DR and RR are data-random and random-random pairs in the same interval, respectively. All pair counts are normalised to have same totals. The random catalogue was generated with 50 times more random points than the observed EROs, and had the same angular mask as the EROs.

The error in the correlation function was estimated from the Jackknife resampling method to compute the deviation of the correlation functions between subfields. We divided the whole area into 25 subfields for DXS/Subaru and 30 subfields for DXS/PS1, then repeated the measurement of the correlation function. From each correlation function we can estimate the error with

$$\sigma^2(\theta) = \sum_{i=1}^{N} \frac{DR_i(\theta)}{DR(\theta)} [w_i(\theta) - w(\theta)]^2 \tag{4.2}$$

where w_i and DR_i are the correlation function and data-random pairs except ith subfield. Then the covariance matrix was calculated with

$$\mathbf{C_{ij}} = (\mathbf{N - 1})\langle[\mathbf{w}(\theta_\mathbf{i}) - \overline{\mathbf{w}(\theta_\mathbf{i})}] \cdot [\mathbf{w}(\theta_\mathbf{j}) - \overline{\mathbf{w}(\theta_\mathbf{j})}]\rangle, \tag{4.3}$$

where $\overline{w(\theta_i)}$ is the mean correlation function of jackknife subsamples in the ith bin. The covariance matrix was used to fit the halo model.

The restricted survey area leads to a negative offset of the observed correlation function from the actual one, which is known as the integral constraint (IC, Groth & Peebles 1977). In order to correct this bias, we applied the same method as Chapter

3 using the equation in Roche et al. (1999),

$$IC = \frac{\sum RR(\theta)w(\theta)}{\sum RR(\theta)}. \tag{4.4}$$

Since it is known that the correlation function of EROs is not described by a single power-law (Chapter 3; Gonzalez-Perez et al. 2011), the functional form of $w(\theta) = \alpha_1\theta^{-\beta_1} + \alpha_2\exp(\beta_2\theta)$ was regarded as the actual correlation function. On the other hand, the correlation function from the halo model can also be used as the actual correlation function (Wake et al. 2011). For redshift limited EROs in Chapters 4 and 5, we use the modelled correlation function to calculate the integral constraint. This method, however, is not appropriate for the whole ERO sample, since EROs are not selected as volume limited samples. We note that the integral constraint ranged from 0.004 to 0.008 for the whole ERO samples, and brighter or redder EROs have larger integral constraints. Moreover the value obtained from the halo models for redshift limited samples was between 0.006 and 0.010.

4.4   Results

4.4.1   Angular correlation function

It is known that clustering properties of EROs depend on magnitude and colour (Daddi et al. 2000; Roche et al. 2002, 2003; Brown et al. 2005; Georgakakis et al. 2005; Kong et al. 2006, 2009; Chapter 3). In this section we discuss the properties of the angular two-point correlation function of EROs from DXS/Subaru and DXS/PS1 samples which are currently the widest and deepest datasets for ERO studies.

Figure 4.3 shows the correlation functions of EROs selected using various criteria. All correlation functions in this figure show a clear break at $\sim 1.2'$ which corresponds to $\sim 1h^{-1}$ Mpc at $z \sim 1$. This break was already reported in Chapter 3 and implies that a single power-law can not describe the correlation function of EROs properly. Therefore we tried to fit a power-law $(w(\theta) = A_w\theta^{-\delta})$ to these correlation functions on small, $0.06' < \theta < 1.26'$, and large, $1.26' < \theta < 19.8'$, scales separately. The boundaries for fitting were determined to minimise the influence of the integral
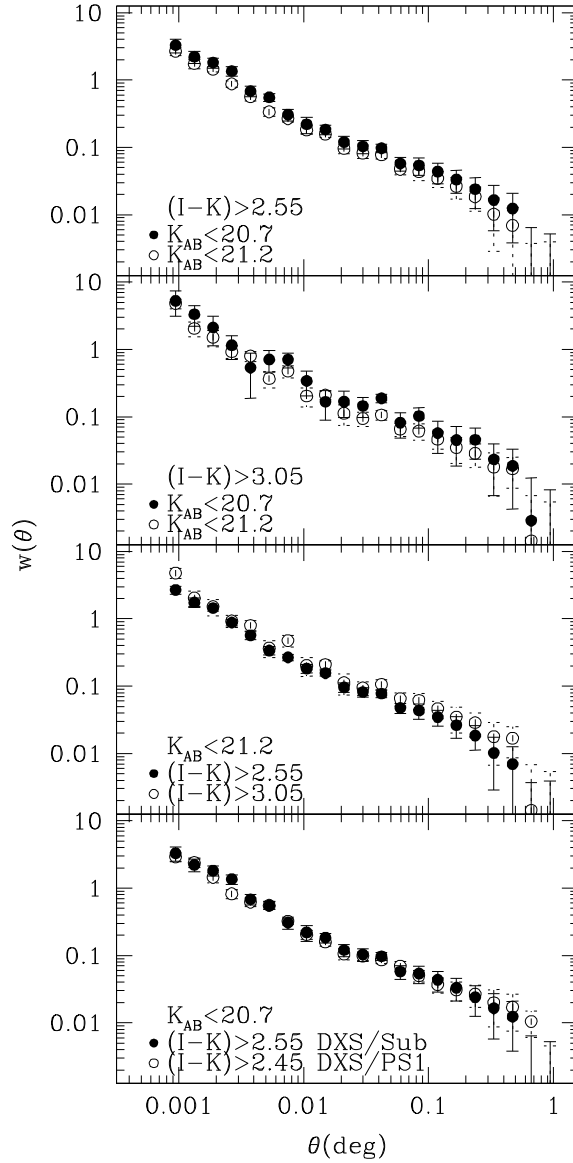
Figure 4.3: Angular two-point correlation functions of EROs with various criteria (top three panels). Those from DXS/Subaru and DXS/PS1 were compared in the bottom panel.

constraint on the large scales. The values measured are listed in the top four rows of table 4.1. Although it is affected by the different slopes, the amplitudes of redder or brighter EROs are larger than bluer or fainter samples. These features are confirmed in figure 4.3. The top two panels display the dependence on limiting magnitude, and the third panel from the top shows the colour dependence.

In order to check the consistency of these measurements we compared the results with those in Chapter 3 which showed good agreement with previously published results. The slopes $(\delta_{small}, \delta_{large})$ in Chapter 3 were $(0.99 \pm 0.09, 0.40 \pm 0.03)$ for $K_{AB} < 20.7, (i - K)_{AB} > 2.95$ EROs and $(1.00 \pm 0.05, 0.51 \pm 0.02)$ for $K_{AB} < 20.7, (i - K)_{AB} > 2.45$ EROs. The values using the same criteria in this work are $(1.05 \pm 0.15, 0.72 \pm 0.15)$ and $(1.10 \pm 0.07, 0.68 \pm 0.12)$. On small scales these values are in agreement within the uncertainty range. However the correlation functions in this work are slightly steeper than previous results. Since we used a smaller area in Chapter 3, those results might be more affected by cosmic variance, explaining the differences on the large scales. The most apparent point is that the correlation function is steeper on small scales and flatter on large scales than the widely used single power-law with $\delta = 0.8$ assumed in previous studies. Furthermore to compare amplitudes directly, we measured the amplitudes again with fixed slopes of $\delta = 0.99$ and 0.40 for small and large scales respectively. For $K_{AB} < 20.7, (I - K)_{AB} > 3.05$ EROs, the amplitudes $(A_w^{small}, A_w^{large})$ were $(4.14 \pm 0.3, 42.05 \pm 0.9) \times 10^{-3}$ in Chapter 3, and $(3.66 \pm 0.5, 33.26 \pm 3.7) \times 10^{-3}$ in this work. These are also consistent on small scales. Overall the measurements in this work are consistent with previous work, although wider data are necessary to confirm this on large scales. In the bottom panel of figure 4.3, we compare the angular correlation functions from DXS/Subaru and DXS/PS1 samples. As mentioned above the area for DXS/PS1 is larger than that of DXS/Subaru, but DXS/Subaru is deeper. The correlation functions of EROs from the different optical datasets are well matched. So we assumed that there is no significant bias for DXS/PS1 caused by the optical dataset, and used DXS/PS1 EROs to estimate the halo properties in the next Chapter.

Additionally photometric redshifts provide an opportunity to compare the clustering properties of EROs in different redshift bins. From the DXS/PS1 catalogue we

Table 4.1: The amplitudes A_ω and slopes of the correlation functions of DXS/Subaru EROs (top 4 rows) for the power-law fit on small and large scales. Bottom 3 rows are same parameters for DXS/PS1 EROs at different redshift bins.

Criteria	$A_\omega^{small} \times 10^3$	$A_\omega^{large} \times 10^3$	slope^{small}	slope^{large}	$\chi^2_{small,large}$	Num.
$(I-K) > 2.55, K_{AB} < 20.7$	1.63±0.6	9.66±3.5	1.10±0.07	0.68±0.12	0.5, 0.3	6,159
$(I-K) > 2.55, K_{AB} < 21.2$	1.42±0.4	7.35±2.3	1.08±0.05	0.69±0.10	1.0, 0.4	11,726
$(I-K) > 3.05, K_{AB} < 20.7$	2.74±2.2	14.45±6.5	1.05±0.15	0.72±0.15	0.6, 0.8	2,012
$(I-K) > 3.05, K_{AB} < 21.2$	3.07±1.4	11.89±4.2	0.98±0.09	0.62±0.12	0.8, 0.3	4,343
$1.00 < z < 1.20, M_K < -23$	1.95±1.1	12.07±4.9	1.14±0.11	0.70±0.14	0.7, 0.3	2,882
$1.15 < z < 1.45, M_K < -23$	1.65±0.7	8.70±3.2	1.15±0.08	0.73±0.12	1.8, 0.7	3,878
$1.40 < z < 1.80, M_K < -23$	3.94±2.7	20.85±6.4	0.93±0.14	0.48±0.12	0.4, 0.4	3,021
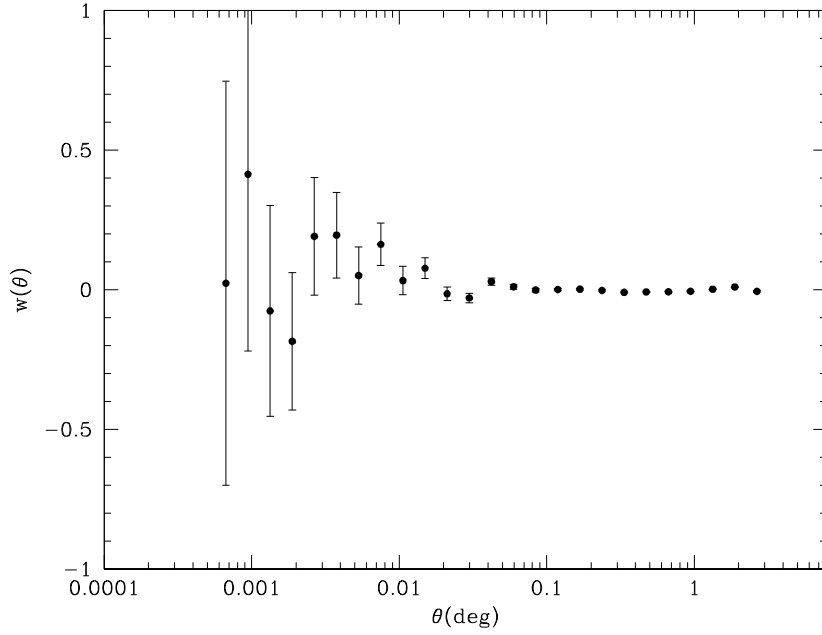
Figure 4.4: The cross-correlation function of EROs in the lowest and highest redshift bins.

classified EROs based on their redshift and absolute magnitude. Firstly we applied a K-band absolute magnitude cut ($M_K < -23$) to select EROs having a similar stellar mass range in different redshift bins. The K-band absolute magnitude was calculated using the passive evolution correction from the Bruzual & Charlot (2003) GALAXEV code. The applied formation redshift and metallicity were $4 < z_f < 5$ and around solar metallicity. Then to compare results at different redshifts, the EROs were split into three redshift bins ($1.0 < z < 1.2, 1.15 < z < 1.45$ and $1.4 < z < 1.8$). The bin size was determined to get large enough samples and uncontaminated samples in the lowest and highest redshift bins. We note that the cross-correlation function of ERO subsets at $1.0 < z < 1.2$ and $1.4 < z < 1.8$ showed ~ 0 amplitude meaning they are independent. Figure 4.4 displays the cross-correlation function of EROs in the lowest and highest redshift bins. Finally a power-law fit was performed on small and large scales separately. The same fitting range as above was used. Figure 4.5 shows the angular two-point correlation functions of DXS/PS1 EROs at $1.0 < z < 1.2$ (top), $1.15 < z < 1.45$ (middle) and $1.4 < z < 1.8$ (bottom). Dotted lines indicate the power-law fits on small and large scales separately. The bottom three rows in table 4.1 list the fitted results. Although the correlation function shows a slightly flatter shape in the highest redshift bin than the others, all the estimated power-law slopes have similar values within the uncertainty range. We also note that the amplitudes on large scales with a fixed power-slope ($\delta = 0.4$) are 0.026±0.002 at $1.0 < z < 1.2$, 0.020±0.002 at $1.15 < z < 1.45$, and 0.025±0.002 at $1.4 < z < 1.8$. These similar amplitudes on large scales indicate a higher bias at higher redshift. This will be discussed in the next Chapter.

4.5 Conclusion

In this Chapter we merged the DXS Elais-N1 catalogue with Subaru and PS1 optical catalogues. Then we classified EROs into sub-samples with colour, magnitude and redshift criteria to investigate the angular clustering of EROs.

The $(I - K)$ and $(i - K)$ colours were applied to extract EROs from the 3.88
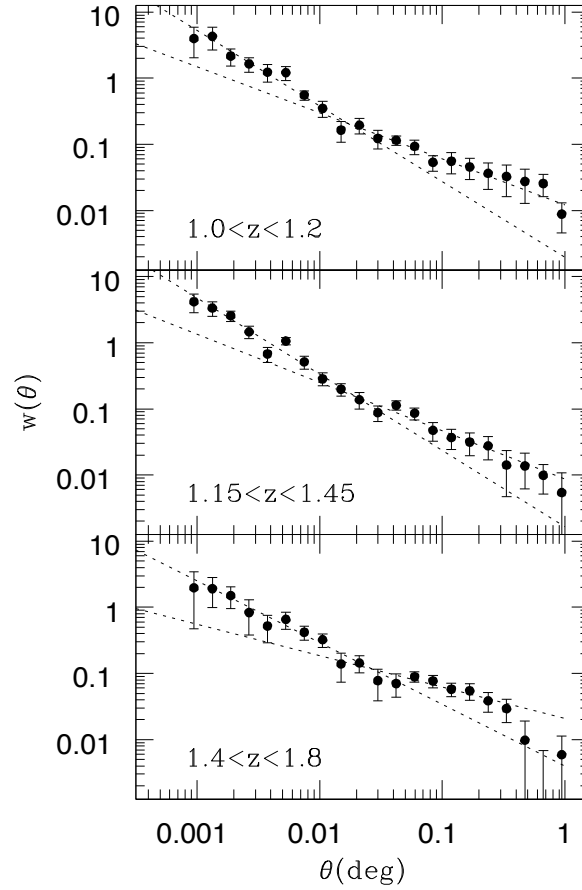
Figure 4.5: Angular two-point correlation functions of DXS/PS1 EROs at $1.0 < z < 1.2$ (top), $1.15 < z < 1.45$ (middle) and $1.4 < z < 1.8$ (bottom). Dotted lines indicate the power-law fits on small and large scales separately.

deg^2 DXS/Subaru and the 5.33 deg^2 DXS/PS1 catalogues, respectively. We detected 17,250 EROs from DXS/PS1 and 23,916 EROs from DXS/Subaru. The number counts of EROs are well matched to previous results. The photometric redshift of galaxies in DXS/PS1 were derived from $grizJK$ and SWIRE IRAC colours. EROs were split into subsamples of different redshift using photometric redshifts and the absolute magnitude ($M_K < -23$).

The angular correlation functions of EROs were measured with several colour and magnitude cuts from the DXS/Subaru sample. All these correlation functions showed a clear break at $\sim 1.2'$ which means the angular correlation function of EROs can not be described by a single power-law. Furthermore redder or brighter EROs showed higher amplitudes than bluer or fainter ones. The correlation functions from DXS/PS1 and DXS/Subaru samples with the same criteria also showed good agreement. The correlation functions at different redshifts had similar amplitudes on large scales, which indicates a higher bias at higher redshift.

Chapter 5

Halo model for EROs

5.1 Introduction

In the ΛCDM paradigm, the measurement of the clustering of galaxies makes it possible to link galaxy properties with halo properties, since more clustered or more massive galaxies reside in more massive haloes. The most popular methods linking them are the two-point correlation function of galaxies (Peebles 1980) and halo modelling with the Halo Occupation Distribution (HOD) framework (Jing, Mo & Boerner 1998; Ma & Fry 2000; Peacock & Smith 2000; Seljak 2000; Scoccimarro et al. 2001; Berlind & Weinberg 2002; Cooray & Sheth 2002). The two-point correlation function describes the probability of the existence of a galaxy pair at a specific scale. The HOD presents the probability of a certain type of galaxy being hosted by a halo of a given mass. From the HOD the observed correlation function can be predicted with some theoretical estimates and certain cosmological parameters.

Recently wide surveys have provided an opportunity to measure the clustering of galaxies with various criteria accurately. From optical imaging and spectroscopic surveys, many sub-samples with a certain luminosity or colour at relatively low redshift have been selected, and their clustering properties were measured (Norberg et al. 2001, 2002; Zehavi et al. 2002, 2005; Coil et al. 2008; Ross & Brunner 2009; Ross, Percival & Brunner 2010; Zehavi et al. 2011). In addition the halo properties of luminous red galaxies (LRGs) at $z < 1$ were predicted with accurate spectroscopic information (Blake, Collister & Lahav 2008; Wake et al. 2008; Sawangwit et al.

2009). For quasars or Active Galactic Nuclei (AGN), Coil et al. (2009) and Hickox et al. (2011) have used the correlation function to explain and to compare their properties with others.

In this Chapter, we use EROs in different redshift bins selected from the DXS/PS1 sample in Chapter 4. The properties of dark matter halo hosting EROs are investigated through fitting the halo model to the observed angular correlation function of EROs. In addition, the predicted clustering and halo properties from the semi-analytic model are compared to the results estimated by halo modelling.

Unless otherwise noted, the photometry is quoted in the AB scale in this Chapter. We assume the following cosmology : $\Omega_m =0.27$, $\Omega_\Lambda = 0.73$, $\sigma_8 = 0.8$ and $H_o = 100$ h km s^{-1} Mpc^{-1} with $h =0.73$.

5.2   Analysis methods

5.2.1   Halo modelling

The halo model (Cooray & Sheth 2002 for a review) is widely used to estimate dark matter halo properties (Blake et al. 2008; Wake et al. 2008; Ross & Brunner 2009; Zehavi et al. 2011). We applied it to produce angular correlation functions of EROs and to measure properties linked with the dark matter haloes hosting EROs.

The halo occupation distribution (HOD) describes the probability of a certain type of galaxy to be hosted by a halo of a given mass (M). In the halo model, galaxies are separated into centrals and satellites. The mean number of galaxies, $N(M)$, is the combination of that for the central galaxies, $N_c(M)$ and satellites, $N_s(M)$ (Zheng et al. 2005; Blake et al. 2008; Wake et al. 2008; Ross & Brunner 2009) by

$$N(M) = N_c(M)(1 + N_s(M)), \tag{5.1}$$

where the mean number density of the central galaxies and satellites are assumed to be described by

$$N_c(M) = 0.5 \left[1 + \text{erf} \left(\frac{\log_{10}(M/M_{cut})}{\sigma_{cut}} \right) \right] \tag{5.2}$$

and

$$N_s(M) = \left(\frac{M}{M_0}\right)^\alpha. \tag{5.3}$$

In order to generate the real-space correlation function we followed the scheme in Ross & Brunner (2009). Firstly we modelled the power spectrum contributed by galaxies in a single halo (1-halo term) and those in separate haloes (2-halo term). Also the power spectrum for the 1-halo term is split into that of central-satellite pairs ($P_{cs}(k)$) and satellite-satellite pairs ($P_{ss}(k)$). The equations for each term are

$$P_{cs}(k) = \int_{M_{vir}(r)}^{\infty} dM n(M) N_c(M) \frac{2N_s(M)u(k|M)}{n_g^2}, \tag{5.4}$$

$$P_{ss}(k) = \int_0^{\infty} dM n(M) N_c(M) \frac{(N_s(M)u(k|M))^2}{n_g^2} \tag{5.5}$$

and

$$P_{2h}(k,r) = P_{mat}(k) \tag{5.6}$$

$$\times \left[\int_0^{M_{lim}(r)} dM n(M) b(M,r) \frac{N(M)}{n_g'} u(k|M) \right]^2, \tag{5.7}$$

where $n(M)$ is the halo mass function parameterised in Tinker et al. (2010), $u(k|M)$ is the Fourier transform of the halo density profile in Navarro, Frenk & White (1997) and $P_{mat}(k)$ indicates the matter power spectrum at the redshift of the samples. For generating $P_{mat}(k)$ we used the 'CAMB' software package (Lewis, Challinor & Lasenby 2000) including the fitting formulae of Smith et al. (2003) for the correction of non-linear growth. The average number density of galaxies is n_g, and the restricted number density of galaxies is n_g'. Those are expressed as

$$n_g = \int_0^{\infty} dM n(M) N(M) \tag{5.8}$$

and

$$n_g' = \int_0^{M_{lim}(r)} dM n(M) N(M). \tag{5.9}$$

The parameter $M_{lim}(r)$ is the mass limit due to halo exclusion, which is determined using the scheme from Tinker et al. (2005). The scale-dependent bias, $b(M,r)$, is calculated from the equation in Tinker et al. (2005) of

$$b^2(M,r) = B^2(M) \frac{[1 + 1.17\xi_m(r)]^{1.49}}{[1 + 0.69\xi_m(r)]^{2.09}}, \tag{5.10}$$

where $\xi_m(r)$ is the non-linear real-space matter correlation function and the halo bias $(B(M))$ is calculated from the function in Tinker et al. (2010). The calculated power-spectra were converted into real-space correlation functions using Fourier transformations

The halo model with three parameters $(\sigma_{cut}, M_0$ and $\alpha)$ was used to produce the angular correlation function. In this case, M_{cut} was fixed by matching the observed number density with other given parameters. The modelled correlation function was projected to angular space using the Limber equation (Limber 1954). Then the covariance matrix was used to find the best parameters having the minimum χ^2 value. The fitting range was $0.06' < \theta < 19.8'$ where the influence of integral constraint was minimised.

From the fitted parameters, the effective mass (M_{eff}), the effective bias (b_g) and the satellite fraction can be estimated by

$$M_{eff} = \int dM M n(M) N(M)/n_g, \tag{5.11}$$

$$b_g = \int dM B(M) n(M) N(M)/n_g \tag{5.12}$$

and

$$f_{sat} = \int dM n(M) N_c(M) N_s(M)/n_g. \tag{5.13}$$

In order to determine the properties of haloes hosting EROs at different redshifts, we compare all the fitted and estimated values for each ERO subset.

5.3   Results

5.3.1   Halo modelling

In this section we report the properties of haloes hosting EROs at different redshifts. The angular correlation functions for DXS/PS1 EROs in different redshift bins with $M_K < -23$ were used for the halo modelling. The halo models were generated at the median redshifts of the bins, $z = 1.12, 1.28$ and 1.55. In order to estimate parameters, the halo model with the three free parameters $(\sigma_{cut}, M_0$ and $\alpha)$ was applied at each redshift.

Figure 5.1 shows the angular correlation functions (points) of EROs brighter than $M_K = -23$ in different redshift bins, and best fit halo models (lines). It is apparent that the correlation functions of all ERO subsets have breaks, and are fitted well by the standard halo model. The HOD fit parameters are listed in table 5.1.

In figure 5.2 the estimated bias (top), effective mass (middle) and satellite fraction (bottom) are displayed. The EROs at higher redshift show a higher bias which is a similar trend to previous results for various kinds of populations (Blake et al. 2008; Wake et al. 2008; Sawangwit et al. 2009 for Luminous Red Galaxies (LRG), Matsuoka et al. 2011; Wake et al. 2011 for stellar mass limited samples and Ross, Percival & Brunner 2010 for absolute magnitude cut samples). The bias of EROs reported previously was 2.7 ± 0.1 in Moustakas & Somerville (2002) which is similar to our measurements, although they applied a single power-law and used a different colour criterion ($(I - H)_{vega} > 3$) for the Las Campanas Infrared Survey data (McCarthy et al. 2001; Firth et al. 2002). These values are similar to those for low redshift LRGs having $b_g \cong 2 - 3$ (Blake et al. 2008; Wake et al. 2008; Sawangwit et al. 2009). If EROs have similar stellar masses as LRGs, EROs should be more biased than low redshift LRGs. However we note that the median stellar mass of an SDSS LRG is $\sim 10^{11.5} M_\odot$ with a narrow distribution (Barber, Meiksin & Murphy 2007), but in the case of EROs at $K_{vega} < 19.7$, the distribution shows a peak at $\sim 10^{11.3} M_\odot$ and a sharp cut-off at $\sim 10^{11.5} M_\odot$ (Conselice et al. 2008). Therefore our samples probably have slightly lower stellar masses than LRGs at lower redshift.

We also found that these EROs reside in haloes more massive than $\sim 10^{12.9} h^{-1} M_\odot$ and EROs at higher redshift are in slightly more massive haloes than lower redshift. Moustakas & Somerville (2002) estimated the average halo mass hosting EROs as $> 10^{13} h^{-1} M_\odot$ which are similar to our results. On the other hand, Hartley et al. (2010) reported that passive galaxies having $M_{K,vega} < -25$ are located in haloes more massive than $10^{13} h^{-1} M_\odot$. This means our measurements show slightly lower halo masses than results for passive galaxies despite having the similar absolute magnitude range. In addition if we assume dark matter haloes in ΛCDM cosmology grow with time, a higher halo mass at higher redshift is not expected. However it
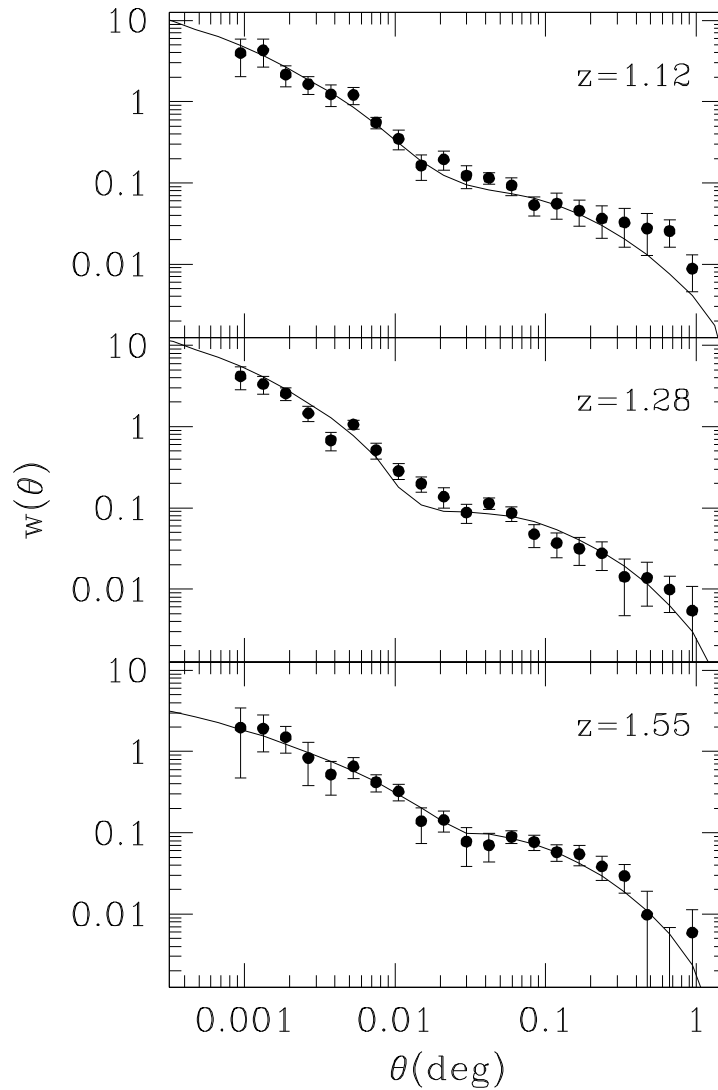
Figure 5.1: Angular correlation functions of M_K cut EROs at different redshifts. Points indicate the correlation function and solid lines are best fit halo models.
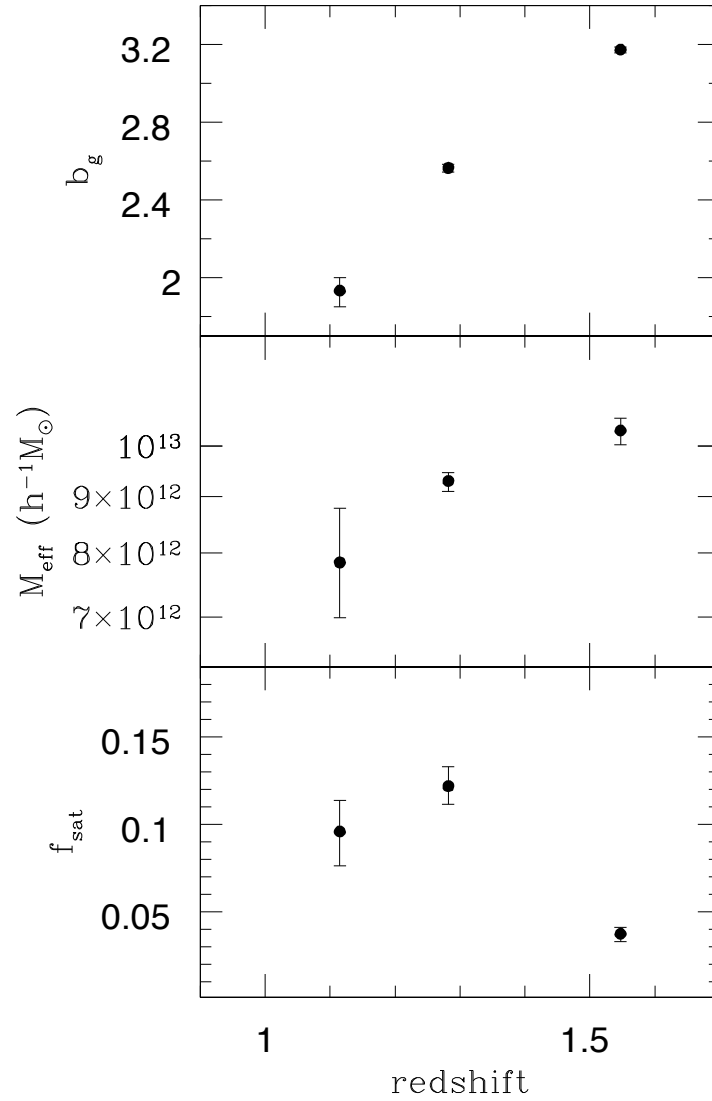
Figure 5.2: The estimated bias (top), effective mass (middle) and satellite fraction (bottom) when three-parameter halo model was applied.

Table 5.1: HOD and estimated parameters for $M_K < -23$ EROs at different redshift bins. The number density is in units of $10^{-4} h^3 \mathrm{Mpc}^{-3}$.

median z	σ_{cut}	$\log(M_{cut}/M_\odot h^{-1})$	$\log(M_0/M_\odot h^{-1})$	α	n_g	b_g	$\log(M_{eff}/M_\odot h^{-1})$	f_{sat}	χ^2/dof
1.12	$0.91^{+0.09}_{-0.06}$	$12.966^{+0.118}_{-0.064}$	$13.569^{+0.023}_{-0.017}$	$1.23^{+0.13}_{-0.09}$	9.7	$1.933^{+0.065}_{-0.084}$	$12.895^{+0.049}_{-0.050}$	$0.096^{+0.018}_{-0.020}$	1.43
1.28	$0.14^{+0.04}_{-0.05}$	$12.506^{+0.009}_{-0.013}$	$13.680^{+0.015}_{-0.018}$	$1.11^{+0.03}_{-0.03}$	7.7	$2.564^{+0.019}_{-0.023}$	$12.968^{+0.008}_{-0.010}$	$0.122^{+0.011}_{-0.010}$	3.07
1.55	$0.01^{+0.02}_{-0.01}$	$12.575^{+0.004}_{-0.004}$	$13.714^{+0.019}_{-0.012}$	$2.45^{+0.07}_{-0.09}$	4.0	$3.172^{+0.013}_{-0.018}$	$13.014^{+0.011}_{-0.013}$	$0.037^{+0.004}_{-0.005}$	1.12

is known that EROs can be split into old, passive and dusty star-forming galaxies (Pozzetti & Mannucci 2000; Smail et al. 2002; Roche et al. 2002; Cimatti et al. 2002, 2003; Moustakas et al. 2004; Sawicki et al. 2005; Simpson et al. 2006; Conselice et al. 2008; Kong et al. 2009). In Chapter 3 the fraction of old, passive EROs was more than ~ 60 per cent. In this work it is not possible to distinguish the whole sample into these two sub-populations by $(i - K)$ versus $(J - K)$ diagram due to the lack of full J-band imaging. So we simply apply the criterion to the two-colour diagram for the region where J-band imaging exists. The fraction of old, passive EROs was 45.4 per cent at $z = 1.12$ and 54.4 per cent at $z = 1.55$. The significant fraction of dusty, star-forming galaxies may dilute the clustering of EROs which causes lower halo masses than pure passive galaxy samples. Also the higher old, passive EROs fraction may contribute to the increased halo masses at higher redshift.

5.4   Discussion

5.4.1   Comparison with stellar mass limited samples

Recent multi-wavelength surveys make it possible to study details of galaxies matching various criteria. One of these is the clustering of stellar mass limited samples at different redshifts (Foucaud et al. 2010; Matsuoka et al. 2011; Wake et al. 2011). In this section we compare our results with those in Wake et al. (2011). Although EROs are not stellar mass limited samples, the comparison with stellar mass limited samples may give some constraints which help explain the properties of EROs and the haloes hosting them.

Wake et al. (2011) used the NEWFIRM medium band survey (NMBS; van Dokkum et al. 2009; Brammer et al. 2009; van Dokkum et al. 2010; Whitaker et al. 2011) data. The NMBS mapped two ~ 0.25 deg^2 areas which together are a smaller area than this work, but the five medium bands with other multi-wavelength datasets and their superior depth are helpful to categorise these sub-samples precisely. They also applied the halo model to estimate parameters constraining dark matter halo properties. However σ_{cut} for the HOD of central galaxies and the power-law slope,

α, for satellites were fixed at 0.15 and 1, respectively. Therefore we fixed those parameters at same values to directly compare results. It is also helpful to find the difference of only two mass cuts, M_{cut} and M_0, of HODs in various redshift bins. In addition there were two options for fitting both clustering and number density or clustering only in Wake et al. (2011). For EROs we also followed these options. In order to do that, M_0 was a free parameter and M_{cut} was estimated to match the observed number density for the first option. In the latter case the two mass cuts were free parameters and the number density was calculated using the halo model.

Figure 5.3 shows the angular correlation functions of M_K cut EROs at different redshifts (points) with halo models fitted to both clustering and number density (solid line) and clustering only (dotted line). All measured parameters are listed in table 5.2. The overall trend of measured parameters are similar to those of the three-parameter fits in the previous section. The halo hosting EROs at higher redshift show a higher mass cut for the HOD, higher bias and a lower satellite fraction than found at lower redshift. In figure 5.4 estimated values in this work (filled circles) and Wake et al. (2011, open circles) are compared. For the Wake et al. (2011) points, the results of various stellar mass limited samples are displayed, which are $10^{(9.85,10.00,10.30,10.48,10.70)}M_\odot$ at $z = 1.1$ and $10^{(10.00,10.30,10.48,10.70,10.78)}M_\odot$ at $z = 1.5$. The highest points in bias and M_{eff} and the lowest points in f_{sat} are for the highest stellar mass cut sample at each redshift. It is clear that haloes hosting EROs contain less satellites than those in Wake et al. (2011). On the other hand our results may show comparable bias and effective mass to Wake et al. (2011).

It can be easily explained that the lower satellite fraction is caused by the selection of EROs, since EROs are mainly comprised of massive galaxies and have red colours. However the comparable bias and M_{eff} to Wake et al. (2011) may not be consistent with previous results, as more massive or brighter galaxies reside in more massive haloes (Zehavi et al. 2005, 2011; Foucaud et al. 2010; Hartley et al. 2010; Matsuoka et al. 2011; Furusawa et al. 2011) and show a higher bias (Coil et al. 2006; Ross & Brunner 2009; Zehavi 2011), if we assume EROs have stellar masses larger than $10^{11}M_\odot$. One of the possible reasons may be the stellar mass distribution of EROs, as EROs are not selected to be a stellar mass limited

sample. From the stellar mass distribution in Concelice et al. (2008), EROs contain $< 10^{11} M_\odot$ galaxies as well. This was confirmed by Hempel et al. (2011) from deeper observational data. Although we applied a K-band absolute magnitude cut, there are still $< 10^{11} M_\odot$ galaxies when the magnitude range was applied to the Hempel et al. (2011) sample. Another possible reason may be the effect of cosmic variance. The NMBS covered two ~ 0.25 deg^2 fields, and Wake et al. (2011) pointed out the discrepancy in the angular correlation functions for each field on large scales. In fact, the measured angular correlation function of $> 10^{10.78} M_\odot$ samples at $z = 1.5$ in Wake et al. (2011) shows significantly higher amplitude than the M_K cut EROs at $z = 1.55$ in the 2-halo term regime.

We also note the recent results on the mass of dark matter haloes estimated from the real-space correlation length and models in Mo & White (2002). Furusawa et al. (2011) used Subaru and UKIDSS Ultra Deep Survey (UDS) datasets to address the mass-dependent clustering. They estimated the halo mass as $10^{13.78} M_\odot$ for $10^{10.86} M_\odot < M_* < 10^{11.26} M_\odot$ galaxies at $z < 1.8$. However this is higher than Foucaud et al. (2010) measured from the Palomar/DEEP2 survey. Foucaud et al. (2010) suggested the halo mass as $10^{12.70} h^{-1} M_\odot$ at $0.8 < z < 1.2$ and $10^{13.17} h^{-1} M_\odot$ at $1.2 < z < 1.6$ for $10^{11.0} M_\odot < M_* < 10^{11.5} M_\odot$ galaxies, which are similar to our measurements. Furusawa et al. (2011) and Foucaud et al. (2010) used the Mo & White (2002) model assuming only one galaxy per halo, but Foucaud et al. (2010) also applied the correction for the HOD including satellites. If this correction is applied, slightly higher correlation length is necessary to get the same halo mass. Thus it is possible that Furusawa et al (2011) might slightly overestimate the halo mass, since the estimated correlation lengths of both results were similar. Moreover, in the case of bias, Foucaud et al. (2010) suggested the bias was 1.8 ± 0.4 at $0.8 < z < 1.2$ and 2.8 ± 0.6 at $1.2 < z < 1.6$ for $10^{11.0} M_\odot < M_* < 10^{11.5} M_\odot$ galaxies, which are also similar to our measurements. Therefore our measurements may mean that EROs reside in haloes having similar properties to those hosting $10^{11} M_\odot < M_* < 10^{11.5} M_\odot$ galaxies.

Finally we briefly note that the discrepancy in measured parameters when the halo model is fitted to both clustering and density or clustering only. Matsuoka et
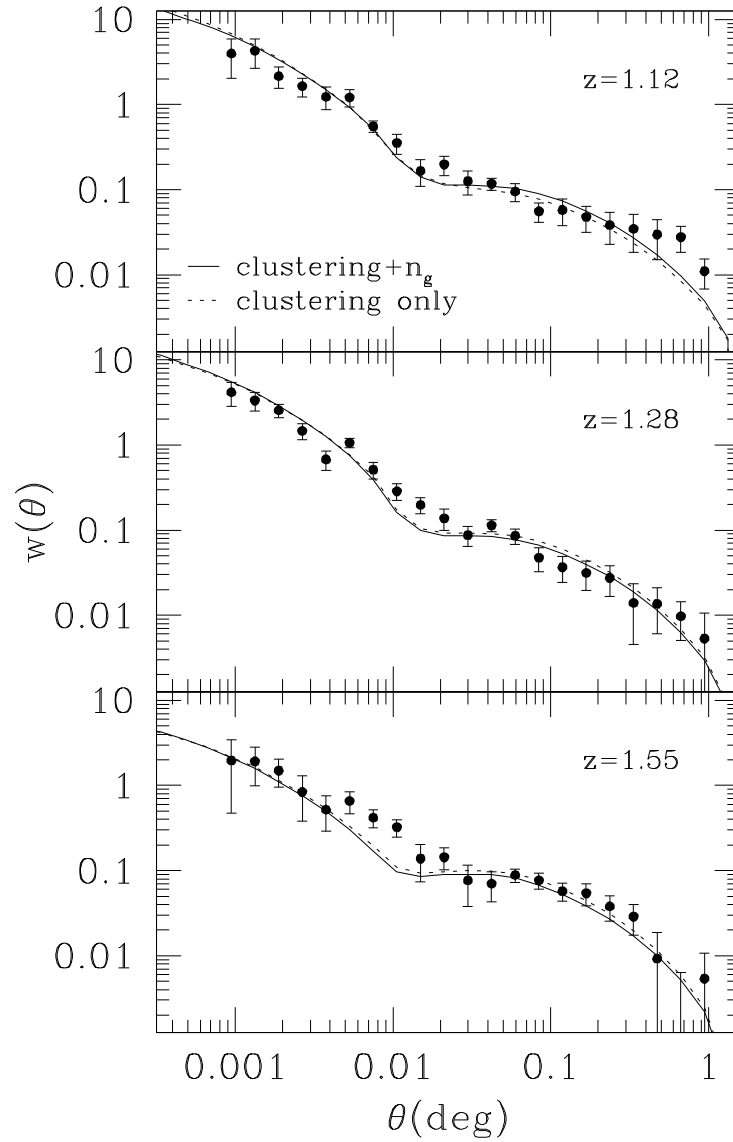
Figure 5.3: Angular correlation functions of M_K cut EROs at different redshifts with the best fit halo model. Points indicate the angular correlation function. Solid and dotted lines are best fit halo models by both clustering and number density and clustering only, respectively.

Table 5.2: HOD and estimated parameters fitted to both clustering and number density and clustering only with fixed σ_{cut} and α. The number density is in units of $10^{-4} h^3 \mathrm{Mpc}^{-3}$.

median z	$\log(M_{cut}/M_\odot h^{-1})$	$\log(M_0/M_\odot h^{-1})$	n_g	b_g	$\log(M_{eff}/M_\odot h^{-1})$	f_{sat}	χ^2/dof
clustering and n_g							
1.12	$12.475^{+0.004}_{-0.004}$	$13.795^{+0.021}_{-0.026}$	9.7	$2.272^{+0.010}_{-0.009}$	$12.968^{+0.007}_{-0.006}$	$0.112^{+0.007}_{-0.005}$	2.32
1.28	$12.506^{+0.004}_{-0.004}$	$13.756^{+0.008}_{-0.023}$	7.7	$2.544^{+0.004}_{-0.008}$	$12.952^{+0.003}_{-0.004}$	$0.119^{+0.006}_{-0.003}$	2.76
1.55	$12.588^{+0.004}_{-0.004}$	$14.428^{+0.105}_{-0.070}$	4.0	$3.039^{+0.003}_{-0.003}$	$12.922^{+0.002}_{-0.002}$	$0.029^{+0.005}_{-0.006}$	3.07
clustering only							
1.12	$12.268^{+0.012}_{-0.020}$	$13.346^{+0.035}_{-0.031}$	$19.0^{+1.2}_{-0.8}$	$2.100^{+0.023}_{-0.033}$	$12.891^{+0.018}_{-0.024}$	$0.195^{+0.015}_{-0.017}$	2.04
1.28	$12.621^{+0.009}_{-0.011}$	$14.005^{+0.023}_{-0.022}$	$5.2^{+0.2}_{-0.2}$	$2.693^{+0.017}_{-0.020}$	$13.018^{+0.009}_{-0.010}$	$0.086^{+0.006}_{-0.005}$	2.93
1.55	$12.705^{+0.022}_{-0.013}$	$14.659^{+0.094}_{-0.050}$	$2.6^{+0.1}_{-0.2}$	$3.260^{+0.046}_{-0.029}$	$13.010^{+0.018}_{-0.012}$	$0.022^{+0.004}_{-0.004}$	3.17
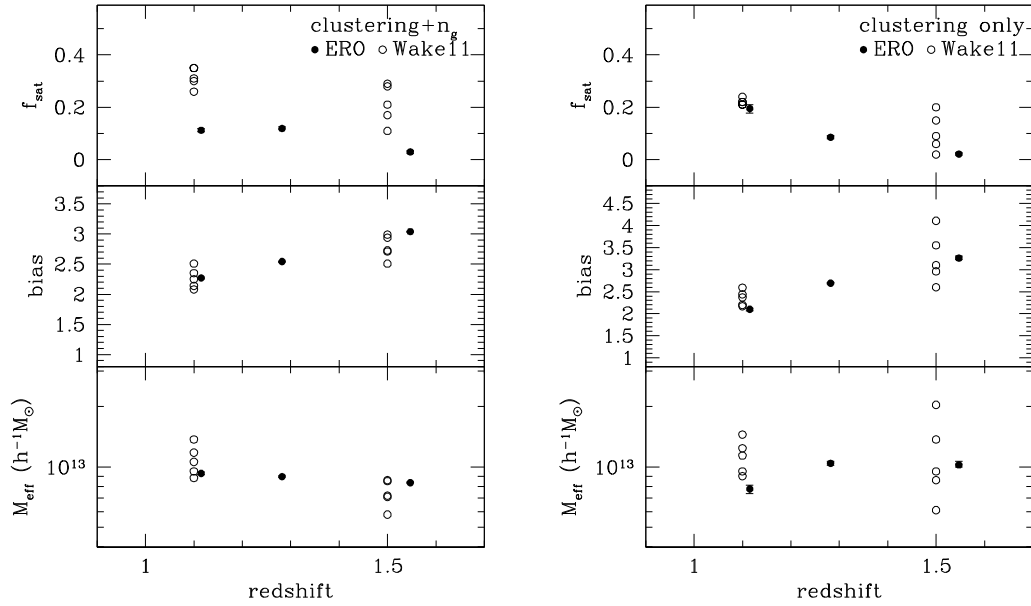
Figure 5.4: Comparison of estimated parameters with those in Wake et al. (2011). Filled circles indicate results for EROs, and open circles are for those in Wake et al. (2011) with various stellar mass cuts at each redshift (see text for more details).

al. (2011) and Wake et al. (2011) point out that halo masses and bias fitted to clustering only are larger, and the predicted number density using the halo model fitted to only clustering are not consistent with the observed density. It is the same situation for EROs. In our case, EROs at $z = 1.28$ and 1.55 show exactly the same features, but the trend is reversed at $z = 1.12$. Wake et al. (2011) suggest that the further calibration of the halo bias relation or more understanding of the galaxy distribution in the halo may be necessary.

5.4.2 GALFORM prediction

Nowadays hierarchical galaxy formation models have succeeded in predicting various phenomena over a wide redshift range. Recently Gonzalez-Perez et al. (2009, 2011) compared the predicted properties of EROs from the GALFORM semi-analytical galaxy formation model (Cole et al. 2000) with observed results. Gonzalez-Perez et al. (2009) presented predictions of the basic properties such as number counts, redshift distribution, morphology, stellar mass, halo mass and age of stellar popula-

tions using two developments of GALFORM : Baugh et al. (2005) and Bower et al. (2006) models. The overall properties of GALFORM EROs, especially using the Bower et al. (2006) model, show good agreement with observational results. Most GALFORM EROs are quiescent galaxies, and had stellar masses $> 10^{11} M_\odot$ at $z > 1$ (Gonzalez-Perez et al. 2009). In addition Gonzalez-Perez et al. (2011) compared the predicted clustering properties of EROs with the observed clustering. In this section we focus on the properties of clustering and haloes hosting EROs using our halo models and semi-analytic models of Gonzalez-Perez et al. (2011).

In figure 5.5 the angular correlation functions of M_K cut EROs (points) are compared with those predicted by the semi-analytic model with same criteria (open circles) at $z = 1.12$ (top) and 1.55 (bottom). To transform the predicted real-space correlation function from GALFORM to the angular correlation function, the observed redshift distribution of EROs was applied. At $z = 1.12$ both correlation functions show good agreement up to $\theta < 18'$, and the observed one is slightly higher on larger scales. On the other hand, they show a discrepancy at $\theta > 2.4'$ for $z = 1.55$ EROs. There may be a few possible reasons explaining these differences as discussed in Gonzalez-Perez et al. (2011). Firstly the colour criterion can affect the sampling. In fact Gonzalez-Perez et al. (2011) pointed out that the correlation function of $(i - K)_{vega} > 4.5$ EROs in GALFORM was well matched with that of $(i - K)_{vega} > 4.0$ samples from observational data. Secondly the limitations of the observational data can lead to the differences. The cosmic variance and integral constraint are the main factors preventing accurate measurements on large scales. Actually the calculated integral constraint ranges from 0.006 to 0.010, so it is significant on large scales.

Now we can directly compare some properties estimated by the halo model with theoretical predictions. Top two rows in Table 5.3 list real-space correlation lengths, number densities, satellite fractions and halo masses (median, 10 and 90 per cent range and effective masses) predicted by the GALFORM semi-analytic model. In order to calculate the number densities, effective halo masses and satellite fractions, we used HODs of EROs using the semi-analytic model and halo mass functions from Tinker et al. (2010) with equations 5.8, 5.11 and 5.13. The median halo
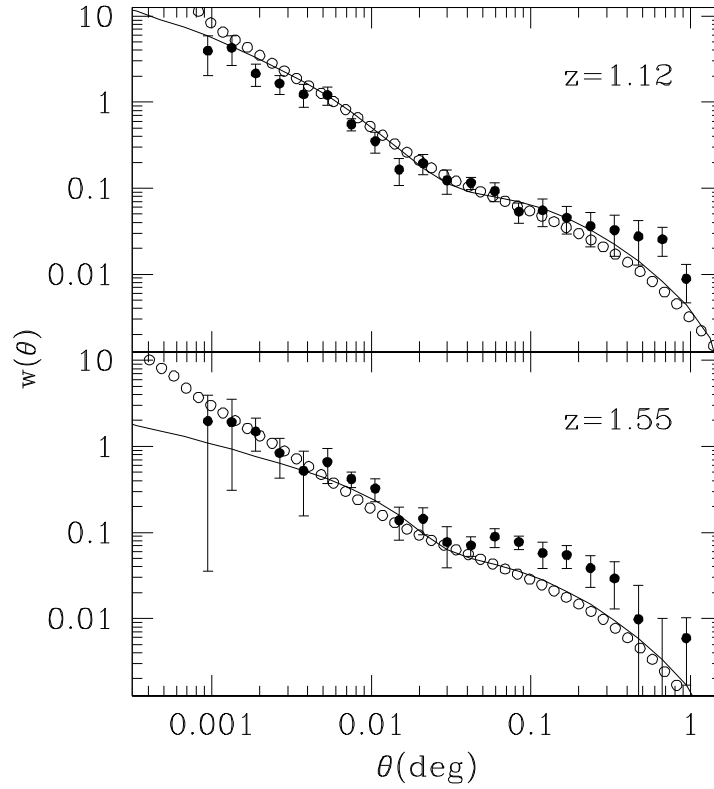
Figure 5.5: Angular correlation functions of M_K cut EROs at different redshifts with GALFORM predictions. Points indicate the observed angular correlation function. Open circles are GALFORM predictions with the observed redshift distribution and the same selection criteria. Solid lines show the best halo model fits for the correlation functions of the GALFORM model.

Table 5.3: Top two rows are correlation lengths, r_0, number densities, dark matter halo masses and satellite fractions predicted from the GALFORM semi-analytic model. Bottom two rows HOD and estimated parameters fitted to both clustering and number density of observed EROs with fixed σ_{cut}, α and GALFORM cosmology. The number density is in units of $10^{-4}h^3\mathrm{Mpc}^{-3}$.

redshift	$r_0(h^{-1}\mathrm{Mpc})$	$\log(median(M_{halo}/M_\odot h^{-1}))$	10 and 90% M_{halo}	n_g	$\log(M_{eff}/M_\odot h^{-1})$	f_{sat}
1.1	7.718	12.572	11.918, 13.523	19.3	13.027	0.22
1.5	6.901	12.320	11.784, 13.199	26.9	12.722	0.22

median z	$\log(M_{cut}/M_\odot h^{-1})$	$\log(M_0/M_\odot h^{-1})$	b_g	$\log(M_{eff}/M_\odot h^{-1})$	f_{sat}	$r_0(h^{-1}\mathrm{Mpc})$	χ^2/dof
1.12	$12.502^{+0.004}_{-0.004}$	$13.830^{+0.031}_{-0.024}$	$2.024^{+0.004}_{-0.010}$	$13.065^{+0.005}_{-0.009}$	$0.120^{+0.006}_{-0.008}$	7.794	2.16
1.55	$12.649^{+0.004}_{-0.004}$	$14.437^{+0.097}_{-0.067}$	$2.705^{+0.004}_{-0.011}$	$13.023^{+0.003}_{-0.007}$	$0.036^{+0.006}_{-0.007}$	9.215	2.71

masses of GALFORM are lower than our effective halo masses in the previous sections, but the M_{eff} of GALFORM shows a similar value to ours, especially for results with a fixed σ_{cut} and α, although different cosmologies were assumed. The GALFORM assumed $\Omega_m =0.25$, $\Omega_\Lambda = 0.75$, $\sigma_8 = 0.9$ and $H_o = 73$ km s^{-1} Mpc^{-1} so σ_8 is 0.1 larger than the value used in our analysis. For direct comparisons, we assumed cosmological parameters again which are the same as the GALFORM model. Then the halo model was generated again to fit to both clustering and number density with a fixed σ_{cut} and satellite HOD slope. The fitted results are listed in Table 5.3 (bottom two rows). Comparing the parameters in Tables 5.2 and 5.3, the overall trends using different cosmology are similar. However the effective masses with GALFORM cosmology are larger than those in the previous section, and the biases are lower. The effective mass from halo modelling with GALFORM cosmology is still higher than the GALFORM median mass, and similar to the effective mass of GALFORM. The correlation length, r_0, is similar at $z = 1.1$, but that from the halo model is larger at $z = 1.5$. This is expected from figure 5.5, since the discrepancy between the two correlation functions on large scales is significant at $z = 1.5$. This discrepancy may also be explained by the satellite fraction, although the HOD of central EROs must reach unity in halo modelling but this is not the case in the semi-analytic model. The direct comparison of HODs is discussed below. The difference in satellite fractions is significantly larger at $z = 1.5$, which means there are less EROs as central galaxies in the semi-analytic model. Therefore the low amplitude of the GALFORM correlation function may be also caused by the fraction of central EROs as well as the possible reasons already mentioned. Here we also note the fraction of EROs to all galaxies in the GALFORM predictions. The fraction of EROs to all galaxies is 0.54 at $z = 1.1$ and 0.74 at $z = 1.5$. In addition those of central EROs to all central galaxies are 0.46 and 0.68 at $z = 1.1$ and 1.5, respectively. In the case of satellites, they are 0.77 and 0.94 in same redshift bins. This indicates that there are many central galaxies bluer than the ERO selection, but these tend to reside in less massive dark matter haloes than those hosting EROs. However the high proportion of EROs as satellites predicted by GALFORM may imply significantly higher satellite fraction than observed.
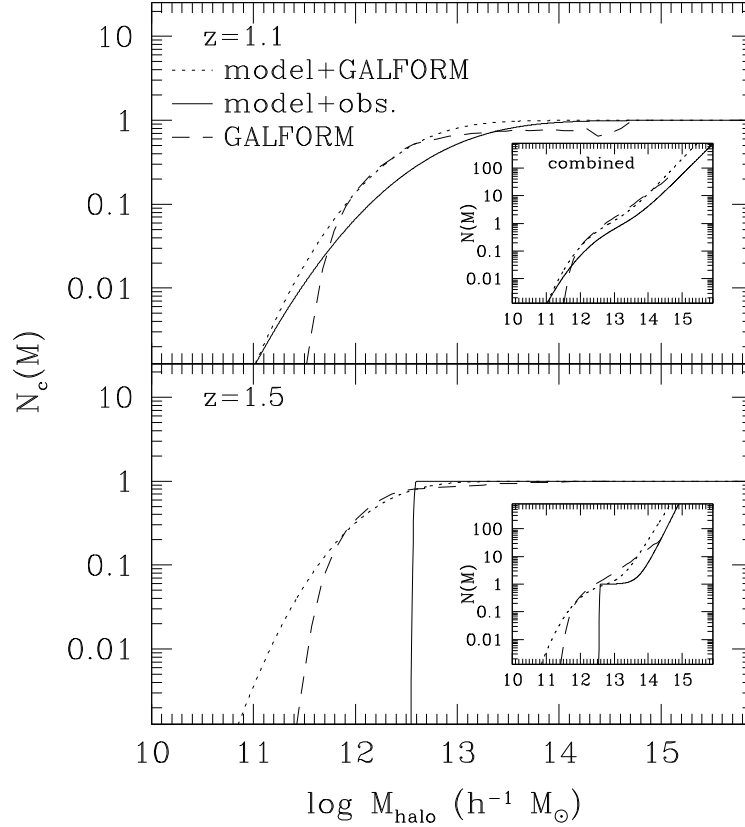
Figure 5.6: Halo occupation distributions of M_K cut EROs at different redshifts. The HODs of central EROs estimated by halo models with three-parameter fit are displayed by solid lines. Dashed lines are HODs of central EROs predicted by GALFORM. Dotted lines are those, when the halo model was fitted to correlation functions predicted by GALFORM. The insets show HODs combined central and satellites EROs with same line styles.

Furthermore GALFORM predicts more EROs overall than observed, especially at $z = 1.5$. The predicted number densities are twice at $z = 1.1$ and 6.7 times at $z = 1.5$ than the observed ones. Comparing number densities of GALFORM EROs with those estimated from fitting halo models to only clustering in section 5.1, they are similar at $z = 1.1$, but show a huge difference at $z = 1.5$. This may also be caused by the large number of satellite EROs in GALFORM.

Figure 5.6 displays HODs of central EROs at different redshifts. Although different cosmological parameters lead to slightly different results, the discrepancy is not large enough to match HODs from the halo model to those from GALFORM.

Therefore we compare HODs from halo modelling in the previous section to GAL-
FORM prediction. HODs of central EROs estimated from halo models with a
three-parameter fit are displayed with solid lines. Dashed lines are the predicted
HODs of central EROs from GALFORM. The insets show HODs combined by
those of central and satellite EROs with same line styles. From HODs in the insets,
the two mass thresholds estimated from halo models are larger than GALFORM
predictions at both redshifts. Since the halo mass function decreases dramatically
in the high halo mass regime, the satellite fractions measured from halo models are
lower than the theoretical prediction. In the case of central EROs, σ_{cut} for EROs at
$z = 1.12$ and 1.55 were 0.9 and 0.01 respectively, which mean a smooth and sharp
HOD shape at each redshift. Gonzalez-Perez et al. (2011) point out that the HOD
of central EROs in GALFORM was below unity for $10^{14}h^{-1}M_{\odot}$ haloes at $z = 1.1$
due to the effect of AGN feedback. It is the same for GALFORM EROs selected by
the criteria used in this work. From the HODs of central EROs, it is noted that halo
masses at $N_c(M) = 0.1$ and 1.0 from GALFORM are $10^{11.92}$ and $10^{14.72}h^{-1}M_{\odot}$ at
$z = 1.1$, respectively. They are $10^{11.73}$ and $10^{14.16}h^{-1}M_{\odot}$ at $z = 1.5$. Therefore the
estimated σ_{cut} from the halo model may describe $N_c(M)$ of GALFORM EROs.

We used functional forms for the HODs calibrated using cosmological simulations
in Zheng et al (2005). In this frame the HOD of central galaxy is forced to reach
unity. However Bower et al. (2006) introduced the effect of AGNs, and these
new simulations now match many observational results well. If the AGN effect is
included, it is not necessary for the central HOD to reach unity. Thus for more
robust comparisons we tried to fit standard halo models to the angular correlation
function predicted by GALFORM. This may provide a direct comparison between
the current HOD frame work and simulations including AGN effects. The solid lines
in figure 5.5 are the best halo model fits for GALFORM correlation functions of
EROs. They show good agreement up to very large scales, although they are not
matched on the smallest scales. The dotted lines in figure 5.6 are central HODs of the
halo model for GALFORM correlation functions at each redshift. They are similar
to those from GALFORM. However they extend to lower halo masses and have
a smoother shape than the GALFORM predictions. Table 5.4 lists halo model

Table 5.4: HOD and estimated parameters fitted to angular correlation functions of GALFORM EROs.

median z	σ_{cut}	$\log(M_{cut}/M_\odot h^{-1})$	$\log(M_0/M_\odot h^{-1})$	α	b_g	$\log(M_{eff}/M_\odot h^{-1})$	f_{sat}
1.12	$0.72^{+0.08}_{-0.15}$	$12.558^{+0.080}_{-0.096}$	$13.201^{+0.013}_{-0.018}$	$1.30^{+0.05}_{-0.05}$	$2.032^{+0.113}_{-0.080}$	$12.978^{+0.058}_{-0.044}$	$0.193^{+0.027}_{-0.017}$
1.55	$0.64^{+0.27}_{-0.46}$	$12.215^{+0.349}_{-0.181}$	$13.206^{+0.022}_{-0.026}$	$2.00^{+0.05}_{-0.08}$	$2.170^{+0.227}_{-0.218}$	$12.691^{+0.091}_{-0.091}$	$0.076^{+0.016}_{-0.016}$

parameters fitted to correlation functions of GALFORM EROs. The effective masses are similar to the GALFORM predictions, and the bias at $z = 1.1$ is similar to observed EROs, but lower at $z = 1.5$. Interestingly the satellite fractions at both redshifts are approximately twice those estimated from observed EROs. At $z = 1.1$ it is similar to the GALFORM prediction. However the fraction is much lower than the GALFORM prediction at $z = 1.5$, which may explain the discrepancy between the angular correlation functions (open circles and solid line) on the very small scales in figure 5.5. Cirasuolo et al. (2010) also reported that various cosmological models still show a wide scatter in the number density of luminous galaxies, especially at high redshift. Also all models predict too many low-luminosity galaxies. This result may be consistent with our analysis.

Comparing all parameters, the possible reasons leading to the discrepancy in the correlation functions is that GALFORM may predict too many EROs, especially satellite EROs at $z = 1.5$, as well as the fundamental possibilities mentioned above. However we also need a more careful analysis to compare halo models with cosmological simulations, since the current HOD frame work forces the shape of HODs which excludes the effect of AGNs.

5.5   Conclusion

In this chapter we have used a near-IR dataset from the UKIDSS DXS and an optical dataset from Pan-STARRS PS1 to investigate the properties of a halo hosting EROs. The main results are summarised as follows;

1. The standard halo model was well fitted to the observed angular correlation of EROs. The biases for EROs range between 1.9 and 3.2, and EROs reside in dark matter haloes more massive than $10^{12.9}h^{-1}M_\odot$. EROs at higher redshift are more biased, and located in more massive dark matter haloes than at lower redshift. Also the satellite fraction decreases with increasing redshift. The different fraction of old, passive EROs at different redshifts may affect the properties as well as evolutionary features in the ΛCDM Universe.

2. The derived results were compared to those for stellar mass limited samples

in previous studies. The properties for EROs are comparable with the NMBS samples in Wake et al. (2011) which are probably lower stellar mass galaxies than EROs. The stellar mass distribution of EROs or cosmic variance may dilute these results. However the overall properties for EROs are consistent with $10^{11.0} M_\odot < M_* < 10^{11.5} M_\odot$ galaxies.

3. The predicted angular correlation function of EROs from the GALFORM semi-analytic model showed good agreement with the observed correlation function, especially on small scales. However they showed a discrepancy on large scales at $z = 1.5$. A difference in number density mainly caused by satellite fractions between the halo model and GALFORM may explain the discrepancy in clustering amplitudes on large scales. Finally we must interpret the results from the HOD frame work with care, since AGNs can alter the shape of HODs.

From this work we have demonstrated that high redshift galaxy populations are important to investigate the distant Universe. However the area and depth surveyed are still not enough to measure the clustering of galaxies accurately. In the near future, the completed UKIDSS and VISTA surveys will allow us to understand the distant Universe. Moreover the combination of near-IR surveys and improved optical surveys such as Pan-STARRS, Hyper Suprime Camera on Subaru and LSST will have a dramatic impact.

Chapter 6

Galaxy clusters in the DXS SA22

6.1 Introduction

Clusters of galaxies are the most important laboratory to study the effect of dense
environments on galaxies and the large scale structure on the Universe. On the
small scale within a galaxy cluster, we can investigate many physical mechanisms
for forming and evolving galaxies. It is well known that red galaxies are concentrated
in the cluster core. In contrast Butcher & Oemler (1978) found that the cores of
galaxy clusters at $z \sim 0.4$ contain a large fraction of blue galaxies, which is different
from galaxy clusters at low redshifts. Similarly Tran et al. (2010) discovered that
the star formation rate of galaxies in the core of a galaxy cluster at $z = 1.62$ was
high which is a reversal of the trend from low redshift environments. Also Edge
et al. (1999) and Edge (2001) found the possibility of star formation in the central
galaxy of cooling flow clusters with the detections of dust and molecular gas. On the
large scale, the distribution of galaxy clusters is tightly linked with the cosmological
model (Gonzalez, Zaritsky & Wechsler 2002; Bahcall et al. 2003; Brodwin et al.
2007 and references therein). Therefore the clustering of galaxy clusters can be used
to test cosmological models.

Many studies have tried to find galaxy clusters since Abell's pioneering work
(Zwicky, Herzog & Wild 1968; Gunn, Hoessel & Oke 1986; Heydon-Dumbleton,
Collins & MacGillivray 1989; Lumsden et al. 1992; Dalton et al. 1997; Annis et
al. 1999; Kim et al. 2002; Gladders & Yee 2005; Wilson et al. 2009). However

finding galaxy clusters has remained a major challenge in astronomy. Especially at high redshift where cluster detections are most difficult due to the lack of deep data and the rareness of massive systems. For the last few decades many optical selection techniques have been developed. Here we briefly describe popular optical selection techniques such as the matched filter, Voronoi Tessellation, maxBCG and red sequence methods.

The matched filter method (Postman et al. 1996) uses luminosity and radial distributions of cluster member galaxies. Comparing both distributions with those of field galaxies, galaxy clusters may show prominently different distributions. Thus spatial and luminosity distributions of cluster galaxies are modelled, and then the matched regions of the observational data are compared. This method gives the redshift and total luminosity of clusters as outputs. However this technique may miss clusters having inconsistent properties with models, since it relies on fixed functions.

From a distribution of particles we can define a characteristic volume associated with each particle which is known as the Voronoi volume. The division of regions is known as Voronoi Tessellation. This technique was applied to find galaxy clusters from the SDSS catalogue (Kim et al. 2002). It does not depend on a source geometry, so it is able to detect irregular structures well. In order to increase a confidence level, density threshold and statistics of Voronoi tessellation for a poissonian distribution are also applied. However Lopes et al. (2004) pointed out that the Voronoi tessellation technique performs better for poor, nearby clusters.

The maxBCG technique (Annis et al. 1999) is based on the colours of elliptical galaxies composing the brightest cluster galaxy (BCG) and the red sequence of cluster. BCGs have a small scatter in magnitude and a photometric evolution with redshift (Stott et al. 2008). The maxBCG method calculates the likelihood that each galaxy is a BCG based on colour and the existence of a red sequence from surrounding galaxies. However this technique does not work well for high redshift clusters, since the cluster galaxy population is more heterogeneous.

Finally the red sequence technique was used by Gladders & Yee (2000). Since elliptical galaxies have similar colours at a given redshift if the 4000 Å break is

positioned between two filters, red galaxies in a galaxy cluster make a clear sequence known as the red sequence. Therefore this sequence is used to detect galaxy clusters. In addition the red sequence is helpful to remove the contamination by blue galaxies at the same redshift, because an elliptical galaxy is the reddest object at a given redshift. From galaxies selected by the red sequence, overdensities of objects are assigned as candidates of galaxy clusters. This technique also provides the redshift of a galaxy cluster based on the red sequence which evolves with redshift.

In this Chapter we perform to search for galaxy clusters in the DXS SA22 field with the red sequence technique. The candidates selected using a red sequence algorithm are compared with spectroscopic datasets. Also the angular clustering of candidate clusters is measured and compared with the prediction of the ΛCDM model. The assumed cosmology is $\Omega_m = 0.3$, $\Omega_\Lambda = 0.7$ and $H_0 = 70$ km s^{-1} Mpc^{-1} in this Chapter. Unless otherwise noted, the AB magnitude system is used in this Chapter.

6.2   Datasets

In order to detect galaxy clusters wide area surveys are necessary, since galaxy clusters are massive and rare systems in the Universe. Recent wide surveys such as UKIDSS, VISTA, CFHTLS and Pan-STARRS provide an opportunity to detect a significant number of galaxy clusters. In this work we concentrated on finding galaxy clusters in the UKIDSS DXS SA22 field with complementary optical datasets.

The DXS maps four different fields covering total 35 deg^2 and the area for each field is 8.75 deg^2. The project is still ongoing and will be completed in 2012. For this work we used the data released in DR5 and DR8 for subfields which were mapped in both J and K filters. All images used for this work were downloaded from the UKIDSS archive, and reprocessed to get a better photometric catalogue with strategies described in Chapter 2.

For complementary optical data we also used the CFHT Legacy Survey[1] (CFHTLS) catalogue obtained by $ugriz$ optical filters. The survey started in 2003 with a 5-

---

[1]http://www.cfht.hawaii.edu/Science/CFHLS/

year plan, and the observations were carried out with the MegaPrime camera on the Canada-France-Hawaii telescope (CFHT). MegaPrime consists of 36 2K×4K CCDs and has a ~1 deg^2 field of view. The survey is composed of four sub-surveys which are the Supernova survey, the wide survey, the very wide survey and the deep survey. Of the four sub-surveys we used the wide survey dataset covering 170 deg^2 with $i_{AB} = 24.5$ depth. The DXS SA22 field overlaps with the CFHTLS W4 field. The CFHTLS W4 maps ~25 deg^2 which is approximately three times wider than the full DXS coverage. Erben et al. (2009) reprocessed the 37 deg^2 CFHTLS wide images released in early 2008 to create photometrically and astrometrically well calibrated images and to get more reliable five-band catalogues. They included ~11 deg^2 of the W4 field covering the whole DXS SA22. We merged the UKIDSS DXS catalogue with that of Erben et al. (2009) for the galaxy cluster detection. The area for the merged catalogue after removing masked regions is ~4.53 deg^2. Also the Galactic extinction was corrected for using the dust map of Schlegel et al. (1998).

The colour of galaxies must be measured from the same parts of galaxies observed with different filters. Since the UKIDSS DXS and CFHTLS wide have similar observational conditions, i.e., similar seeing condition, the colour of objects were estimated using a 2 arcsec aperture magnitude in all filters. In order to remove the contamination by stellar components, the K-band magnitude difference between aperture and total magnitudes was used for bright stars, and the stellar locus on the $g - J$ versus $J - K$ diagram was removed (see Figure 2.10 for the two-colour diagram). Figure 6.1 shows the number density of all galaxies (solid line) and $(i - K) > 2.45$ EROs (dashed line) detected from DXS and CFHTLS. For comparison with previous results, galaxy number counts in Lane et al. (cyan, 2007) and those for galaxy (top) and EROs (bottom) in Kong et al. (blue and red, 2006) are also displayed. The number densities of galaxies and EROs from the DXS/CFHTLS catalogue are consistent with previous results.

Photometric redshifts of galaxies can be used as a constraint to find galaxy clusters. In this work the red sequence technique is applied to find clusters. But it can not avoid contamination by blue galaxies at higher redshifts. Therefore the photometric redshift can be used to reduce the contamination. From the DXS/CFHTLS
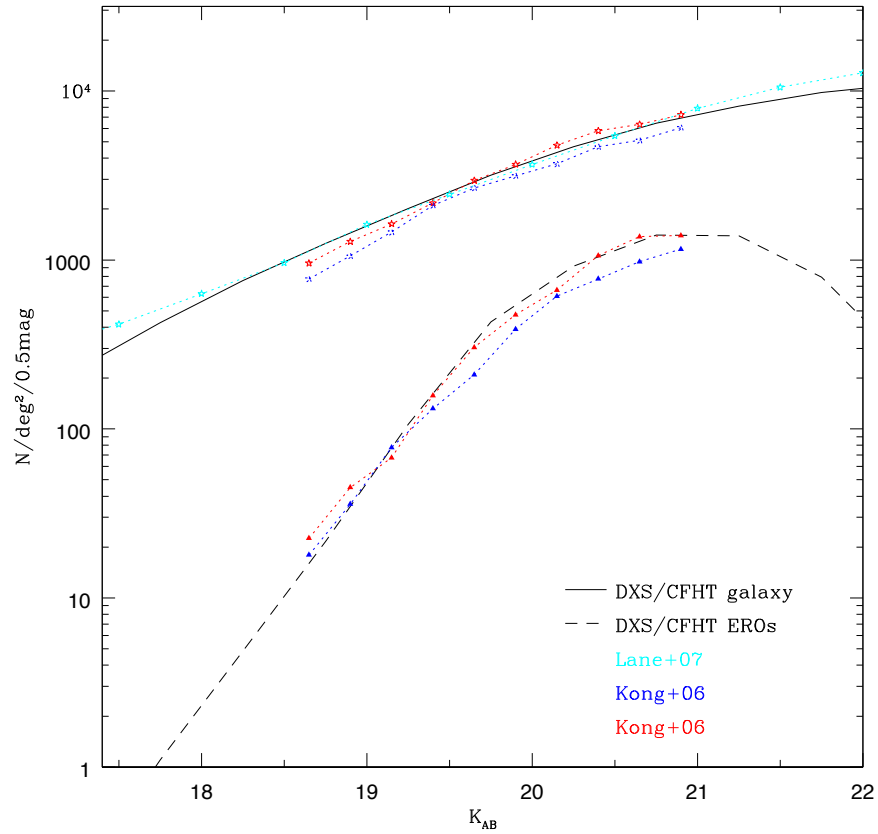
Figure 6.1: Number counts of galaxies (solid line) and EROs (dashed line) in SA22 field by DXS/CFHTLS. For the comparison, galaxy number counts (top) by Lane et al. (cyan, 2007) and Kong et al. (blue and red, 2006) are displayed. In addition those for EROs (bottom blue and red) in Kong et al. (2006) are also shown.

catalogue the photometric redshifts of galaxies were measured by the EAZY (Brammer et al. 2008). Firstly the photometric catalogue was matched with the VIMOS VLT Deep Survey (VVDS) spectroscopic catalogue (Le Févre et al. 2005). Then the EAZY code was run with spectroscopic redshifts for only matched objects to measure the zero magnitude offsets of each filter compared with the best template at the spectroscopic redshift. Finally the photometric redshifts for all galaxies were estimated after correcting for the zero magnitude offset. The normalised median absolute deviation in $\Delta z/(1 + z_{spec})$ was 0.05.

6.3   Algorithm

We apply the red sequence technique to find galaxy clusters in DXS fields. In this section the algorithm applied to find galaxy cluster candidates is described.

Swinbank et al. (2007) found the supercluster at $z = 0.9$ in Elais-N1 field from the UKIDSS DXS early data release (EDR) covering just $\sim$0.8 deg^2. The main goal of this work is to check for the existence of other superclusters in other fields as well as finding galaxy clusters. We applied the red sequence method with additional constraints for galaxy clusters at $0.8 < z < 1.2$ where the $r - J$ colour can efficiently distinguish red galaxies from other populations.

First, the colour-magnitude relations of red sequences at various redshifts were generated by using the GALAXEV (Bruzual & Charlot 2003). We assumed the formation redshift of galaxies as $z_f = 5$ with the metallicity range from $Z = 0.004$ to 0.05 and the Salpeter initial mass function. Also the models were constructed with half of the stars formed in a single burst at $t = 0$ and the remainder formed with an exponentially declining formation rate of $\tau = 0.1$ Gyr. These assumptions were also applied in Muzzin et al. (2008) which detected galaxy clusters successfully. Muzzin et al. (2008) noted that the red sequence modelled with $z_f = 2.8$ and 5.0 were identical at $z < 1.1$. Our main targets are galaxy clusters at $z \sim 1$, so $z_f = 5$ should be appropriate for this work. Finally the red sequences generated were calibrated to that of the Coma cluster in Bower et al. (1992). Figure 6.2 shows the modelled red sequences at different redshifts. The points correspond to colour and magnitude at
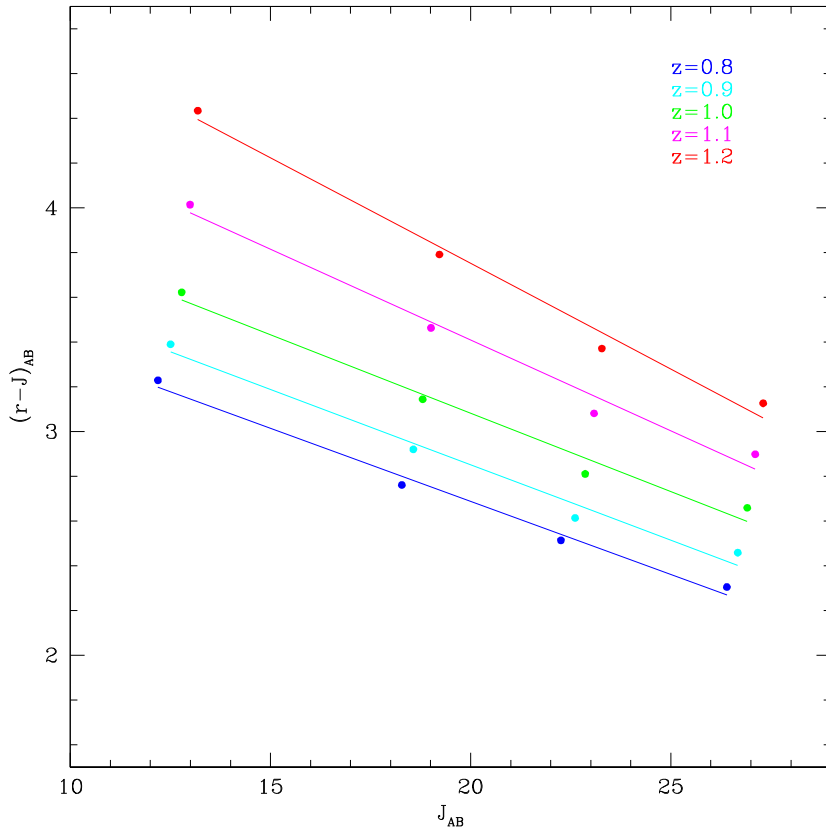
Figure 6.2: Modelled red sequences from $z = 0.8$ to $z = 1.2$ on $r - J$ vs. J plane. Points correspond to colour and magnitude with various metallicities. Solid lines show the least squares fits.

each metallicity and the solid lines show the least squares fits.

Second, galaxies satisfying the red sequence criteria were extracted from the DXS/CFHTLS catalogue. We applied bins to the redshifts derived from the red sequence fitting of $\Delta z = 0.1$ from $z = 0.8$ to $z = 1.2$ with increasing boundaries as 0.05, i.e., $0.8 < z < 0.9$, $0.85 < z < 0.95$, ..., $1.05 < z < 1.15$ and $1.1 < z < 1.2$. Simultaneously the photometric redshift constraint was also applied. A wider photometric redshift width of 0.05 than the redshift boundaries for the red sequence fits was applied due to the uncertainty in the photometric redshifts. Since the samples selected by red sequence colours contain few lower redshift galaxies, the photometric redshift constraint is most useful to remove galaxies at higher redshifts.

Finally, a contour map of selected galaxies was created and overdense regions

were selected as cluster candidates. The observed area was gridded with a 12.6 arcsec bin width, and the number of red sequence galaxies in each bin was assigned as a value in a grid point. Then the gridded map was filtered with the Gaussian filter of 0.8 arcmin FWHM corresponding to 350 kpc at $z = 0.8$ and 390 kpc at $z = 1.2$. When the filtered pixel had a value of $> 4\sigma$, where σ is the standard deviation of filtered pixels, this region was assigned as the candidate of galaxy cluster. The coordinate of cluster candidates was determined by the position of the peak pixel, and the redshift of candidates was assigned the median redshift of galaxies satisfying photometric redshift criteria within a 2.28 arcmin radius.

6.4   Cluster Candidates

Through the algorithm described in the previous section we can find candidate galaxy clusters in UKIDSS DXS fields. The algorithm was applied most successfully to the DXS/CFHTLS catalogue of the DXS SA22 field. But the process was also applied to the DXS/PS1 catalogue used in previous chapters for the DXS Elais-N1 field to detect galaxy clusters at $z \sim 0.9$ published in Swinbank et al. (2007) as a test of our technique.

6.4.1   Reliability of the algorithm

From the UKIDSS EDR dataset covering ~ 0.8 deg^2, Swinbank et al. (2007) already found five galaxy clusters in this field and suggested the existence of supercluster at $z \sim 0.9$. They applied wider colour bins than the modelled red sequences here and fixed the red sequence slope as -0.025 in the colour magnitude space. However they used $J-K$, $I-K$ and $K-3.6\mu$m colours and identified galaxy overdensities detected by all colours. Those are good testbeds to check the reliability of the algorithm and to find other candidates included in the supercluster.

Figure 6.3 shows contour maps for galaxy cluster candidates identified from the DXS/PS1 catalogue. Since the released J-band coverage was smaller than the optical data, the south-east part of the figure was not included in the analysis. Contour levels range from 3σ to 7σ with a 1σ increment above the mean density of the back-
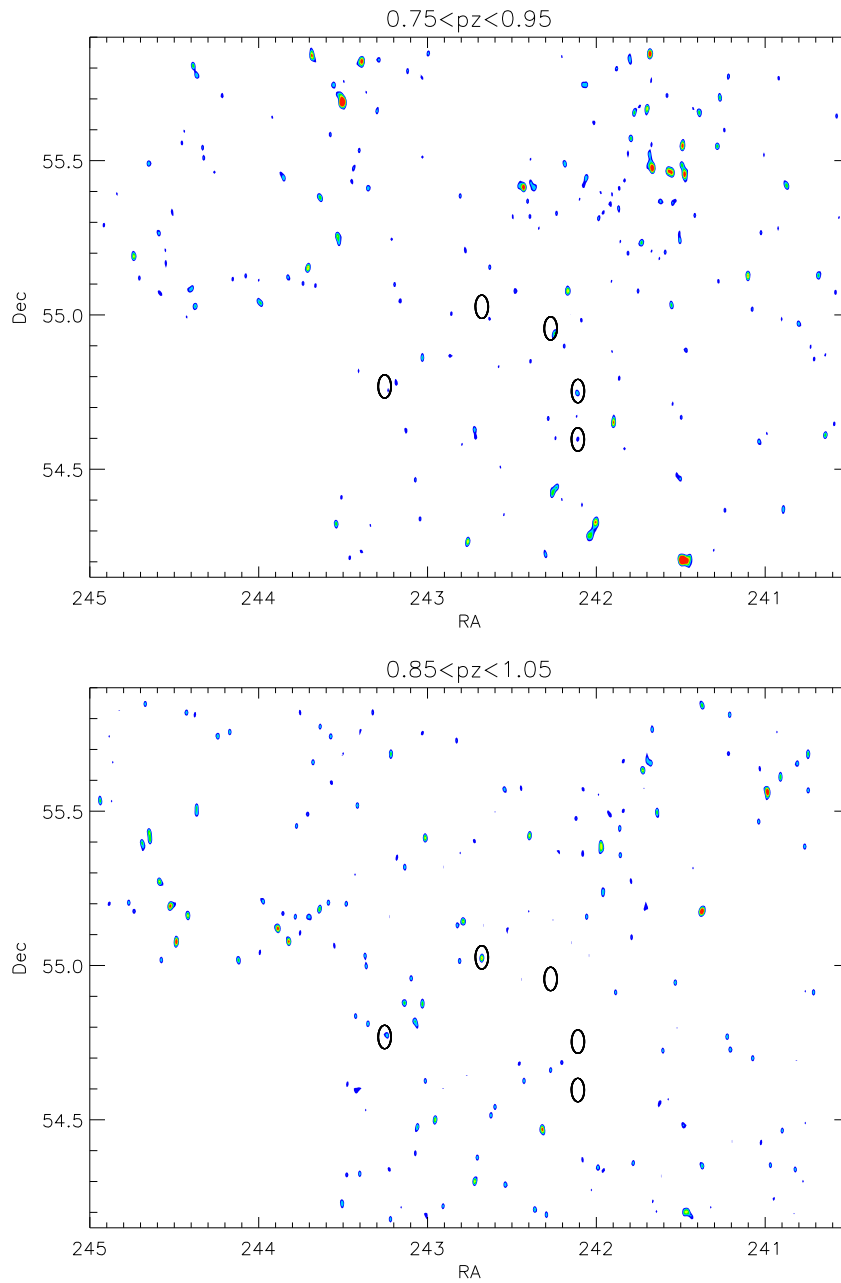
Figure 6.3: Contour maps for galaxy cluster candidates in Elais-N1 at $0.8 < z < 0.9$ (top) and $0.9 < z < 1.0$ (bottom). Contour levels are 3 (blue), 4 (cyan), 5 (green), 6 (yellow) and 7σ (red) from the mean density of background. Black circles indicate galaxy clusters published in Swinbank et al. (2007).

ground. Black circles indicate the five galaxy clusters confirmed spectroscopically in Swinbank et al. (2007) with a 2.28 arcmin radius corresponding to 1 Mpc at $z = 0.9$. Although two of them are detected at slightly shifted regions, all confirmed clusters are detected by our algorithm within a 1 Mpc range. Therefore we can conclude that the red sequences are modelled correctly and the algorithm works properly.

Moreover we can find other candidates across the whole area. Swinbank et al. (2007) pointed out that they detected the only part of supercluster and possibly missed up to 50 per cent. From the contour maps, there are significant overdense regions on the north-west part and some candidates between confirmed clusters. We also note that prominent candidates between confirmed clusters in this work are identical with those in Swinbank et al. (2007). Thus more spectroscopic confirmation is required for this field.

6.4.2   Candidates in SA22

The algorithm was also applied to the DXS/CFHTLS catalogue. The catalogue covers $\sim$4.53 deg^2 with $ugrizJK$ filters. The wide area is vital to find galaxy clusters at different redshifts. In this work we mainly focus on finding cluster candidates at $0.8 < z < 1.1$.

Firstly we measured angular correlation function of the extracted red sequence galaxies, since if the algorithm selects suitable galaxies in red sequences those should be strongly clustered. Figure 6.4 shows angular correlation function of selected galaxies at each redshift bin. The red line shows the angular correlation function of EROs by the DXS/Subaru catalogue with $(I - K)_{AB} > 2.55$ and $K_{AB} < 20.7$ in Chapter 4. The uncertainty of correlation function was calculated using the poissonian variance with equation 3.2. The purpose of this analysis is to check whether they are strongly clustered or not. Thus the integral constraint correction was not applied. All the correlation functions at each redshift bin show a high amplitude, and a clear break at $\theta \sim 1.2'$ from the two components contributed by the same halo and different haloes. It is also noted that the amplitude is comparable with that of EROs in Chapter 4, especially at $z > 0.9$. Since EROs are distributed at a similar redshift range as the target redshift for cluster finding, most red sequence
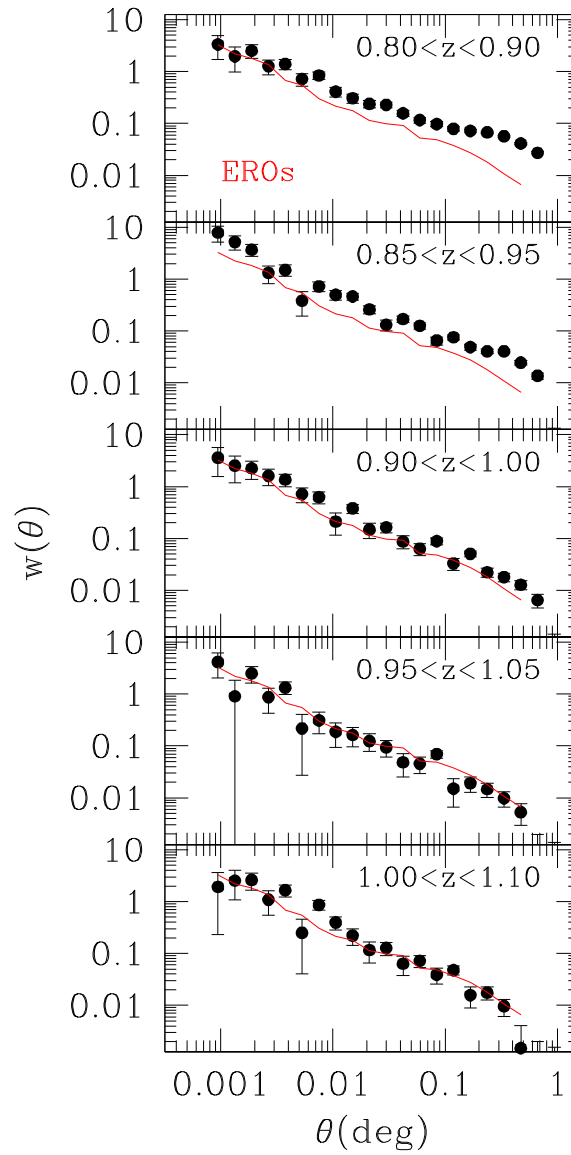
Figure 6.4: Angular correlation functions of red sequence galaxies at different redshift bins. Points indicate the angular correlation functions of red sequence galaxies. The red line shows that of EROs by the DXS/Subaru catalogue with $(I - K)_{AB} > 2.55$ and $K_{AB} < 20.7$.

galaxies in those redshift bins may overlap with EROs. However EROs may miss a large fraction of red galaxies at $z < 0.9$ because of the selection criterion for EROs. From the angular correlation function it can be concluded that the algorithm extracts suitable red sequence galaxies to find galaxy clusters.

Figure 6.5, 6.6 and 6.7 show contour maps of selected red sequence galaxies for galaxy cluster candidates in the DXS SA22 field in different redshift bins. The south-east and north-west parts are empty due to the lack of J-band coverage. Contour levels range from 3σ to 7σ with a 1σ increment above the mean density of background. From these contour maps we can find many overdense regions and different large scale structures at each redshift bin. It is also identified that significantly overdense regions corresponding to richer cluster candidates are concentrated on a particular area, i.e., are more clustered. Figure 6.8 and 6.9 show examples of galaxy cluster candidates at $0.8 < z < 0.9$ and $1.0 < z < 1.1$ respectively. The top-left panel shows the fraction of the galaxies satisfying photometric redshift ranges compared to the total number of galaxies as a function of redshift. Top-right and bottom-right panels display two different colour-magnitude diagrams of galaxies within a 1 Mpc projected radius. Small points are all galaxies, red points are galaxies satisfying photometric redshift criteria, and green points are red sequence galaxies. Cyan lines indicate the red sequence boundaries. For the plot, slightly wider red sequence boundaries, each sequence was moved 0.1 dex on the colour space, were applied to consider the uncertainty of colour. The bottom-left panel shows the spatial distribution of galaxies with the same colours as in the colour-magnitude diagrams. Both candidates show a clear red sequence in different colour-magnitude spaces. In addition, red sequence galaxies are centrally concentrated making them clear candidates for rich clusters.

The number density of cluster candidates was 19 deg^{-2} in Swinbank et al. (2007). Through the algorithm we found 124 overdense regions at $0.8 < z < 0.9$ corresponded to 27.4 deg^{-2}. It is a significantly larger number, compared with the result in Swinbank et al. (2007). The algorithm might find many groups or noise due to small number statistics. If we apply another constraint on the number of galaxies satisfying the red sequence boundaries, N_{RS}, as more than 10, 13 and 15, these
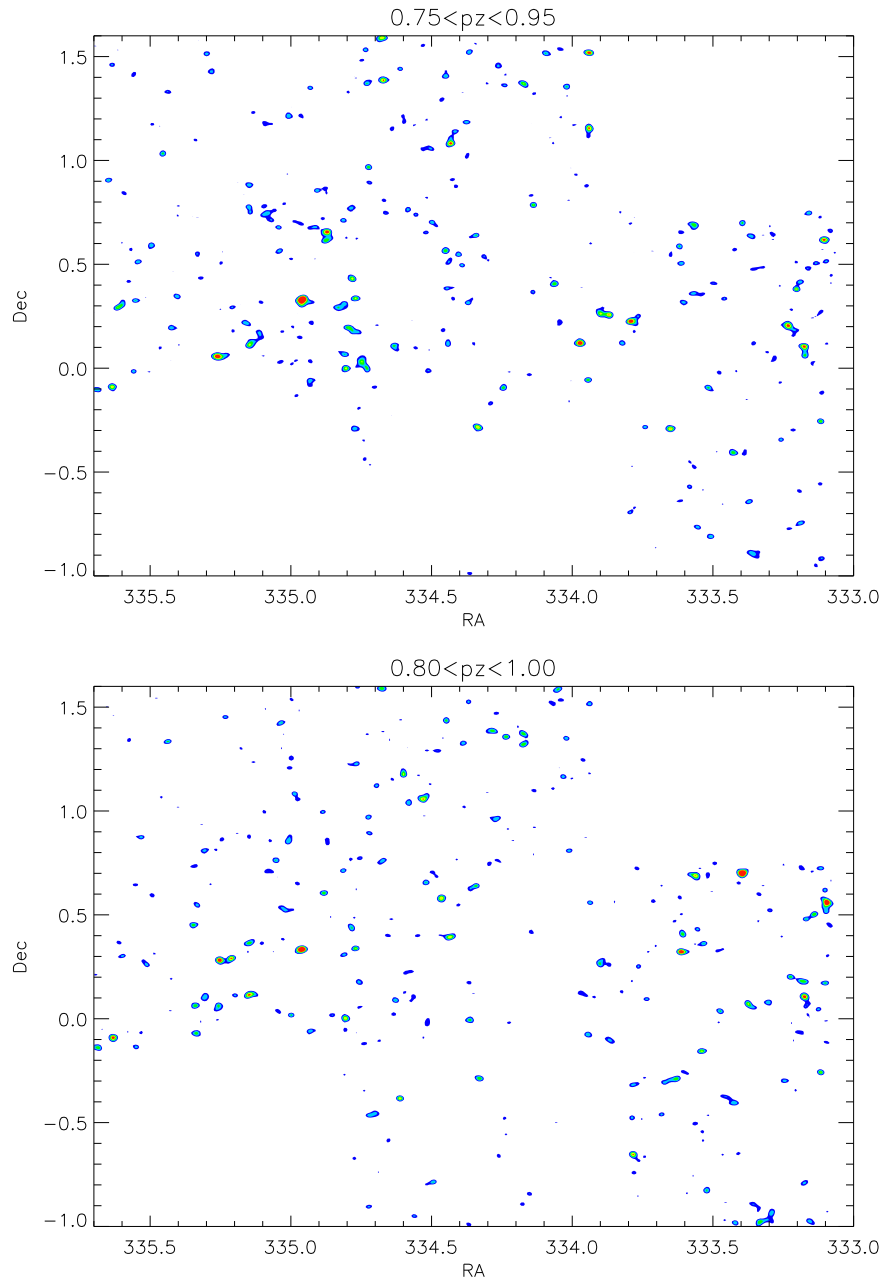
Figure 6.5: Contour maps for galaxy cluster candidates in SA22 at $0.8 < z < 0.9$ (top) and $0.85 < z < 0.95$ (bottom). Contour levels are 3 (blue), 4 (cyan), 5 (green), 6 (yellow) and 7σ (red) from the mean density of background. The term pz at the top of panel denotes photometric redshift.
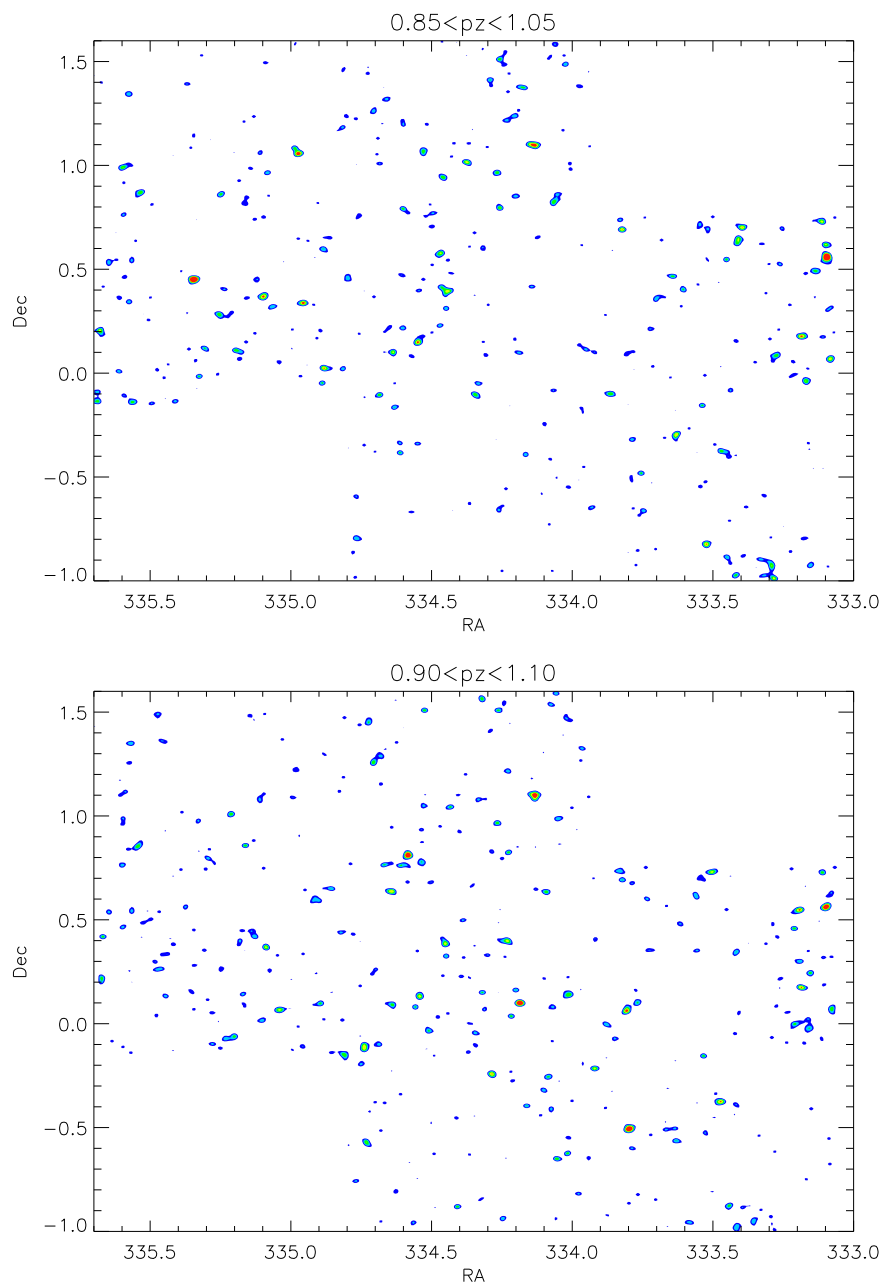
Figure 6.6: Same with Figure 6.4 but cluster candidates at $0.9 < z < 1.0$ (top) and $0.95 < z < 1.05$ (bottom).
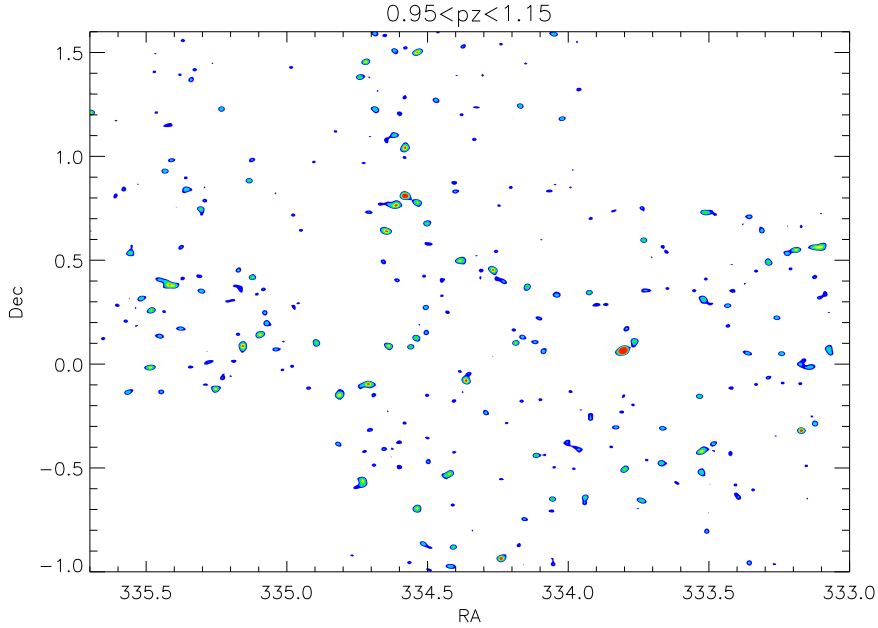
Figure 6.7: Same with Figure 6.4 but cluster candidates at $1.0 < z < 1.1$.

surface densities become 14.6, 7.5 and 4.0 deg^{-2}, respectively, which are more reasonable values. Additionally, the measured surface densities of cluster candidates with $N_{RS} \geq 8, 10$ and 13 at $0.8 < z < 1.1$ are 50.8, 27.6 and 10.6 deg^{-2}. Gladders & Yee (2005) found 429 candidates of clusters and groups at $0.9 < z < 1.4$ from $\sim$10 deg^2 of the Red sequence Cluster Survey (RCS). They also confirmed 67 clusters from these 429 candidates. Thus our identified candidates in this work show slightly higher densities than Gladders & Yee (2005). However van Breukelen et al. (2006) found 13 clusters (26 deg^{-2}) having $5 \times 10^{13} < M_{cluster} < 3 \times 10^{14}$ at $0.61 < z < 1.39$ from the UKIDSS UDS EDR data. They also measured the number density as 10 deg^{-2} for $> 10^{14} M_{\odot}$ clusters at $z = 0.5 - 1.5$. These results show good agreement with this work.

6.4.3 Spectroscopic confirmations

In order to confirm candidates as galaxy clusters, spectroscopic follow-up observations are necessary. We have spectroscopic datasets which can confirm galaxy clusters from our selected candidates. Thus cross-matching candidate clusters with spectroscopic datasets is described in this section.
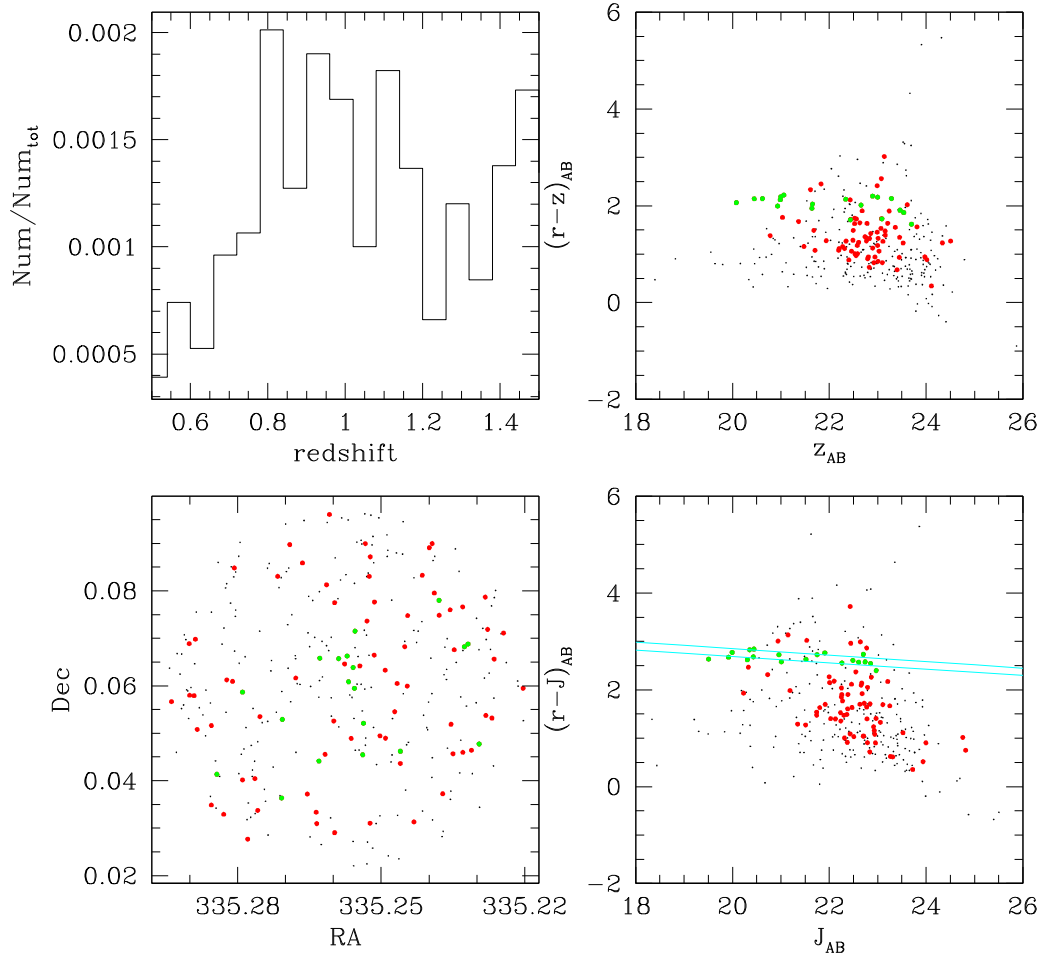
Figure 6.8: Example of galaxy cluster candidate at $0.8 < z < 0.9$. The top-left panel shows the fraction of number of galaxy satisfying photometric redshift ranges to total number of galaxy. Top-right and bottom right panels display $(r - z)_{AB}$ vs. z_{AB} and $(r - J)_{AB}$ vs. J_{AB} diagrams of galaxies within 1 Mpc radius, respectively. Small points are all galaxies, red points are galaxies satisfying photometric redshift ranges, and green points are red sequence galaxies with a slightly wider colour criterion. Cyan lines indicate red sequence boundaries. The bottom-left panel shows the spatial distribution of the galaxies with same symbols as in the colour magnitude diagrams.
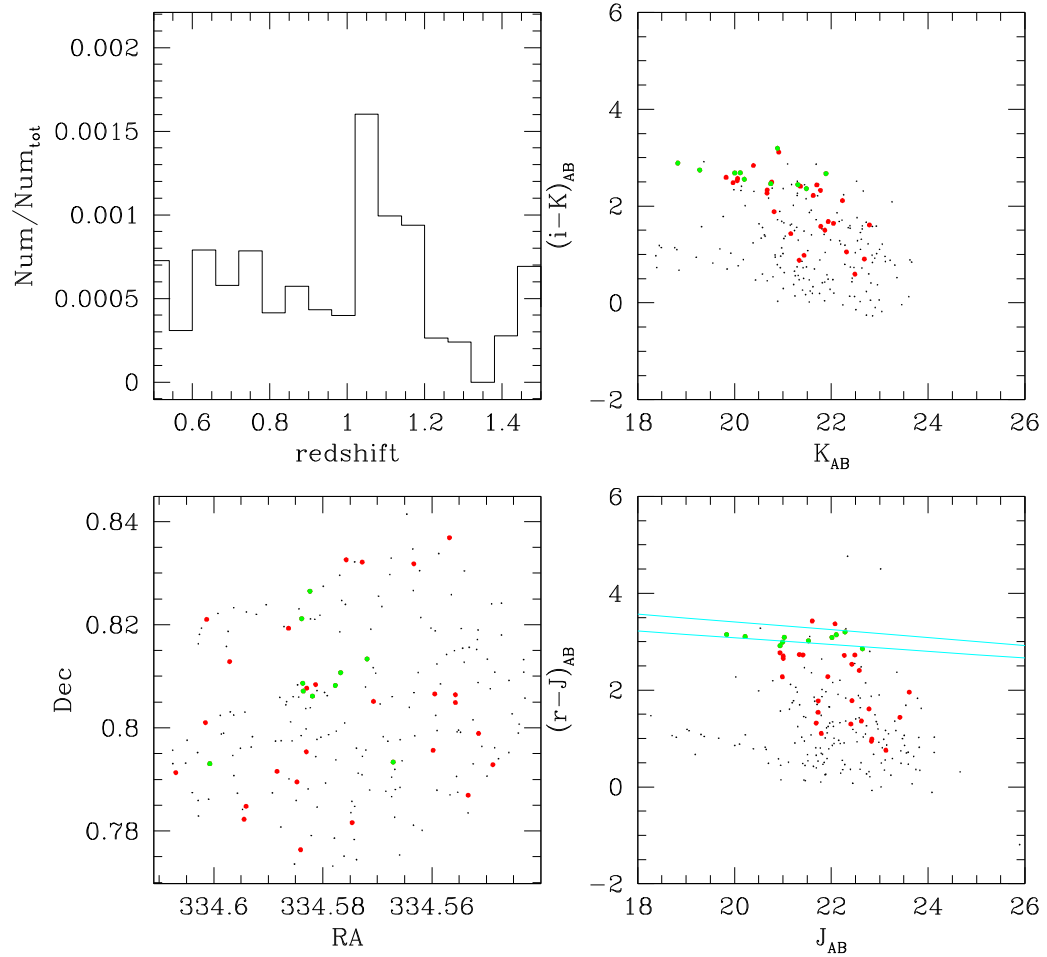
Figure 6.9: The same plot with figure 6.8, but candidate at $1.0 < z < 1.1$. Also $(i - K)_{AB}$ vs. K_{AB} diagram is displayed in the top-right panel.

The purpose of these observations was to confirm galaxy clusters selected from the UKIDSS DXS DR2 dataset with the i-band catalogue obtained from the CTIO Blanco telescope. In John Stott's PhD thesis he tried to find candidate galaxy clusters. Instead of using the red sequence slope, he applied $3.6 < (i - K)_{vega} < 4.9$ and $1.6 < (J - K)_{vega} < 2.0$ criteria based on the typical colours of the brightest cluster galaxy at $z \sim 1$. He measured the number density of candidates as 9 deg^{-2} comparable with 14.6 and 7.5 deg^{-2} for candidates of $N_{RS} \geq 10$ and 13 at $0.8 < z < 0.9$ in this work. It also gives an opportunity to check the reliability of the algorithm in this work.

The spectroscopic observation was performed by the Gemini Multi-Object Spectrograph (GMOS) mounted on the Gemini North telescope in 2007. The GMOS provides multi-slit spectroscopy with $\sim$30 slits and imaging over a 5 arcmin field of view. Galaxies at high redshift are faint, so good sky subtraction and removal of night sky lines is required. The observation with the Nod and Shuffle sky subtraction method (Glazebrook & Bland-Hawthorn 2001) was performed. The GMOS OG515 filter with the R400 grating was used for the observation covering 580-1100 nm. The redshifts of galaxies were determined by the identification of emission or absorption features, principally the [OII] 3727Å, 4000Å break, Ca H&K absorption at 3933Å, 3969Å and G-band at 4304Å. This analysis was performed by John Stott.

From the spectroscopic observations there are three galaxy clusters (preliminarily named as SA22DXS2, SA22DXS5 and SA22DXS7) at $z \sim 0.87$. Cross-matching them with selected candidates in this work, two clusters (SA22DXS2 at $\alpha = 334.4458, \delta = 0.1161$ and SA22DXS7 at $\alpha = 335.1375, \delta = 0.1156$) were also detected by the algorithm, but one cluster (SA22DXS5 at $\alpha = 335.0083, \delta = 0.2139$) was detected at the $> 3\sigma$ level. In this work we concentrated on two prominent clusters. The number of member galaxies confirmed spectroscopically were 4 and 9 for SA22DXS2 and SA22DXS7 respectively. Figures 6.10 and 6.11 show properties of confirmed clusters, SA22DXS2 and SA22DXS7, with the same symbols as Figure 6.8. Blue open circles are spectroscopically confirmed member galaxies. The spectroscopic redshifts of SA22DXS2 and SA22DXS7 are 0.872 and 0.875 respectively, and the photometric redshifts estimated by the median values of galaxies are 0.838
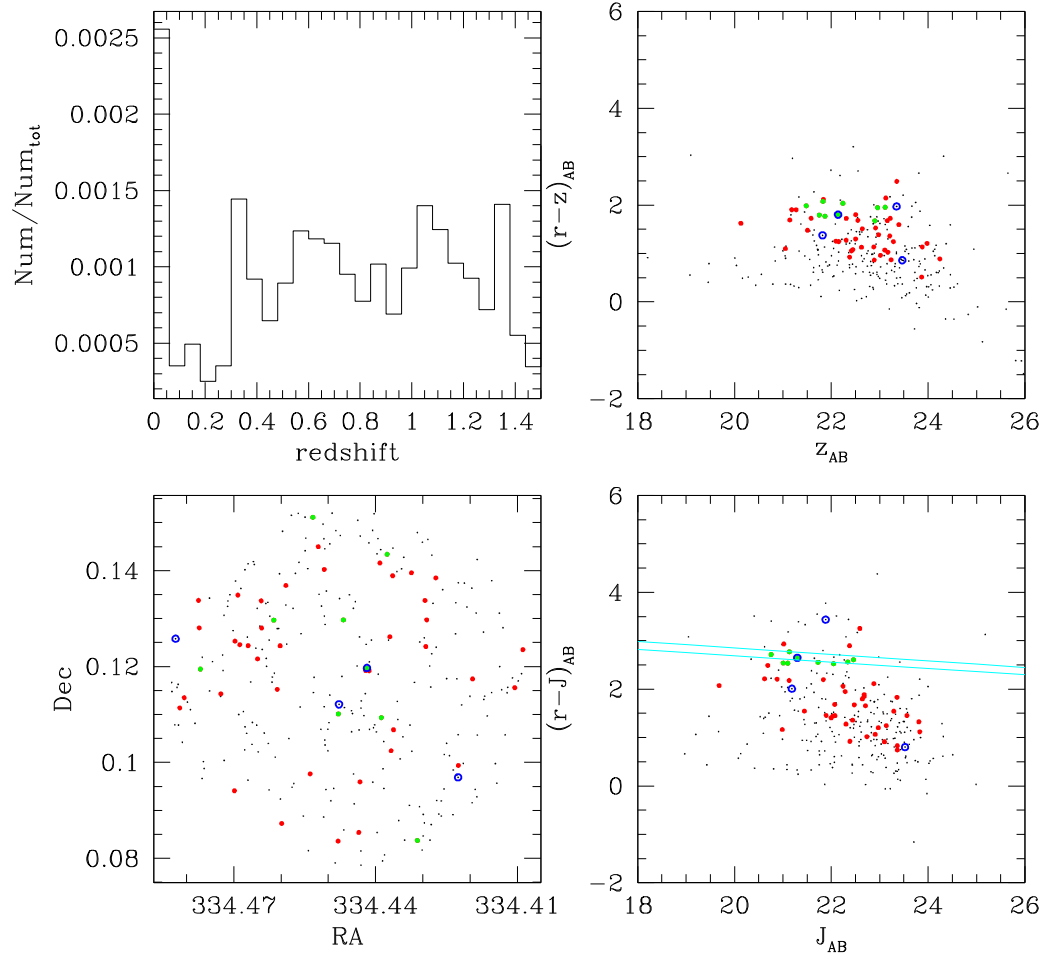
Figure 6.10: The spectroscopically confirmed galaxy cluster SA22DXS2. Symbols are the same as figure 6.8. Blue open circles indicate member galaxies confirmed spectroscopically.
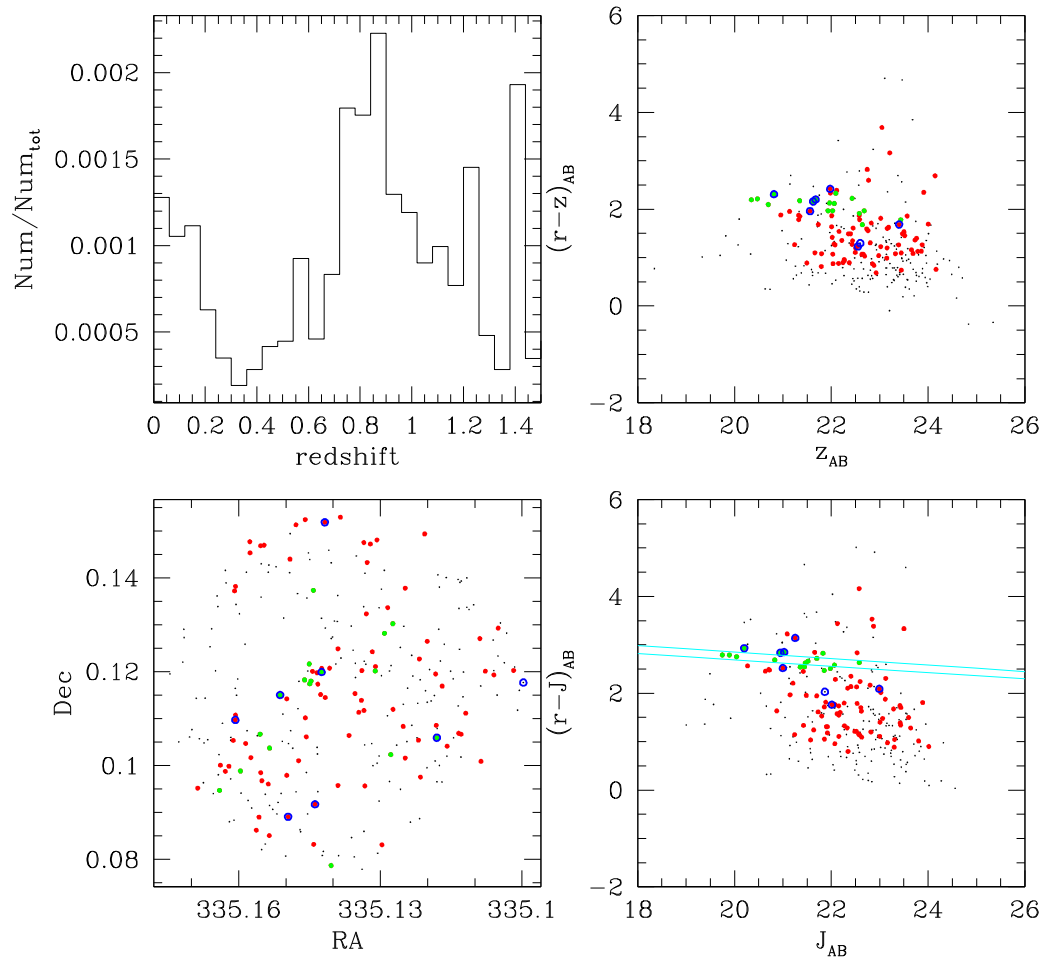
Figure 6.11: The spectroscopically confirmed galaxy cluster SA22DXS7. Symbols are the same as figure 6.10.

and 0.837. The spectroscopic redshifts of clusters were measured using the bi-weight mean in Beers, Flynn & Gebhardt (1990). Although the photometric redshifts are slightly lower than the spectroscopic redshifts within the uncertainty range, it is confirmed that both clusters are located at the same redshift. The angular distance between them is 0.69 deg corresponding to 19.2 Mpc at $z = 0.87$.

The robust approach by Beers et al. (1990) also allows us to calculate the scale corresponding to the dispersion in redshift (σ_z) and to identify members of clusters as well as the mean for the central redshift (z_c). From both quantities, the line of sight rest-frame velocity dispersion (σ_v) is calculated by

$$\sigma_v = \frac{\sigma_z c}{1 + z_c}, \tag{6.1}$$

where c is the speed of light (Demarco et al. 2010). The velocity dispersions for SA22DXS2 and SA22DXS7 are 589 ± 183 km s^{-1} and 1130 ± 226 km s^{-1} respectively. The errors were estimated by the bootstrap resampling method.

The dynamical properties of galaxy clusters can be described with r_{200}, the radius at which the mean interior density is 200 times critical density, and M_{200}, the mass within r_{200} (Carlberg et al. 1997). Those are estimated with the velocity dispersion by

$$r_{200} = \frac{\sqrt{3}\sigma_v}{10H(z)}, \tag{6.2}$$

$$M_{200} = 3\frac{\sigma_v^2 r_{200}}{G}, \tag{6.3}$$

where $H(z)$ is the Hubble parameter, and G is the gravitational constant. Based on velocity dispersions, we estimated $r_{200} = 0.89 \pm 0.28$ Mpc and 1.71 ± 0.34 Mpc for SA22DXS2 and SA22DXS7 and $M_{200} = 2.1\pm1.4\times10^{14}M_\odot$ and $1.7\pm0.6\times10^{15}M_\odot$ for the two clusters, respectively. Although an accurate estimation is prevented by the small number of redshifts, the SA22DXS7 may be one of the most massive clusters detected at $z > 0.8$. We note that Hoekstra et al. (2000) found a $2.4\times10^{15}M_\odot$ cluster and Demarco et al. (2010) reported SpARCS J161315+564930 having $2 \times 10^{15}M_\odot$. Thus SA22DXS7 may not be a unique system, but a rare system. From the algorithm in this work, N_{RS} values for SA22DXS2 and SA22DXS7 were 7 and 18 respectively.

6.4.4 Supercluster candidate

A supercluster is an association of galaxy groups and galaxy clusters extending across tens of Mpc. Examples of discovered distant superclusters are the Lynx Supercluster at $z = 1.26$ (Rosati et al. 1999), the supercluster at $z \sim 1.1$ in the 1338+27 field (Tanaka et al. 2001), the CI1604 supercluster and the supercluster in Elais-N1 (Swinbank et al. 2007). From the DXS/CFHTLS catalogue we can check the presence of such a supercluster.

Figure 6.12 shows the spatial distribution of candidate clusters at $0.8 < z < 0.9$ with $N_{RS} \geq 10, 13$ and 15 (black, red and cyan points respectively). It is clear that the distribution of candidates is not homogeneous, but clustered. There are fewer candidates on the southern part $333.6 < \alpha < 334.6$ and $-1 < \delta < 0$, although the catalogue covers this area. The candidates having $N_{RS} \geq 10$ (black points) are distributed across whole area. However $N_{RS} \geq 15$ candidates are concentrated on the eastern part of area. Furthermore black open circles indicate SA22DXS2 and SA22DXS7 which are confirmed by the spectroscopic observation. We can also find more candidates between and around them. From confirmed clusters and candidates having higher N_{RS}, it may suggest the presence of a supercluster in the DXS SA22 field.

Figure 6.13 is the photometric redshift distribution of candidates satisfying the three N_{RS} criteria with the same colour coding in Figure 6.12. Interestingly most $N_{RS} \geq 15$ candidates are located at $z \sim 0.83$ with approximately a Gaussian distribution. The dashed line shows the Gaussian fit for candidates at $0.815 < z_{phot} < 0.845$. The fit suggests $z = 0.829$ and $\sigma = 0.007$. Finally Figure 6.14 displays $(r - J)_{AB}$ versus J_{AB} diagrams for 18 candidates having $N_{RS} \geq 15$. Symbols are the same as Figure 6.8. We find many red sequence galaxies which are brighter than the foreground blue galaxies. Additionally the magnitude of the brightest cluster galaxy can be used to check the reliability of the algorithm and candidates as galaxy clusters. Stott et al. (2008) presented the magnitude and colour evolution of BCGs in the near-IR regime. From their results we can expect $J_{AB} \sim 20$ as the magnitude of a BCG at $z \sim 0.8$. From Figure 6.14, the J-band magnitudes of the brightest red sequence galaxies which should be identical to BCGs are consistent with those
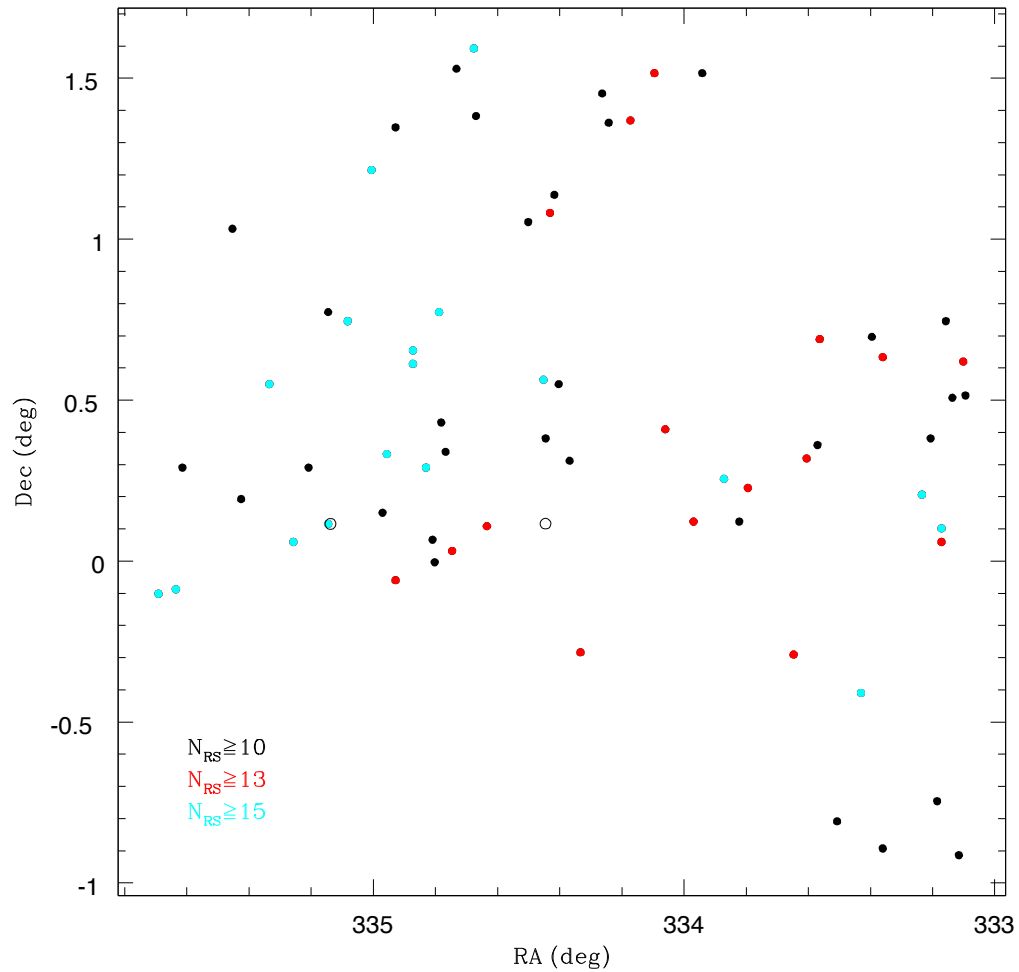
Figure 6.12: The spatial distributions of candidate clusters with $N_{RS} = 10, 13$ and 15 (black, red and cyan points respectively). Open black circles indicate SA22DXS2 ($\alpha = 334.4458$ and $\delta = 0.1161$) and SA22DXS7 ($\alpha = 335.1375$ and $\delta = 0.1156$).
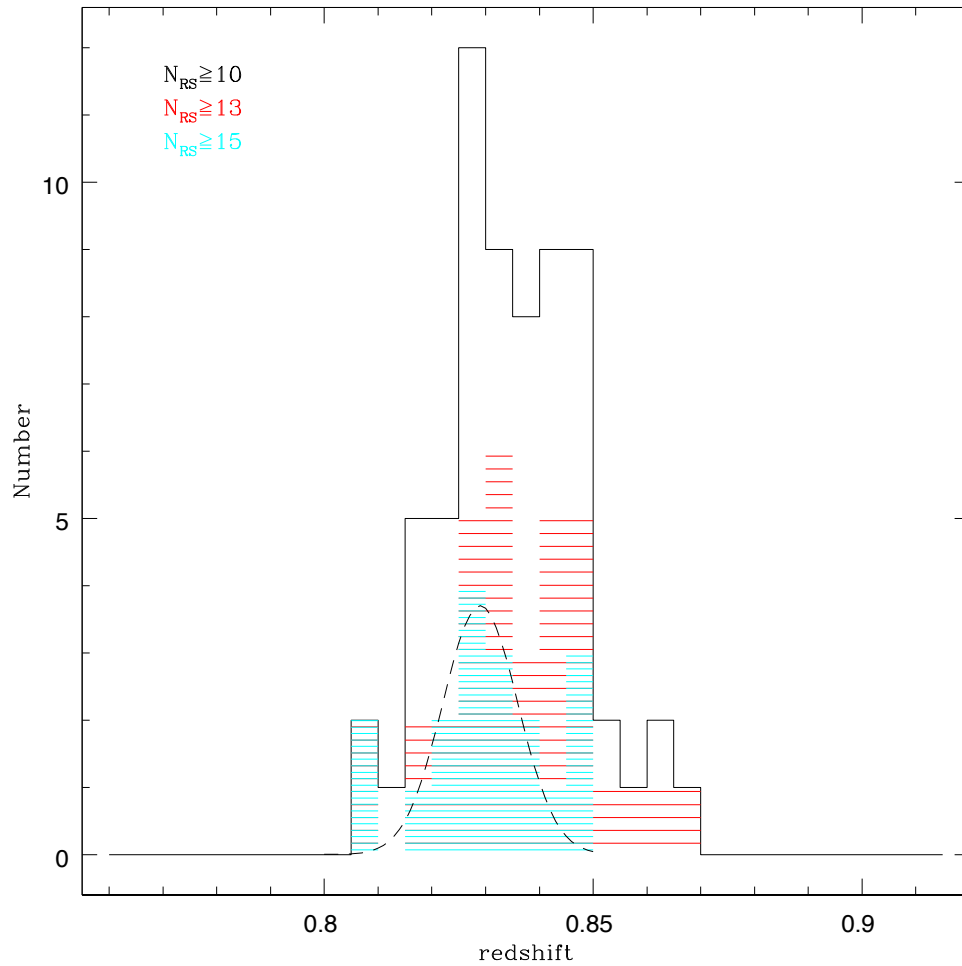
Figure 6.13: The Photometric redshift distribution of massive cluster candidates displayed in Figure 6.12 with the same colour coding. The dashed line shows the Gaussian fit for candidates at $0.815 < z_{phot} < 0.845$.
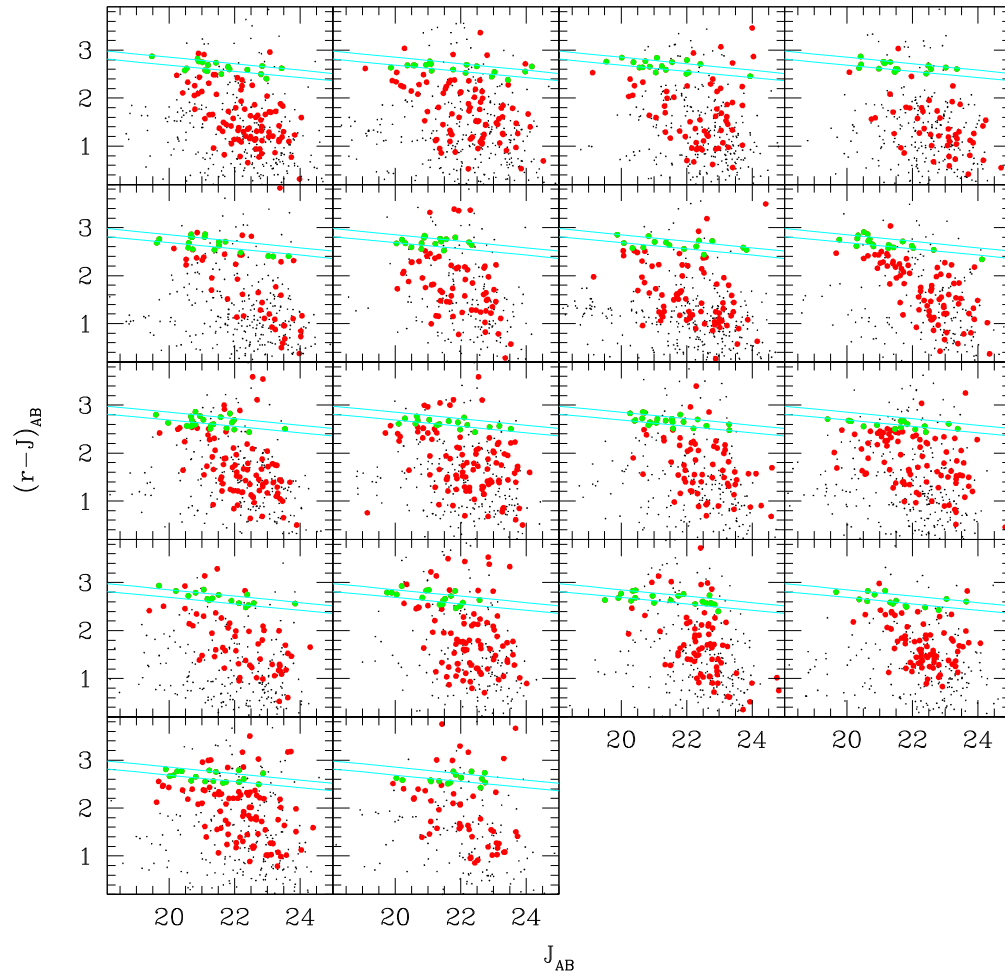
Figure 6.14: The colour magnitude diagrams of massive cluster candidates having $N_{RS} \geq 15$. The colour coding is the same as Figure 6.8.

in Stott et al. (2008).

The spatial and photometric properties of candidates suggest the existence of a supercluster in the DXS SA22 field. In order to confirm this conclusion, spectroscopic observations are necessary.

6.5 Clustering of clusters

Since galaxy clusters trace the extremely overdense regions of dark matter in the Universe, galaxy clusters are more strongly clustered than galaxies and the clustering of galaxy clusters is a good tool to test the cosmological model. Also the clustering strength depends on the richness of a galaxy cluster (Bahcall & Soneira 1983). The average correlation length is $\sim 12h^{-1}$ Mpc for poor clusters and $\sim 25h^{-1}$ Mpc for rich clusters (Bahcall et al. 2003). In this section we show the angular clustering of galaxy cluster candidates detected using the red sequence method from the DXS/CFHTLS catalogue.

The angular correlation function of cluster candidates was measured with the same strategy as used in Chapter 3 and 4. We used candidate galaxy clusters at $0.8 < z < 1.2$. For the random catalogue, 50 times more random points than candidates were generated. The uncertainty in the angular correlation function was calculated with the equation 3.2 assuming a poissonian variance. The integral constraint was also estimated with the equation 3.4. However we assumed a single power-law $(w(\theta) = A_w\theta^{-\delta})$ with a fixed power-law slope of $\delta = 1.0$ which is a widely accepted value. The power-law slope was also confirmed by Papovich (2008) for galaxy clusters in SWIRE fields. Finally the correlation length (r_0) was calculated using equation 3.6 with estimated amplitudes of correlation functions and the distribution of median photometric redshift for each candidate.

As mentioned previously, the algorithm for this work may detect not only candidates of galaxy clusters but also many smaller structures such as galaxy groups. Therefore we used all detected candidates and also applied the N_{RS} criterion for richer candidates to measure the angular correlation functions. The applied N_{RS} criteria were ≥ 8 and 10. For higher N_{RS} criteria than $N_{RS} = 10$, the selected

numbers of candidates were too small to reliably measure the angular correlation function. It is noted that the SA22DXS2 had $N_{RS} = 7$ in the previous section. Figure 6.15 shows angular correlation function for all (top), $N_{RS} \geq 8$ (middle) and $N_{RS} \geq 10$ (bottom) candidates. The measured amplitudes (A_w) are $11.3 \pm 0.9 \times 10^{-3}$ for all candidates, $37.5 \pm 3.5 \times 10^{-3}$ for $N_{RS} \geq 8$ and $53.1 \pm 6.5 \times 10^{-3}$ for $N_{RS} \geq 10$. The amplitude measured by Papovich (2008) was 40.0×10^{-3} similar to the results in this work. This demonstrates that the candidates found by the algorithm are strongly clustered, and their clustering amplitude is much higher than that of EROs and DRGs.

The clustering of galaxy clusters must be related with the cosmological model. Bahcall et al. (2003) and Brodwin et al. (2007) demonstrated that ΛCDM can well describe the cluster correlation length and mean cluster separation relation. In addition Papovich (2008) also pointed out that galaxy clusters at $z > 1$ also follow the relation predicted by ΛCDM. Figure 6.16 shows the correlation length of clusters (r_0) versus mean cluster separation (d_c) relation. Open circles are from Bahcall et al. (2003) including results from various optical and X-ray surveys. The solid curve indicates $r_0 = 2.6\sqrt{d_c}$ in Bahcall et al. (2003) which is consistent with the prediction of the ΛCDM model. The results from this work are displayed with filled circles for all, $N_{RS} \geq 8$ and 10 candidates from left to right, respectively. The correlation length for all candidates is lower than values for other clusters. This may be caused by the contamination of smaller structures in this work. For $N_{RS} \geq 8$ and 10 candidates, the measured correlation strengths follow the observed trend. Therefore the clustering of galaxy clusters in the DXS SA22 field is also consistent with the ΛCDM model.

6.6 Summary

Recent wide field surveys provide the opportunity to detect a cosmologically interesting number of galaxy clusters. In order to perform one of the main scientific goals of the DXS, we have tried to find galaxy clusters in the DXS SA22 field with the DXS/CFHTLS catalogue.
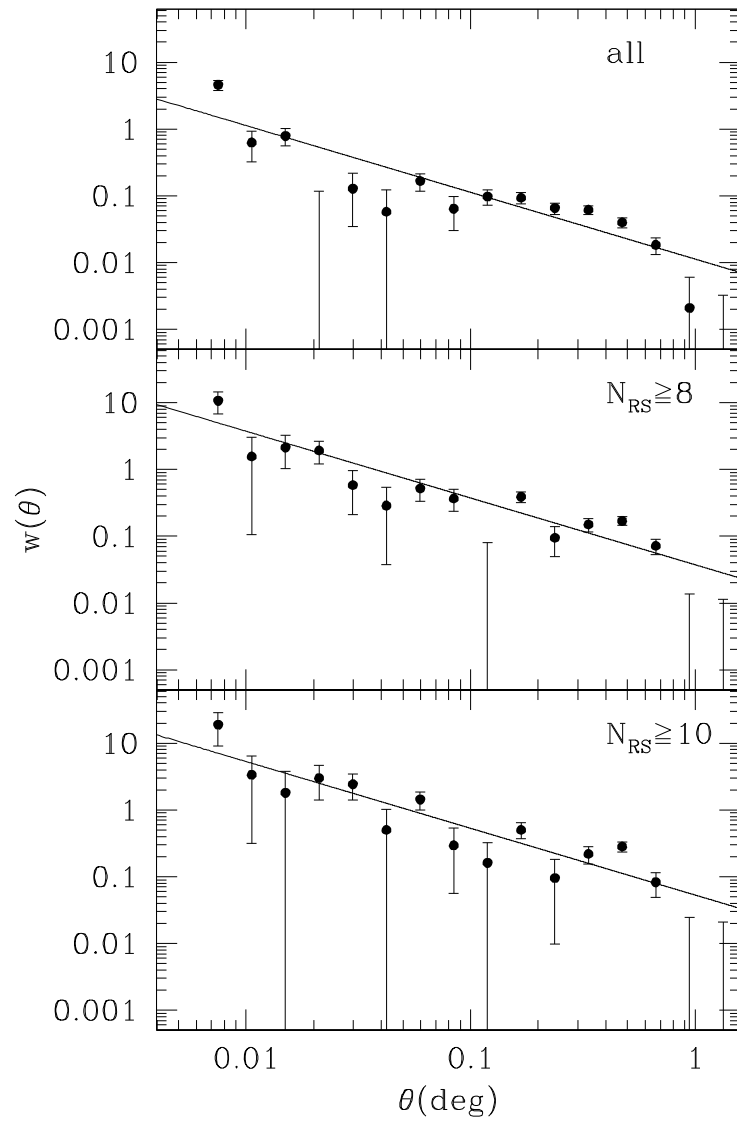
Figure 6.15: The angular correlation functions of candidates of galaxy clusters at $0.8 < z < 1.2$. The top panel is for all detected candidates and middle and bottom panels are for candidates with $N_{RS} \geq 8$ and 10 respectively.
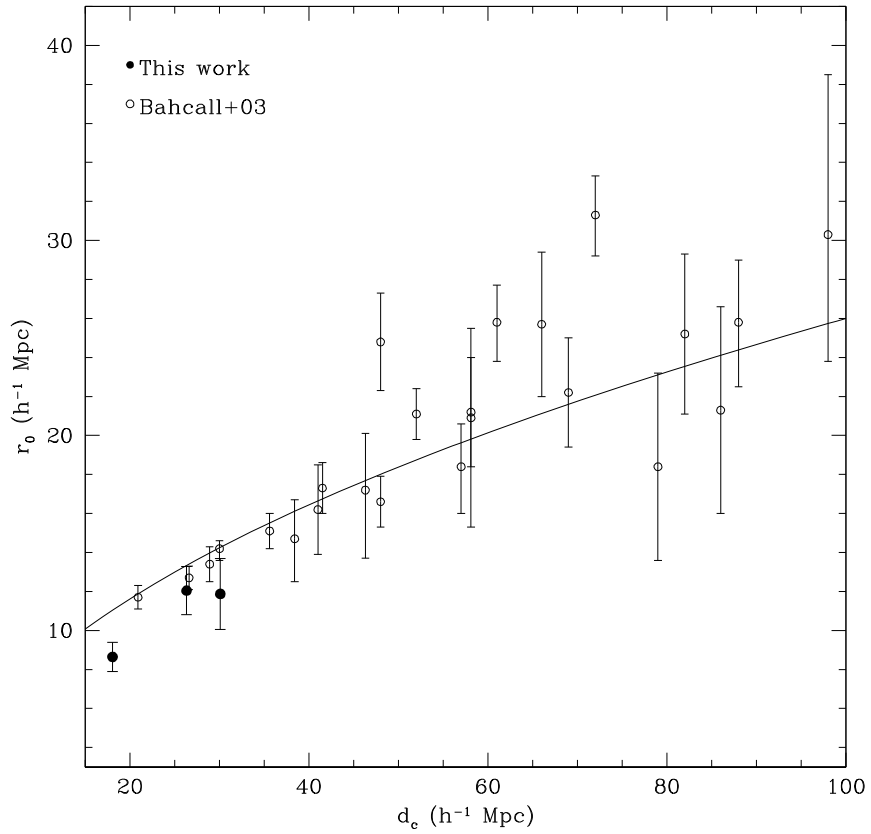
Figure 6.16: The correlation length (r_0) and mean cluster separation (d_c) relation. Filled circles are results in this work. Open circles are from Bahcall et al. (2003) including results by various optical and X-ray surveys. The solid curve indicates $r_0 = 2.6\sqrt{d_c}$ in Bahcall et al. (2003).

The candidate galaxy clusters at $0.8 < z < 1.2$ were selected using the red sequence technique with measured photometric redshifts. The algorithm used in this work successfully detected all galaxy clusters in Elais-N1 published by Swinbank et al. (2007). Moreover many overdense regions corresponding to galaxy clusters were also found from the DXS/CFHTLS catalogue. From our spectroscopic observations we confirmed two galaxy clusters at $z \sim 0.87$. The dynamical masses of these two clusters were $2.1 \times 10^{14} M_\odot$ and $1.7 \times 10^{15} M_\odot$. Combining spatial and photometric redshift distributions of our candidates having higher probability, it may suggest the presence of supercluster in the DXS SA22 field. Finally the angular correlation function of candidates was also measured. The candidate galaxy clusters are strongly clustered, more than any other galaxy population. From the cluster correlation length and mean cluster separation relation, the clustering strengths of cluster candidates in the DXS SA22 field are found to be consistent with the prediction by the ΛCDM model.

In this Chapter we have demonstrated that the existence of galaxy clusters and a probable supercluster. However an accurate measurement of cluster properties is hampered by the small area coverage. When the UKIDSS survey is completed, the DXS will cover $\sim$35 deg^2 and allow the detection of more clusters for the comparison between observational results and the ΛCDM prediction.

Chapter 7

Conclusions

7.1 Key results

We are now in an era where various surveys are being performed through all observable wavelengths. These surveys covering a wide area allow us to investigate the large scale structure of the Universe and rare systems which are difficult to select from smaller area observations. In addition deep and wide near-IR surveys such as the UKIDSS and VISTA surveys make it possible to detect various galaxy populations at high redshift, especially at $z > 1$. In this thesis we study the large scale structure of high redshift galaxy populations selected from their colours, and densest regions of galaxy clusters in the Universe.

In Chapter 2 we described the characteristics of the deep, wide near-IR survey, UKIDSS. UKIDSS began in 2005 with a 7-year plan. UKIDSS consists of 5 sub-surveys covering various areas and depths. The DXS is one of 5 sub-surveys mapping a 35 deg^2 area comprised of 4 different fields. The main science goals of the DXS are to detect galaxy clusters at high redshift, to measure galaxy clustering and bias at $z > 1$ and to study the contribution of starburst galaxies and AGNs to the global energy budget.

Although the UKIDSS standard pipeline provides reduced catalogues of each sub-survey, there are known issues such as spurious objects caused by cross-talk and diffraction spikes, and unreliable total magnitudes. In order to overcome these problems we generated new catalogues with a careful analysis. For these reprocessed

catalogues we reduced the fraction of spurious objects successfully and got better photometric catalogues for the science exploitation. The completeness estimated from an artificial star test satisfies the magnitude goals of the DXS, $J_{vega} = 22.3$ and $K_{vega} = 20.8$, with 90 per cent completeness.

In this thesis we concentrated on the clustering of high redshift galaxies and the detection of galaxy clusters. However the depth and wide coverage of the DXS also give an opportunity to study other science goals. We found candidate KX quasars and brown dwarves in two DXS fields. It was verified that the DXS survey is appropriate to find rare objects located in the vicinity of the Earth to the distant Universe.

In Chapters 3 and 4 we selected high redshift galaxy populations such as EROs and DRGs in DXS SA22 and DXS Elais-N1 fields. The DXS near-IR catalogues were merged with suitable optical datasets which were the *gri* catalogue from the CTIO Blanco telescope for the DXS SA22 field, and Pan-STARRS and Subaru datasets for the DXS Elais-N1 field.

The dependence of the angular correlation functions for EROs and DRGs in the DXS SA22 field on various criteria was described in Chapter 3. From the measured angular correlation function it was confirmed that both populations are strongly clustered. We also found that the angular correlation function of both populations cannot be represented by a single power-law, but by a double power-law with a clear break. Fitting a double power-law to the angular correlation function, brighter samples have higher amplitudes and larger correlation lengths than fainter ones. In the case of EROs, samples selected from brighter magnitude cuts show stronger clustering on small scales, but similar strengths on large scales. While redder EROs show larger correlation lengths on all scales. EROs can be split into old, passive and dusty, star-forming populations. For each population old, passive EROs are more clustered than dusty, star-forming EROs. Additionally the cosmic variance for the WFCAM field size ($\sim$0.8 deg^2) was measured to be 0.2, 1.5 times smaller than that for the CTIO Blanco field size ($\sim$0.36 deg^2). It directly shows the importance of wide area surveys to overcome this cosmic variance effect.

We also measured the angular clustering of EROs from a wider area, and dis-

cussed the dependence of ERO clustering on redshift in Chapter 4. The DXS Elais-N1 field studied was wider than the DXS SA22 field for Chapter 3. Firstly the clustering of EROs in the DXS Elais-N1 field with same criteria in the Chapter 3 was consistent with that for the DXS SA22 field. Thus the result in Chapter 3 is confirmed by the data covering a wider area. From the DXS/PS1 catalogue, EROs were split by photometric redshift and absolute magnitude. The angular correlation functions of EROs at different redshifts showed a similar amplitude on the large scale, indicating a higher bias at higher redshift.

Chapter 5 displayed the halo model fit to the angular correlation function of EROs at different redshifts. Since the clustering of galaxies is directly linked with the distribution of dark matter, we can estimate the halo mass hosting EROs and bias. The standard halo model with the halo occupation distribution works well to restore the angular correlation function of EROs. EROs reside in dark matter haloes having $> 10^{12.9} h^{-1} M_\odot$, and have a bias of 1.93 at $z = 1.12$ and 3.17 at $z = 1.55$. Those results are consistent with halo mass and bias for $> 10^{11} M_\odot$ galaxies at similar redshift ranges. The satellite fractions for EROs are significantly lower than mass limited samples, which may be related to the fact that EROs are massive and red galaxies.

The halo properties and clustering of EROs were also compared with those predicted by the semi-analytic model, GALFORM. Firstly the angular correlation function of EROs at $z = 1.1$ predicted by GALFORM showed good agreement with the observed correlation function, whereas they showed a discrepancy on large scale at $z = 1.5$. This may be caused by a different satellite fraction, since GALFORM predicts too many satellites at $z = 1.5$. With the direct comparison of HODs through the halo model and GALFORM, they showed different shapes and mass thresholds at both redshifts. The effect of AGNs may lead to this difference, because the halo model requires that the central HOD must reach unity but this is not the case for the semi-analytic model. This result may point to the requirement that HOD analysis should be applied with more care to correctly compare results with the prediction of cosmological simulations.

In Chapter 6 we found galaxy clusters at high redshift from the DXS/CFHTLS

catalogue mapping the DXS SA22 field. The red sequence technique was applied to select candidate galaxy clusters at $0.8 < z < 1.2$ with photometric redshift constraints. We demonstrated that the algorithm used in this work finds reliable candidates, comparing candidates with published galaxy clusters at $z \sim 0.9$ in the Elais-N1 field.

For the DXS SA22 field we identified many overdensities at each redshift, using the algorithm. Of candidates at $0.8 < z < 0.9$, we confirmed two galaxy clusters with spectroscopic observations. The SA22DXS2 has the dynamical mass (M_{200}) of $2.1 \times 10^{14} M_\odot$, and the SA22DXS7 has $1.7 \times 10^{15} M_\odot$. Moreover, we found many massive cluster candidates classified with the number of red sequence galaxies, and they were concentrated on the specific region. The photometric redshift distribution of these is described by the Gaussian distribution at $z = 0.83$ with $\sigma = 0.007$. Their spatial and redshift distributions suggests the presence of a supercluster in the DXS SA22 field. Finally we measured the angular correlation function of candidate clusters with richness constraints. This shows that richer candidates are more clustered than poorer candidates which is consistent with previous results. Moreover the correlation lengths for each sub-sample are in good agreement with previous results and the ΛCDM model on the correlation length and mean cluster separation relation.

From the clustering of high redshift galaxies, it is confirmed that the large scale structure was already formed when the Universe was younger than 2 Gyr. Moreover the different clustering properties of passive and dusty star-forming EROs imply that the red sequence of galaxies might be already formed at $z > 1.5$. Overall results from the halo modelling and the clustering of galaxy clusters are consistent the standard ΛCDM cosmological model. However recent cosmological simulations may overpredict the number of red galaxies, especially red satellites. In the near future advanced surveys such as VISTA, LSST, Pan-STARRS, Hyper Suprime Camera on Subaru and Euclid will provide crucial evidence for demonstrating the formation and evolution of galaxies as well as a wider understanding of the Universe.

7.2   Future Work

In the near future it will be possible to measure all quantities more accurately from wider and deeper surveys. The full UKIDSS DXS data will allow the detection of a huge number of high redshift galaxies leading to the accurate measurement of galaxy clustering.

The UKIDSS DXS will be completed in 2012. We will be able to detect EROs and DRGs from the full DXS area. Merging with deep optical datasets, we intend to investigate detailed properties of both populations. Furthermore we can study the evolution of their clustering properties with photometric redshifts. Since both populations represent the most massive objects at high redshift, we can directly compare the result with those at lower redshift estimated from shallower surveys such as SDSS. The full DXS catalogues will also reveal a statistically significant number of galaxy clusters. Since the investigation of galaxies with their environments is a key science in astronomy, we will be able to compare that at low and high redshifts. We intend to apply the cluster finding algorithm to the full DXS area, and will find galaxy clusters at higher redshift. Combining with other optical, X-ray and radio surveys for finding galaxy clusters, it is expected that a large map of the Universe at high redshift can be created. The most interesting objects can be selected for spectroscopic follow-up.

7.3   Scientific Acknowledgements

In this section I would like to include several scientific acknowledgements.

Bibliography

[1] Abell G. O., 1958, ApJS, 3, 211

[2] Abell G. O., Corwin H. G., Jr., Olowin R. P., 1989, ApJS, 70, 1

[3] Adelberger K. L., Steidel C. C., Pettini M., Shapley, A. E., Reddy N. A., Erb
D. K., 2005, ApJ, 619, 697

[4] Adelberger K. L., Steidel C. C., Shapley A. E., Hunt M. P., Erb D. K., Reddy
N. A., Pettini M., 2004, ApJ, 607, 226

[5] Annis J. et al. 1999, AAS, 195, 1202

[6] Bahcall N. A., Dong F., Hao L., Bode P., Annis J., Gunn J. E., Schneider D.
P., 2003, ApJ, 599, 814

[7] Bahcall N. A., Soneira R. M., 1983, ApJ, 270, 20

[8] Barber T., Meiksin A., Murphy T., 2007, MNRAS, 377, 787

[9] Baugh C. M., 2006, Reports on Progress in Physics, 69, 3101

[10] Baugh C. M., Lacey C. G., Frenk C. S., Granato G. L., Silva L., Bressan A.,
Benson A. J., Cole S., 2005, MNRAS, 356, 1191

[11] Beers T. C., Flynn K., Gebhardt K., 1990, AJ, 100, 32

[12] Berlind A. A., Weinberg D. H., 2002, ApJ, 575, 587

[13] Berta S. et al., 2007, A&A, 467, 565

[14] Bertin E., Arnouts S., 1996, A&AS, 117, 393

[15] Bertin E., Mellier Y., Radovich M., Missonier G., Didelon P., Morin B., 2002, in Bohlender D. A., Durand, D., Handley T. H., eds, ASP Conf. Ser., Vol. 281, Astronomical Data Analysis Software and Systems XI. Astron. Soc. Pac., San Francisco, p. 228

[16] Blake C., Collister A., Lahav O., 2008, MNRAS, 385, 1257

[17] Blanc G. A. et al., 2008, ApJ, 681, 1099

[18] Bower R. G., Benson A. J., Malbon R., Helly J. C., Frenk C. S., Baugh C. M., Cole S., Lacey C. G., 2006, MNRAS, 370, 645

[19] Bower R. G., Lucy J. R., Ellis R. S., 1992, MNRAS, 254, 601

[20] Brainerd T. G., Smail I., Mould J., 1995, MNRAS, 275, 781

[21] Brammer G. B. et al., 2009, ApJ, 706, 173

[22] Brammer G. B., van Dokkum P. G., Coppi P., 2008, ApJ, 686, 1503

[23] Brodwin M., Gonzalez A. H., Moustakas L. A., Eisenhardt P. R., Stanford S. A., Stern D., Brown M. J. I., 2007, ApJ, 671, L93

[24] Brown M. J. I., Jannuzi B. T., Dey A., Tiede G. P., 2005, ApJ, 621, 41

[25] Bruzual G., Charlot S., 2003, MNRAS, 344, 1000

[26] Burgasser A. J., Geballe T. R., Leggett S. K., Kirkpatrick J. D., Golimowski D. A., 2006, ApJ, 637, 1067

[27] Butcher H., Oemler A., Jr, 1978, ApJ, 219, 18

[28] Carlberg R. G., Yee H. K. C., Ellingson E., 1997, ApJ, 478, 462

[29] Casali M. et al., 2007, A&A, 467, 777

[30] Cimatti A. et al., 2002, A&A, 381, L68

[31] Cimatti A. et al., 2003, A&A, 412, L1

[32] Cirasuolo M., McLure R. J., Dunlop J. S., Almaini O., Foucaud S., Simpson C., 2010, MNRAS, 401, 1166

[33] Coil A. L. et al., 2008, ApJ, 672, 153

[34] Coil A. L. et al., 2009, ApJ, 701, 1484

[35] Coil A. L., Newman J. A., Cooper M. C., Davis M., Faber S. M., Koo D. C., Willmer C. N. A., 2006, ApJ, 644, 671

[36] Cole S., Ellis R. S., Broadhurst T. J., Colless M. M., 1994, MNRAS, 267, 541

[37] Cole S., Lacey C. G., Baugh C. M., Frenk C. S., MNRAS, 2000, 319, 168

[38] Conselice C. J. et al., 2007, ApJ, 660, 55

[39] Conselice C. J., Bundy K., U V., Eisenhardt P., Lotz J., Newman J., 2008, MNRAS, 383, 1366

[40] Cooray A. et al., 2010, A&A, 518, 22

[41] Cooray A., Sheth R., 2002, Physics Reports, 372, 1

[42] Croom S. M., Warren S. J., Glazebrook K., 2001, MNRAS, 328, 150

[43] Daddi E., Cimatti A., Pozzetti L., Hoekstra H., Röttgering H. J., Renzini A., Zamorani G., Mannucci F., 2000, A&A, 361, 535

[44] Daddi E., Cimatti A., Renzini A., Fontana A., Mignoli M., Pozzetti L., Tozzi P., Zamorani G., 2004, ApJ, 617, 746

[45] Dalton G. B., Maddox S. J., Sutherland W. J., Efstathiou, G., 1997, MNRAS, 289, 263

[46] Davis M. et al., 2007, ApJ, 660, 1

[47] Demarco R. et al., 2010, ApJ, 711, 1185

[48] Dye S. et al., 2006, MNRAS, 372, 1227

[49] Edge A. C., 2001, MNRAS, 328, 762

[50] Edge A. C., Ivison R. J., Smail I, Blain A. W., Kneib J.-P., 1999, MNRAS, 306, 599

[51] Eke V. R. et al., 2004, MNRAS, 355, 769

[52] Eke V. R., Cole S., Frenk C. S., Patrick Henry J., 1998, MNRAS, 298, 1145

[53] Elston R., Rieke G. H., Rieke M. J., 1988, ApJ, 331, 77

[54] Erben T. et al., 2009, A&A, 493, 1197

[55] Fall S. M., Efstathiou G., 1980, MNRAS, 193, 189

[56] Fang G. -W., Kong X., Wang M., 2009, Res. Astron. Astrophys., 9, 59

[57] Firth A. E. et al., 2002, MNRAS, 332, 617

[58] Foucaud S. et al., 2007, MNRAS, 376, L20

[59] Foucaud S., Conselice C. J., Hartley W. G., Lane K. P., Bamford S. P., Almaini O., Bundy K., 2010, MNRAS, 406, 147

[60] Foucaud S., McCracken H. J., Le Févre O., Arnouts S., Brodwin M., Lilly S. J., Crampton, D., Mellier, Y., 2003, A&A, 409, 835

[61] Franx M. et al., 2003, ApJ, 587, L79

[62] Furusawa J., Sekiguchi K., Takata T., Furusawa H., Shimasaku K., Simpson C., Akiyama Masayuki., 2011, ApJ, 727, 111

[63] Garilli B. et al., 2008, A&A, 486, 683

[64] Georgakakis A., Afonso J., Hopkins A. M., Sullivan M., Mobasher B., Cram L. E., 2005, ApJ, 620, 584

[65] Gladders M. D., Yee H. K. C., 2000, AJ, 120, 2148

[66] Gladders M. D., Yee H. K. C., 2005, ApJ, 157, 1

[67] Glazebrook K., Bland-Hawthorn J., 2001, PASP, 113, 197

[68] Golimowski D. A., et al. 2004, AJ, 127, 3516

[69] Gonzalez A. H., Zaritsky D., Wechsler R. H., 2002, ApJ, 571, 129

[70] Gonzalez-Perez V., Baugh C. M., Lacey C. G., Almeida, C., 2009, MNRAS, 398, 497

[71] Gonzalez-Perez V., Baugh C. M., Lacey C. G., Kim J. -W., 2011, MNRAS, in press (arXiv:1105.3477)

[72] Grazian A. et al., 2006, A&A, 453, 507

[73] Groth E. J., Peebles, P. J. E., 1977, ApJ, 217, 385

[74] Gunn J. E., Hoessel J. G., Oke J. B., 1986, ApJ, 306, 30

[75] Hambly N. C. et al., 2008, MNRAS, 384, 637

[76] Hartley W. G. et al., 2010, MNRAS, 407, 1212

[77] Hempel A. et al., 2011, MNRAS, 414, 2246

[78] Hewett P. C., Warren S. J., Leggett S. K., Hodgkin S. T., 2006, MNRAS, 367, 454

[79] Heydon-Dumbleton N. H., Collins C. A., MacGillivray, H. T., 1989, MNRAS, 238, 379

[80] Hickox R. C. et al., 2011, ApJ, 731, 117

[81] Hoekstra H., Franx M., Kuijken K., 2000, ApJ, 532, 88

[82] Hubble E., 1929, PNAS, 15, 168

[83] Jing Y. P., Mo H. J., Boerner G., 1998, ApJ, 494, 1

[84] Kaiser N., Pan-STARRS team, 2002, BAAS, 34, 1304

[85] Kauffmann G., Colberg J. M., Diaferio A., White S. D. M., 1999, MNRAS, 307, 529

[86] Kim R. S. J. et al., 2002, AJ, 123, 20

[87] Knapp G. R. et al., 2004, AJ, 127, 3553

[88] Kong X. et al., 2006, ApJ, 638, 72

[89] Kong X., Fang G., Arimoto N., Wang M., 2009, ApJ, 702, 1458

[90] Kovač K., Somerville R. S., Rhoads J. E., Malhotra S., Wang J., 2007, ApJ, 668, 15

[91] Labbé I. et al., 2005, ApJ, 624, L81

[92] Landy S. D., Szalay A. S., 1993, ApJ, 412, 64

[93] Lane K. P. et al., 2007, MNRAS, 379, L25

[94] Lawrence A. et al., 2007, MNRAS, 379, 1599

[95] Le Févre O. et al., 2005, A&A, 439, 845

[96] Lewis A., Challinor A., Lasenby A., 2000, ApJ, 538, 473

[97] Limber D. N., 1953, ApJ, 117, 134

[98] Limber D. N., 1954, ApJ, 119, 655

[99] Lodieu N., Dobbie P. D., Deacon N. R., Venemans B. P., Durant M., 2009, MNRAS, 395, 1631

[100] Lonsdale C. J. et al., 2003, PASP, 115, 897

[101] Lopes P. A. A., de Carvalho R. R., Gal R. R., Djorgovski S. G., Odewahn S. C., Mahabal A. A., Brunner, R. J., 2004, AJ, 128, 1017

[102] Lumsden S. L., Nichol R. C., Collins C. A., Guzzo, L., 1992, MNRAS, 258, 1

[103] Ma C. -P., Fry J. N., 2000, ApJ, 543, 503

[104] Maddox S. J., Efstathiou G., Sutherland W. J., Loveday J., 1990, MNRAS, 242, 43

[105] Maddox N., Hewett P. C., Warren S. J., Croom S. M., 2008, MNRAS, 386, 1605

[106] Matsuoka Y., Masaki S., Kawara K., Sugiyama N., 2011, MNRAS, 410, 548

[107] McCarthy P. J. et al., 2001, ApJ, 560, L131

[108] Mo H. J., White S. D. M., 2002, MNRAS, 336, 112

[109] Moustakas L. A. et al., 2004, ApJ, 600, L131

[110] Moustakas L. A., Somerville R. S., 2002, ApJ, 577, 1

[111] Muzzin A., Wilson G., Lacy M., Yee H. K. C., Stanford S. A., 2008, ApJ, 686, 966

[112] Navarro J. F., Frenk C. S., White S. D. M., 1997, ApJ, 490, 493

[113] Neuschaefer L. W., Windhorst R. A., 1995, ApJ, 439, 14

[114] Norberg P. et al., 2001, MNRAS, 328, 64

[115] Norberg P. et al., 2002, MNRAS, 332, 827

[116] Papovich C., 2008, ApJ, 676, 206

[117] Papovich C. et al., 2006, ApJ, 640, 92

[118] Peacock J. A., Smith R. E., 2000, MNRAS, 318, 1144

[119] Peebles P. J. E., 1980, The Large-Scale Structure of the Universe. Princeton Univ, Press, Princeton, NJ.

[120] Perlmutter S. et al., 1998, Nature, 391, 51

[121] Postman M., Lauer T. R., Szapudi I., Oegerle W., 1998, ApJ., 506, 33

[122] Postman M., Lubin L. M., Gunn J. E., Oke J. B., Hoessel J. G., Schneider D. P., Christensen J. A., 1996, AJ, 111, 615

[123] Pozzetti L., Mannucci F., 2000, MNRAS, 317, L17

[124] Press W. H., Schechter P., 1974, ApJ, 187, 425

[125] Quadri R. et al., 2007, AJ, 134, 1103

[126] Quadri R. F., Wiiliams R. J., 2010, ApJ, 725, 794

[127] Quadri R. F., Williams R. J., Lee K., Franx M., van Dokkum P., Brammer G. B., 2008, ApJ, 685, L1

[128] Riess A. G. et al., 1998, AJ, 116, 1009

[129] Roche N. D., Almaini O., Dunlop J., Ivison R. J., Willott C. J., 2002, MNRAS, 337, 1282

[130] Roche N. D., Dunlop J., Almaini O., 2003, MNRAS, 346, 803

[131] Roche N., Eales S. A., Hippelein H., Willott C. J., 1999, MNRAS, 306, 538

[132] Rosati P., Stanford S. A., Eisenhardt P. R., Elston R., Spinrad H., Stern D., Dey A., 1999, AJ, 118, 76

[133] Ross A. J., Brunner R. J., 2009, MNRAS, 399, 878

[134] Ross A. J., Percival W. J., Brunner R. J., 2010, MNRAS, 407, 420

[135] Ross N. P., Shanks T., Cannon R. D., Wake D. A., Sharp R. G., Croom S. M., Peacock J. A., 2008, MNRAS, 387, 1323

[136] Rowan-Robinson M. et al., 2008, MNRAS, 386, 697

[137] Sánchez E. et al., 2011, MNRAS, 411, 277

[138] Sawangwit U., Shanks T., Abdalla F. B., Cannon R. D., Croom S. M., Edge A. C., Ross N. P., Wake D. A., 2009, MNRAS, submitted (arXiv:0912.0511)

[139] Sawicki M., Stevenson M., Barrientos L. F., Gladman B., Mallén-Ornelas G., van den Bergh S., 2005, ApJ, 627, 621

[140] Schlegel D. J., Finkbeiner D. P., Davis M., 1998, ApJ, 500, 525

[141] Scoccimarro R., Sheth R. K., Hui L., Jain B., 2001, ApJ, 546, 20

[142] Scoville N. et al., 2007, ApJS, 172, 1

[143] Seljak U., 2000, MNRAS, 318, 203

[144] Sheth R. K., Tormen G., 1999, MNRAS, 308, 119

[145] Simpson C. et al., 2006, MNRAS, 373, L21

[146] Skrutskie M. F. et al., 2006, AJ, 131, 1163

[147] Smail I., Owen F. N., Morrison G. E., Keel W. C., Ivison R. J., Ledlow M. J., 2002, ApJ, 581, 844

[148] Smail I., Sharp R., Swinbank A. M., Akiyama M., Ueda Y., Foucaud S., Almaini O., Croom, S., 2008, MNRAS, 389, 407

[149] Smith R. E. et al., 2003, MNRAS, 341, 1311

[150] Somerville R. S., Lee K., Ferguson H. C., Gardner J. P., Moustakas L. A., Giavalisco M., 2004, ApJ, 600, L171

[151] Steidel C. C., Giavalisco M., Pettini M., Dickinson M., Adelberger K. L., 1996, ApJ, 462, 17

[152] Steidel C. C., Hamilton D., 1992, AJ, 104, 941

[153] Stott J. P., Edge A. C., Smith G. P., Swinbank A. M., Ebeling H., 2008, MNRAS, 384, 1502

[154] Surace J., Shupe D. L., Fang F., Lonsdale C. J., Gonzalez-Solares E., 2005, SSC Web site Release: The SWIRE Data Release 2 (Pasadena, CA: CalTech)

[155] Swinbank A. M. et al., 2007, MNRAS, 379, 1343

[156] Tanaka I., Yamada T., Turner E. L., Suto Y., 2001, ApJ, 547, 521

[157] Tinker J. L., Kravtsov A. V., Klypin A., Abazajian K., Warren M., Yepes G., Gottlöber S., Holz D. E., 2008 ApJ, 688, 709

[158] Tinker J. L., Robertson B. E., Kravtsov, A. V., Klypin A., Warren M. S., Yepes G., Gottlöber S., 2010, ApJ, 724, 878

[159] Tinker J. L., Wechsler R. H., Zheng Z., 2010, ApJ, 709, 67

[160] Tinker J. L., Weinberg D. H., Zheng Z., Zehavi I., 2005, ApJ, 631, 41

[161] Tran K. H. et al. 2010, ApJ, 719, 126

[162] Trenti M., Stiavelli M., 2008, ApJ, 676, 767

[163] Trichas M. et al., 2010, MNRAS, 405, 2243

[164] van Breukelen C. et al., 2006, MNRAS, 373, L26

[165] van Dokkum P. G. et al., 2009, PASP, 121, 2

[166] van Dokkum P. G. et al., 2010, ApJ, 709, 1018

[167] Wake D. A. et al., 2008, MNRAS, 387, 1045

[168] Wake D. A. et al., 2011, ApJ, 728, 46

[169] Warren S. J., Hewett P. C., Foltz C. B., 2000, MNRAS, 312, 827 D. A. et al.,

[170] Whitaker K. E. et al., 2011, ApJ, 735, 86

[171] White S. D. M., Frenk C. S., 1991, ApJ, 379, 52

[172] White S. D. M., Rees M. J., 1978, MNRAS, 183, 341

[173] Williams R. J., Quadri R. F., Franx M., van Dokkum P., Labbé I., 2009, ApJ, 691, 1879

[174] Wilson G. et al., 2009, ApJ, 698, 1943

[175] Wright E. L., 2006, PASP, 118, 1711

[176] York D. G. et al., 2000, AJ, 120, 1579

[177] Zehavi I. et al., 2002, ApJ, 571, 172

[178] Zehavi I. et al., 2005, ApJ, 630, 1

[179] Zehavi I. et al., 2011, ApJ, 736, 59

[180] Zheng Z. et al., 2005, ApJ, 633, 791

[181] Zwicky, F., Herzog E., Wild P., 1968, Catalogue of galaxies and of clusters of galaxies, Caltech, Pasadena